Scalable Pathogen Extraction Platform for the Treatment of Blood-borne Infections

By

Sinead Emily Miller

Dissertation
Submitted to the Faculty of the
Graduate School of Vanderbilt University
in partial fulfillment of the requirements
for the degree of

DOCTOR OF PHILOSOPHY
in

Biomedical Engineering
May, 2017
Nashville, Tennessee

Approved:

Todd D. Giorgio, Ph.D.

Timothy L. Cover, M.D.

Frederick R. Haselton, Ph.D.

Michael I. Miga, Ph.D.

John P. Wikswo, Ph.D.

ACKNOWLEDGEMENTS

First, praise and thanks goes to the Lord Jesus Christ for blessing me with the ability to perform this work. I sincerely thank my advisor, Todd D. Giorgio, for giving me the opportunity to be a member of his lab at Vanderbilt University. Without his persistent support and guidance this dissertation would not have been possible. He encouraged me to not only grow as a scientist, but also as an independent thinker. Dr. Giorgio provided me with the opportunity to develop my own individuality and self-sufficiency by allowing me to work with independence. I can't thank him enough for this. I would also like to thank all of the members of the Giorgio research group for their support. I especially want to thank Charleson Bell, Austin Anthony, and Stephen Petty Valenzuela for their academic support, friendship, and feedback on my work. These three friends and co-workers also provided endless humor and entertainment, filling of our days in the lab with laughter. I would like to thank Timothy Cover, Mark McClain, Chrissy Marasco, David Schaffer, Frederick Haselton, Michael Miga, John Wikswo, and Craig Duvall for letting me use equipment in their labs and for their input. Also, I want to thank the Department of Defense (W81XWH-13-1-0397) for providing financial support for this work.

I want to express my love and gratitude to my family and friends. I thank my parents for instilling in me an unwavering drive and for providing encouragement through every step of this journey. I thank Samantha for being my ever supportive sister and for providing countless laughs and memories. I thank Alex for providing me with encouraging words, persistent love, and friendship. This work would not have been possible without these individuals.

TABLE OF CONTENTS

Page

Chapter

Appendix

LIST OF TABLES

Table Page

LIST OF FIGURES

LIST OF ABBREVIATIONS

ζ	zeta potential
°C	degrees Celsius
ANOVA	analysis of variance
ATCC	American Type Culture Collection
Au	gold
AUC	area under the curve
AuNPs	gold nanoparticles
CFU	colony forming unit
Cl	chlorine
Col	colistin
Col-PEG-AuNP	colistin functionalized gold nanoparticles
Ctrl	control
Cu	copper
D_2O	deuterium oxide
Dab	diaminobutyric acid
DI	de-ionized
DLS	dynamic light scattering
DMEM	Dulbecco's modified Eagle's medium
DMSO	dimethylsulfoxide
EDS	energy dispersive spectroscopy
ELISA	enzyme-linked immunosorbent assay
EU	endotoxin unit
FBS	fetal bovine serum
FDA	Food and Drug Administration

H	height
H^1 NMR	proton nuclear magnetic resonance
HAADF-STEM	High angle annular dark field scanning transmission electron microscopy
HepG2	human liver carcinoma cancer cell line
HS-PEG$_{2000}$	thiolated polyethylene glycol
HUVEC	human umbilical vein endothelial cell line
IL-1	interleukin-1
IRB	Institutional Review Board
K	potassium
L	length
LB-Agar	Lennox L Agar
LB Broth	Lennox L Broth
LPS	lipopolysaccharide
MDR	multi-drug resistance
MIC	minimum inhibitory concentrations
MNPs	magnetic nanoparticles
N	nitogren
Na	sodium
$NaHCO_3$	sodium bicarbonate
NHS-PEG$_{3400}$-OPSS	succinimidyl ester-polyethylene glycol-ortho-pyridyl disulfide
NHS-PEG-Silane	*N*-hydroxysuccinimide-polyethylene glycol$_{1000}$-silane
NP	nanoparticle
P	phosphate
PBPK	physiologically based pharmacokinetic
PBS	phosphate buffer solution
PDMS	polydimethylsiloxane

PEG	polyethylene glycol
PEG-AuNP	polyethylene glycol functionalized gold nanoparticle
PEG-Silane	polyethylene glycol$_{1000}$-silane
RBC	red blood cell
SD	standard deviation
TNF-α	tumor necrosis factor-alpha
v/v%	volume/volume percent
W	width

CHAPTER I

INTRODUCTION

The presence of bacteria in the circulatory blood initiates a cascade of local and systemic regulatory mechanisms that often result in sepsis[1]. Sepsis, defined as a life-threatening organ dysfunction caused by a dysregulated host response to infection, afflicts over one million Americans annually and has an associated mortality rate ranging from 25-50%[2,3]. Sepsis is the leading cause of death in the critically ill in the United States, costing the US over $20 billion in treatment annually[2,3]. These statistics clearly define a tremendous clinical need for improved therapeutic strategies to better address sepsis and sepsis progression.

Acinetobacter baumannii, a Gram-negative coccobacillus with a multi-drug resistant (MDR) phenotype, is a leading cause of sepsis worldwide[4,5]. *A. baumannii* is widely distributed in nature and has few nutritional requirements for growth[6]. The organism is able to thrive at various temperatures and pH conditions, while utilizing a variety of carbon and energy sources[7,8]. These properties help explain the resilient fitness of *A. baumannii*, contributing to its rapid transmission, and aid in our understanding as to why this bacterium continues to persist even in harsh environments. *A. baumannii* is not only characterized by robustness, but this bacterium also has an intrinsic resistance to many antibiotics, contributing to its MDR phenotype[9]. These characteristics have led the CDC to classify *A. baumannii* as a ‘Serious Threat’ to the United States, warning that the threat will continue to worsen if new treatment and prevention therapies are not developed[10].

A. baumannii rates of infection are significantly increasing due to the expanding incidence of MDR *A. baumannii* species[11]. As humans continue to inadvertently accelerate the evolution of bacterial resistance through over-use of antibiotics, the major problem of MDR will grow in scope and impact. Immunosuppression and neutropenia are significant risk factors associated with development of *A. baumannii* induced sepsis[12]. If left untreated or inappropriately treated, progression of sepsis can lead to widespread inflammation, blood clotting, multiple organ failure, pneumonia, septic shock, and death[6].

The lack of new antibiotics in the developmental pipeline, combined with increasing numbers of elderly and immunocompromised populations, suggests that the incidence of *A. baumannii*-associated sepsis will continue to pose as a significant global health problem[13]. A common treatment for *A. baumannii*-associated sepsis is empiric, broad-spectrum antibiotic therapy. Unfortunately, high dose antibiotic administration can result in serious side effects, including significant renal and neurological toxicity[14]. The increasing incidence of *A. baumannii*-associated infection combined with the lack of effective and safe antibiotics is leading us into the post-antibiotic era. New treatment methods for sepsis must be developed and utilized to counter antibiotic ineffectiveness and overuse.

Various research groups have attempted to circumvent the limitations of monotherapy antibiotic treatment by using synergistic antibiotic combination therapies against *A. baumannii* species. Novel combinations of antibiotics have proven to be effective at eradicating *A. baumannii* infection[15–17]. However, multi-drug therapies promote the development of antibiotic resistance through the bacterium production of drug-inactivating enzymes, efflux pumps, and target-site or outer membrane modifications[18]. Pan-drug resistant *A. baumannii* strains have already emerged[19,20].

Progression from sepsis to severe sepsis or septic shock results partially from an initial failure to effectively eradicate infection. Bacterial cells and endotoxins propagate from the primary site of infection to distal organ sites through the bloodstream, overwhelming the immune system and causing a dysregulated host response to infection. Alternative treatment methods (e.g. fluid resuscitation, anti-thrombosis therapy, removal of inflammatory mediators, and organ support) do not address the root cause of sepsis - the persistence of pathogens that continuously release pathogen-associated toxins into the bloodstream[21].

All major antimicrobial resistance mechanisms known to occur in bacteria are employed by *A. baumannii* to escape antibiotic-induced death[22]. This has led researchers to work towards developing therapies that treat the root cause of sepsis and are not reliant on antibiotic-induced bacterial cell death. A number of approaches, founded on separation biophysics, have been demonstrated to isolate bacteria from simple fluids. For example, bacteria-targeting magnetic nanoparticles (MNPs) have been designed to bind bacteria, which can then be separated from fluid with up to 50% efficiency by applying external magnetic fields[23–25]. It has been reported by Singh et al. that surface-functionalized MNPs can be used for capture and magnetic extraction of *Escherichia coli* from saline solution[24]. Also, Kang et al. have successfully employed genetically engineered human opsonin functionalized MNPs to capture and remove *Staphylococcus aureus* and *Escherichia* coli from fluid[25]*.* Mathematical modeling, however, suggests that effective binding to bacteria in whole blood at physiologically relevant flow rates requires MNP diameters of less than 50 nm, which is too small to isolate even for the most advanced magnetic separation systems[26,27]. Therefore, more work must be done in order to develop other bacteria separation strategies, including bacterial hemofiltration.

Hemoperfusion columns designed to remove endotoxin (lipopolysaccharide) and cytokines from the blood have been developed for the treatment of sepsis[28,29]. However, these columns do not remove bacteria and have not been approved for use in the US, citing the lack of effectiveness and clogging. Therefore, an improved technology must be developed to treat the root cause of sepsis through direct removal of pathogens and endotoxins, overcoming the surface area limitations imposed by membrane-based column filters and eliminating the risk of clogging.

Recently, microfluidic cross-flow filtration methods have been used to sequester bacteria from whole blood. Raub et al. have developed a size-exclusion based microfluidic device for this purpose[30]. The implementation of size-exclusion and margination-based cross-flow channels in a microfluidic device allowed for 30% separation of bacteria from red blood cells using flow rates up to 100 µL/min.

Inertial lift and Dean forces have also been used in more complex microscale spiral or double spiral systems to focus particles into multiple, size-dependent equilibrium positions within the channel cross section, leading to distinct microparticle separation[31,32]. These types of inertial-based microfluidic devices have been shown to separate 5 μm sized particles from 15 μm sized particles with a 95% separation efficiency (Fig 1.1)[32]. Appropriate alteration of channel geometry and the ratio of inertial lift force to Dean force can result in particle stream migration near the walls of a double spiral microchannel. By taking advantage of the large inertial lift forces experienced by particles in high aspect ratio spiral channels, particles as small as 590 nm in diameter have been shown to migrate into particle streamlines near the channel walls, away from the channel center (Fig 1.2)[33].

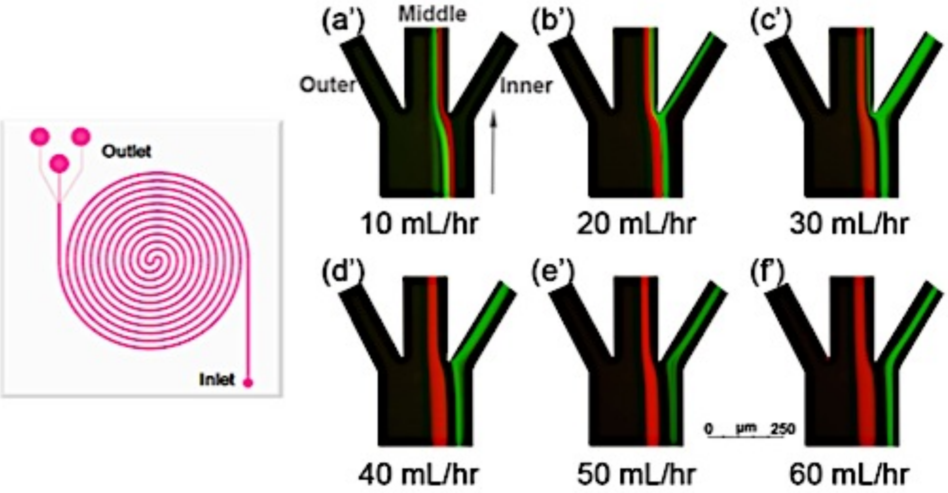

Figure 1.1. Superimposed fluorescent images taken within the outlet of a double spiral microfluidic channel show the separation of 5 µm (green) and 15 µm (red) particles at various flow rates[32].

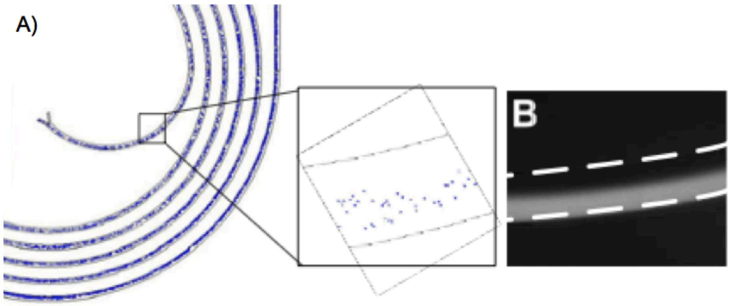

Figure 1.2. **a**, Simulation results indicating the 590 nm particle distribution across the channel width in the spiral channel. **b**, Experimental result showing the 590 nm particle distribution (fluorescent stream) across the channel width at the outlet[33].

These results demonstrating the separation of micron-sized particles from flowing fluid using spiral microfluidic systems are promising and have the potential to be further altered and scaled for capture and removal of bacteria from fluid, thereby aiding in the treatment of bacterial sepsis. Bacteria are heterogeneous in size and shape, unlike the homogenous spherical particles used in Figures 1.1 and 1.2. Therefore, the translation of the previous work to bacteria is nontrivial.

Objectives

The central hypothesis of my dissertation is that a model-based fluidic platform can be used for inertial focusing and capture of *Acinetobacter baumannii*, including colistin-resistant variants. Furthermore, I hypothesize that the proposed approach will remove *A. baumannii* from whole blood, providing a new paradigm for the treatment of sepsis. This approach addresses the unmet need for improved bacterial eradication through extracorporeal blood cleansing, which, in the absence of effective antibiotic treatment, represents the most powerful and adaptive system for blood-borne bacterial elimination. Therefore, the **objectives** of this work are to **(1)** fabricate a ligand designed to capture and bind *A. baumannii*, including colistin-resistant variants, **(2)** develop a computational model that enables prediction of *A. baumannii* clearance characteristics needed for successful removal of bacteria from circulation, and **(3)** design a mathematical model-based fluidic platform functionalized with the *A. baumannii*-targeting ligand for capture of the pathogen from fluid.

Specific Aims

Specific Aim 1: A ligand designed for the capture of *Acinetobacter baumannii* from fluid will be synthesized. Assessment of *A. baumannii* capture using the designed ligand will be characterized.

Specific Aim 2: A mathematical model describing the kinetics and distribution of *A. baumannii* pathogenesis will be developed. This model will be used to predict *A. baumannii* clearance requirements for the treatment of sepsis.

Specific Aim 3*:* Modeling predictions will be incorporated to design and fabricate an inertial-based fluidic platform decorated with an *A. baumannii*-targeting ligand for the separation and capture of *A. baumannii* from flowing fluid. Separation and capture of *A. baumannii* from flowing fluid through ligand interactions will be characterized.

Background and Significance

This research addresses the need for a better understanding of the feasibility of bacterial separation from flowing fluid. Bacterial separation techniques have been developed for the treatment of sepsis, however, feasibility of these techniques remains unknown. Therefore, this work is aimed towards developing a bacterial pathogenesis model to inform bacterial separation needs, which will then be used to build and test a bacterial separation device. Sepsis afflicts millions of people globally each year and is ranked among the top seven causes of death in Europe and North America[34–36]. Development and progression of sepsis is often a result of immunosuppression, previous antibiotic therapy, or previous sepsis, each of which are independently related[37]. *Acinetobacter baumannii*, a Gram-negative coccobacillus, is a particularly formidable cause of sepsis and fatal bacterial toxemia because it is both difficult to control and treat[37]. This microorganism can persist in the harshest environments and colonize a wide range of human and environmental reservoirs[37,38]. The great resilience and genomic plasticity of *A. baumannii*, combined with overuse of antimicrobials, has promoted the evolution of multi-drug resistant (MDR) *A. baumannii* along with the acquisition of novel virulence characteristics[39]. The transformation of *A. baumannii* into an antimicrobial-evading pathogen has severely restricted the therapeutic options available for infected patients, and has increased mortality rates[40,41]. The continued stagnation of antibiotic development, combined with the large number of negative side effects associated with antibiotic administration, has led to the need for development of new treatment strategies for *A. baumannii* sepsis. This work details the development of a microfluidic device-based approach that addresses these key issues and enables selective capture and eradication of *A. baumannii* from flowing fluid.

Colistin, a polycationic molecule, selectively interacts both electrostatically and hydrophobically with the negatively charged lipid A component of bacterial lipopolysaccharide (LPS), the major outer membrane component of Gram-negative bacteria[42,43]. Although colistin-functionalized nanoparticles are particularly useful for the capture of *A. baumannii* in fluid, extraction of nanoparticle-bound bacteria is a nontrivial limitation of this technology. To circumvent this obstacle, a model-based microfluidic channel decorated with a colistin ligand was developed, which was used to capture *A. baumannii* from fluid. The microchannel dimensions were designed in such a way as to leverage inertial lift forces to focus the bacteria near the colistin-functionalized channel walls, thereby allowing continuous capture and removal of *A. baumannii* from the flowing fluid. This innovative bacterial separation device not only enables the removal of *A. baumannii* from fluid, but also removes endotoxin and other Gram-negative bacteria species from circulating fluids. This work will inform the design and feasibility of bacterial separation devices, which could have the capacity to aid in the treatment of sepsis. The breakthrough concept of this work is that this inertial-based fluidic platform can separate and immobilize bacteria from continuously flowing whole blood, avoiding obstacles to translation that limit blood purification therapies that utilize membrane-based filters for removal of inflammatory mediators and other toxins. Advancement of this work may improve sepsis-associated outcomes by treating sepsis rapidly at the source and potentially decrease the current threat of the 'post-antibiotic era' through effective treatment of multi-drug resistant pathogens. ***Mechanically removing bacteria and endotoxins breaks the current paradigm of sepsis therapy that is focused on applying antibiotics following bacterial culture and identification.***

CHAPTER II

COLISTIN LIGAND FOR THE RAPID CAPTURE OF BACTERIA

Gold nanoparticles (AuNPs) were functionalized for rapid binding of *Acinetobacter baumannii* (*A. baumannii*), a Gram-negative bacterium. AuNPs were functionalized with colistin (Col), a polycationic antibiotic, using a two-step self-assembly process, in which heterobifunctional polyethylene glycol (PEG) was used as a linker. Colistin was successfully conjugated to the AuNPs (Col-PEG-AuNP), as validated by dynamic light scattering (DLS) and proton nuclear magnetic resonance (H^1 NMR). High angle annular dark field scanning transmission electron microscopy (HAADF-STEM) images, acquired simultaneously with x-ray energy dispersive spectroscopy (EDS) data, confirmed binding of Col-PEG-AuNPs to the cell envelope of *A. baumannii*. Results generated from a rapid binding assay indicated that Col-PEG-AuNP complexation with *A. baumannii* occurred rapidly and reached half-maximum saturation in approximately 7 minutes, on average, for all *A. baumannii* strains evaluated. Quantitative measurement of the kinetics of Col-PEG-AuNP binding to *A. baumannii* is essential to inform the design of colistin-functionalized magnetic nanoparticles for magnetic separation of nanoparticle-bound *A. baumannii*. Results from this chapter will fulfill Specific Aim 1 of my dissertation.

Introduction

Acinetobacter baumannii is commonly found in soil, water, mucous membranes, vegetables, and on human skin[1]. Individuals with a compromised immune system, diabetes, or wounds can suffer from life-threatening infections resultant from *A. baumannii*. Infections caused by *A. baumannii* can lead to widespread inflammation, blood clotting, multiple organ failure, pneumonia, septic shock, and death[6]. *A. baumannii* is responsible for 2% to 10% of Gram-negative bacterial infections worldwide and has an associated mortality rate reaching up to 60%[41,44,45].

The spread of *A. baumannii* occurs via human contact and through contact with contaminated food, soil, water, and hospital equipment[46]. *A. baumannii* has been detected in freshwater ecosystems, sewage, wastewater, drinking water, and groundwater supplies[46,47]. Infections resultant from *A. baumannii* and other Gram-negative bacteria can be transmitted by contaminated drinking water[48]. Various adsorption columns have been developed for the removal of bacteria from fluid[49–51]. Unfortunately, these devices have drawbacks due to slow, diffusion-limited operation and surface sites, which decrease the adsorption capacity of the adsorbent. Separation of adsorbents from bulk medium can be complex. Thus, the development of adsorbents with higher adsorptive capacity, low diffusion resistance, and fast separation is of great importance in practical engineering applications.

Recently, alternative approaches have been sought to address the shortcomings of current treatments for various bacterial contaminations and infections. In particular, bacteria-targeting magnetic nanoparticles (MNPs) have been developed for the separation of MNP-bound bacteria from wastewater or blood using external magnetic fields[24,52]. Nanoparticles have a high surface area to volume ratio, which enables high adsorption efficiency. Singh et al. have reported that surface-engineered MNPs allow for successful capture and extraction of *Escherichia coli* from PBS[24]. Also, Kang et al. have reported that genetically engineered human opsonin functionalized MNPs can be used to successfully bind and extract *Staphylococcus aureus* or *Escherichia* coli from biological fluid[25]*.* Unfortunately, very few nanoparticles have been shown to bind *A. baumannii*. Also, many of the nanoparticles developed for bacterial capture are functionalized with genetically engineered, synthetic, or biomacromolecular ligands. Such surface functionalization may pose special challenges in achieving the Food and Drug Administration (FDA) approval required for many important applications. Furthermore, very few reports indicate bacterial capture in less than 1 hour. This is a notable unmet need because rapid extraction of bacteria is essential in order to allow effective decision-making in assessing potential pathogen contamination and to minimize risk of infection.

We have developed a novel colistin (Col) functionalized gold nanoparticle (AuNP) that is designed to rapidly capture *A. baumannii*. Colistin, a naturally occurring cationic decapeptide isolated from *Paenibacillus polymyxa* var. *colistinus*[53], is a potent broad-spectrum antimicrobial that was first used in the 1950s. The cationic colistin molecule and the negatively charged lipid A component of bacterial lipopolysaccharide (LPS) interact both electrostatically and hydrophobically[42,43], presumably allowing for colistin functionalized gold nanoparticle capture of *A. baumannii*. The amount of colistin conjugated to the AuNP surface was carefully designed to improve *A. baumannii* binding kinetics. Additional thiolated polyethylene glycol (PEG), lacking colistin, was used to passivate AuNP sites left unoccupied by colistin groups, thereby minimizing nonspecific interactions.

Utilizing colistin as a targeting ligand presents many advantages over synthetic, genetically engineered, or biomacromolecular ligands that have been used in this context[24,25,52]. One advantage is that colistin is a readily available, approved antibiotic that has been used in the clinical setting for decades. This design simplifies development and facilitates regulatory considerations relative to the use of genetically engineered or new biomacromolecular ligands. The effects of colistin surface presentation on the colistin functionalized gold nanoparticles were examined, and the results of *in vitro* binding kinetic experiments with *A. baumannii* are presented.

Materials and Methods

Materials

All materials were obtained from Sigma-Aldrich (St Louis, MO, USA) and used as received unless otherwise noted.

Methods

Synthesis of colistin functionalized gold nanoparticles (Col-PEG-AuNPs)

Col-PEG-AuNPs were prepared using a multistep approach

(i). *Conjugating Colistin to NHS-PEG$_{3400}$-OPSS tethers*. Colistin sulfate (Sigma-Aldrich, Batch # ALBN5158V) was suspended in 100 m*M* sodium bicarbonate ($NaHCO_3$) (Sigma-Aldrich, Lot # 017K0165) (pH 8.5) at a concentration of 0.29 mg/mL. NHS-PEG$_{3400}$-OPSS (succinimidyl ester-polyethylene glycol-ortho-pyridyl disulfide, Laysan Bio, Inc., Arab, AL, USA) was prepared in 100 m*M* $NaHCO_3$ at a concentration of 3.19 mg/mL. 900 µL of NHS-PEG$_{3400}$-OPSS solution was added in drop-wise fashion to 9 mL of colistin solution. The solution was vortexed for 10 seconds and then allowed to react at 4°C for 2 h.

(ii). *Attachment of Colistin-PEG$_{3400}$-OPSS onto AuNPs*. 1.425 mL of Colistin-PEG$_{3400}$-OPSS from step (i) and an additional 75 µL of 100 m*M* $NaHCO_3$ solution were added to 15 mL of 20 nm gold nanoparticle (AuNP) suspension (Ted Pella Inc., Redding, CA, USA, Lot # 012126). The solution was incubated at 21°C for 1 h.

(iii). *Passivation of Col-PEG-AuNPs with HS-mPEG$_{2000}$*. 109 µ*M* HS-mPEG$_{2000}$ (thiol-polyethylene glycol, Laysan Bio, Inc., Lot # 136-102) was prepared in distilled water. 1.5 mL of 109 µ*M* HS-mPEG$_{2000}$ solution was added to the Col-PEG-AuNPs resultant from step (ii), and then incubated at 21°C for 1 h. Following incubation, the functionalized nanoparticles were centrifuged at 8,000g (21°C) for 30 minutes. The supernatant was decanted and particles were resuspended in 70% ethanol. The solution was stored at 4°C for 24 h.

Synthesis of polyethylene glycol-functionalized gold nanoparticles (PEG-AuNPs)

PEG-AuNPs were prepared in three steps

(i). *Dilution of NHS-PEG$_{3400}$-OPSS*. NHS-PEG$_{3400}$-OPSS was prepared in 100 m*M* $NaHCO_3$ (pH 8.5) at a concentration of 3.19 mg/mL. 900 µL of NHS-PEG$_{3400}$-OPSS solution was added in drop-wise fashion to 9 mL of 100 m*M* $NaHCO_3$ solution. The solution was vortexed for 10 seconds and then stored at 4°C for 2 h.

(ii). *Attachment of NHS-PEG$_{3400}$-OPSS onto AuNPs*. 1.425 mL of NHS-PEG$_{3400}$-OPSS solution from step (i) and an additional 75 µL of 100 m*M* $NaHCO_3$ solution were added to 15 mL of 20 nm AuNP suspension. The solution was incubated at 21°C for 1 h.

(iii). *Passivation of PEG-AuNPs with HS-mPEG$_{2000}$.* 109 µ*M* HS-mPEG$_{2000}$ was prepared in distilled water. 1.5 mL of 109 µ*M* HS-mPEG$_{2000}$ solution was added to the PEG-AuNPs resultant from step (ii), and then incubated at 21°C for 1 h. Following incubation, the functionalized nanoparticles were centrifuged at 8,000g (21°C) for 30 minutes. The supernatant was decanted and particles were resuspended in 70% ethanol. The solution was stored at 4°C for 24 h.

Physical characterization of Col-PEG-AuNPs and PEG-AuNPs

Unconjugated AuNPs, Col-PEG-AuNPs, and PEG-AuNPs were centrifuged at 8,000g (21°C) for 30 minutes. The supernatant was decanted and particles were resuspended in nanopure water at a NP concentration of 0.5 m*M*. Droplets of diluted, aqueous NP suspensions were deposited on carbon film-backed copper grids (Ted Pella Inc., 400 mesh Cu, Lot # 250315) and blotted dry. Samples were left to dry for 2 h at 25°C prior to transmission electron microscopy (TEM) imaging on a 200 kV FEI Tecnai Osiris microscope (Hillsboro, OR, USA). X-rays emitted from the specimens were collected via four symmetrically arranged energy dispersive X-ray spectrometers. Signals from all four detectors were combined into one x-ray energy dispersive spectroscopy (EDS) spectrum to improve collection efficiency. EDS spectrums were created using Esprit imaging software (Bruker, Billerica, MA, USA). The specific energies of the EDS emission peaks were used to identify elements within each sample.

Confirmation of Colistin-PEG$_{3400}$-OPSS and NHS-PEG$_{3400}$-OPSS conjugation to AuNPs

Zeta potential measurements and size measurements were obtained with a Malvern Instruments Zetasizer (Malvern Nanosizer ZS, Malvern Instruments, U.K.) to determine surface charge and size of the Col-PEG-AuNPs, PEG-AuNPs, and unconjugated AuNPs. Each NP formulation was resuspended in dH_2O (pH 7.5) at an AuNP concentration of 1.0 m*M*, respectively.

H^1 NMR spectroscopy was used to confirm colistin conjugation to the Col-PEG-AuNPs.

H^1 NMR spectrums were recorded in deuterium oxide (D_2O, Cambridge Isotope Laboratories, Inc., Andover, MA, Lot #: D2OR-14-06), pH 7.4 using a Bruker 600 MHz spectrometer (Bruker, 600 MHz, Billerica, MA, USA). Col-PEG-AuNPs at a NP concentration of 5 m*M* were lyophilized for 24 h. The sample was resuspended in D_2O and then centrifuged at 8,000g (21°C) for 30 min. The supernatant was decanted and analyzed using H^1 NMR spectroscopy, prior to the iodination process described below.

The sample pellet was resuspended in D_2O and five iodine crystals were added. The iodinated Col-PEG-AuNP sample was vortexed for 10 s, every 20 min, for the total duration of 1 h. Iodine is a nucleophile and, therefore, attacks the disulfide group present in the OPSS-containing ligand[54]. During this reaction, nucleophilic substitution of iodine with the disulfide takes place, thereby causing quantitative decoupling of the OPSS-containing ligands from the surface of the AuNPs. Iodination of AuNPs reduces their aqueous solubility and forces them to spontaneously precipitate[55], leaving only OPSS-containing ligand and iodine in the supernatant.

Following 1 h of periodic vortexing, the sample was stored at 4°C for 24 h to allow the iodine crystals to settle at the bottom of the suspension. Then, only Colistin-PEG_{3400}-OPSS ligand remained in suspension and was extracted for analysis using H^1 NMR spectroscopy. The same procedure was used to analyze the NHS-PEG_{3400}-OPSS ligand of the PEG-AuNPs. Also, free colistin sulfate (500 ng) in D_2O was analyzed using H^1 NMR spectroscopy. This low concentration of free colistin sulfate was chosen for H^1 NMR analysis to prove that this method of analysis can detect the presence of colistin at minute concentrations.

Functionalized nanoparticle storage stability

The possibility of Colistin-PEG_{3400}-OPSS ligand disassembly from the surface of the Col-PEG-AuNPs was evaluated using H^1 NMR spectroscopy. Col-PEG-AuNPs (5 m*M*) were resuspended in PBS, pH 7.4 and stored at 21°C. After 24h, the Col-PEG-AuNP sample was centrifuged at 8,000g (21°C) for 30 minutes. Following centrifugation, the supernatant was decanted and analyzed using H^1 NMR spectroscopy to detect possible release of Colistin-

PEG_{3400}-OPSS ligands from the surface of the functionalized nanoparticles. This analysis was also performed 24h, 48h, 72h, and 7 days following Col-PEG-AuNP storage (21°C) in PBS, pH 7.4.

Cell culture

HepG2 cells (human liver carcinoma cancer cell line) were cultured in Dulbecco's modified Eagle's medium (DMEM, Gibco Cell Culture, Carlsbad, CA, USA) supplemented with 10% fetal bovine serum (FBS, Gibco) at 37°C in a humidified atmosphere containing 5% CO_2. HUVEC cells (human umbilical vein endothelial cell line) were cultured in vascular basal cell medium (American Type Culture Collection (ATCC) PCS-100-300, Manassas, VA, USA) supplemented with endothelial cell growth kit-VEGF (ATCC PCS-100-41) at 37°C in a humidified atmosphere containing 5% CO_2.

In vitro cytotoxicity studies

The cytotoxicity induced by Col-PEG-AuNPs, PEG-AuNPs, and free colistin sulfate on mammalian cell cultures was determined using the alamarBlue (Invitrogen Co., Carlsbad, CA, USA) assay[56]. HepG2 and HUVEC cells were seeded in clear, flat 96-well plates at a density of 10,000 cells/well in 200 µL of medium and incubated for 24 h at 37°C. Next, culture medium was removed and exchanged with medium containing fresh Col-PEG-AuNPs and PEG-AuNPs at concentrations of 2, 1, 0.5, 0.25, and 0 m*M,* respectively. Cells were also treated with free colistin sulfate at concentrations of 900, 90, 70, 15, 1 and 0 µ*M*. After incubation for 24 h at 37°C, cells were washed three times with phosphate buffer solution (PBS), pH 7.4 and treated with 200 µL of alamarBlue containing media. Cells were then incubated for an additional 4 h at 37°C. Fluorescence was quantified using a plate-reader (Tecan, Infinite M1000 Pro, Switzerland), with an excitation wavelength of 540 nm and emission wavelength of 590 nm.

In vitro hemocompatibility

Human whole blood was collected from anonymous, consenting human donors in accordance with an approved Institutional Review Board (IRB) protocol (IRB 111251). Red blood cells (RBCs) were isolated according to well-established protocols[57]. Four different concentrations (2, 1, 0.5, 0.25, and 0 m*M*) of Col-PEG-AuNPs and PEG-AuNPs were prepared in PBS, pH 7.4, respectively. Free colistin sulfate (900, 0.9, 0.4, 0.2, and 0 μ*M*) was also prepared in PBS, pH 7.4. Col-PEG-AuNPs, PEG-AuNPs, free colistin sulfate, positive control, and negative control were incubated with RBCs for 1h at 37°C, each respectively, at the concentrations outlined above. Following incubation, the samples were centrifuged (21°C) and the supernatant was spectrophotometrically analyzed for hemoglobin release using a plate-reader (Tecan, Infinite M1000 Pro) at 451 nm in order to determine percent hemolysis relative to the Triton-X positive control. Triton X-100 (Sigma-Aldrich) was diluted in diH_2O to result in a 20 v/v % Triton-X detergent concentration, which served as the positive control. The negative control used was PBS, pH 7.4. Percent of hemoglobin release was calculated according to the following equation:

$$\text{Hemoglobin release \%} = \frac{(Sample_{451\,nm} \;\; - \text{Negative control}_{451\,nm})}{(\text{Positive control}_{451\,nm} \; - \; \text{Negative control}_{451\,nm})} * 100\% \qquad (2.1)$$

A. baumannii strains and culture conditions

A. baumannii type strains ATCC 17978 and ATCC 19606 were obtained from the American Type Culture Collection (ATCC). Colistin-resistant variants of ATCC 19606 (designated 19606C) were isolated according to well-established procedures[58]. Briefly, *A. baumannii* strain ATCC 19606 was directly plated onto LB-agar (Lennox L Agar, Research Products International Corp., Lot # 32687) containing 4 μg/ml of colistin sulfate. Colistin-resistant colonies were identified at a frequency of approximately 1 in 10^8 after a single round of selection. All *A. baumannii* strains were maintained on LB-agar or cultured LB broth (Lennox L Broth, Research Products International Corp., Lot # 30728) at 37°C, with the addition of 4 μg/ml of colistin sulfate where appropriate.

A. baumannii binding

A. baumannii (ATCC 17978) was grown in LB broth at 37ºC, 200 rpm until reaching late log phase. The *A. baumannii* culture ($5x10^8$ CFU/ml, pH 7.4) was exposed to Col-PEG-AuNPs (1 m*M* NPs) for 1 hour at 37ºC, 200 rpm prior to centrifugation at 8,000g (21°C) for 20 min to pellet the cells. The supernatant was discarded, and the cells were washed two times with sterile DI water prior to imaging. To fix the cells, 2% formaldehyde was added, and the samples were incubated for 30 min at 21°C. Droplets of Col-PEG-AuNP bacteria suspension were deposited on carbon film-backed copper grids (Ted Pella Inc., 400 mesh Cu, Lot # 250315) and blotted dry. A 200 kV FEI Tecnai Osiris microscope was used for high angle annular dark field-scanning transmission electron microscopy (HAADF-STEM) imaging and simultaneous EDS spectrum analysis. Imaging was performed using the STEM mode capabilities of the microscope, thereby providing suitable conditions for high angle annular dark field imaging (HAADF). Data collection was carried out using the HAADF detector of the FEI Tecnai Osiris microscope, which collects scattered electrons emitted from the sample with an annular dark-field detector. By using HAADF-STEM, it was possible to form atomic resolution images, in which contrast is directly related to atomic number. This allowed for determination of the location and distribution of the Col-PEG-AuNPs with respect to the *A. baumannii*. The same procedure was repeated using PEG-AuNPs. Image analysis was carried using Bruker Esprit software.

AuNP standard concentration curve

The concentration of AuNPs was quantified using absorbance techniques, from which a standard concentration curve was generated. AuNPs were resuspended in PBS, pH 7.4 and diluted to various concentrations (2.0, 1.5, 1.0, 0.75, 0.5, 0.25, 0.12, 0 m*M*). 200 µL of each sample was plated in a 96-well plate. Absorbance was quantified using a plate-reader (Tecan, Infinite F500, Switzerland), with an absorbance wavelength of 492 nm. A standard concentration curve was generated from the data and is represented by the following equation:

$$y = 0.9193x + 0.014;\ R^2 = 0.9976 \tag{2.2}$$

where *x* represents AuNP concentration (m*M*) and *y* represents absorbance at 492 nm.

***A. baumannii* binding kinetics**

The rate of nanoparticle association to *A. baumannii* (ATCC 17978, ATCC 19606, ATCC

19606C) was analyzed using a spin filtration/absorbance technique. Initially, *A. baumannii* was grown in LB at 37ºC, 200 rpm until reaching late log phase. *A. baumannii* diluted in PBS, pH 7.4 ($5x10^8$ CFU/ml) was then exposed to Col-PEG-AuNPs (1 m*M*) and PEG-AuNPs (1 m*M*), respectively, for various times (0, 5, 10, 20, 30, 60, 120 min) prior to centrifugation at 4,900g (21°C) for 1 min to pellet the nanoparticle-bound bacteria. 200 µL of the supernatant was plated in a 96-well plate. Absorbance was quantified using a plate-reader (Tecan Infinite F500), with an absorbance wavelength of 492 nm. Results were then compared to the AuNP standard concentration curve in order to determine the concentration of nanoparticles unbound to bacteria. From this, the number of nanoparticles bound to bacteria was estimated. This procedure was completed for all three *A. baumannii* strains (ATCC 17978, ATCC 19606, ATCC 19606C).

Statistical analysis

All experiments were performed in triplicate. The results were expressed as the arithmetic mean ± standard deviation (SD). One-way analysis of variance (ANOVA) was used to determine whether there were any significant differences between the means of independent groups. Tukey's *post hoc* test was utilized to discriminate between groups of means. The factor was declared significant if the probability of the null hypothesis was less than 5% (*p-value* < 0.05).

Ethical compliance

Human whole blood was collected from anonymous donors in accordance with an approved IRB protocol (IRB 111251).

Results and Discussion

Preparation of Col-PEG-AuNPs and PEG-AuNPs

Colistin was tethered to AuNP surfaces using heterobifunctional PEG, as depicted in Figure 2.1. NHS was used to couple the PEG group to one of the five similarly reactive L-α-diaminobutyric acid (Dab) residues of colistin through the amine side chain of Dab[59]. Upon entering an aqueous environment, the NHS group of the NHS-PEG_{3400}-OPSS linker covalently binds to any single, comparably reactive amine residue of the colistin antibiotic via carbodiimide chemistry, resulting in an amide bond[60,61]. The disulfide group of the OPSS end of the heterobifunctional PEG has a strong affinity for the gold surface of the AuNPs[62]. Therefore, use of the PEG heterobifunctional linker enabled colistin decoration of the AuNP with a PEG molecular spacer, which was designed to reduce steric hindrance of colistin binding to bacteria. Thiolated PEG (HS-PEG$_{2000}$) was used to passivate the AuNP surface unoccupied by the Colistin-PEG$_{3400}$-OPSS. This additional PEG was intended to further passivate the Col-PEG-AuNPs, reduce nonspecific binding onto the gold surface, and sterically stabilize the NPs in both biological and non-biological fluids. In the range of physiological pH values, between pH 7.0 and 8.5, the primary amine groups of colistin were protonated, and, therefore, positively charged[63,64]. The positive charge of colistin allowed for binding to the negatively charged outer membrane of *A. baumannii*[42]. PEG-AuNPs were synthesized using a very similar, multistep approach, and used as a control group that lacked colistin decoration.

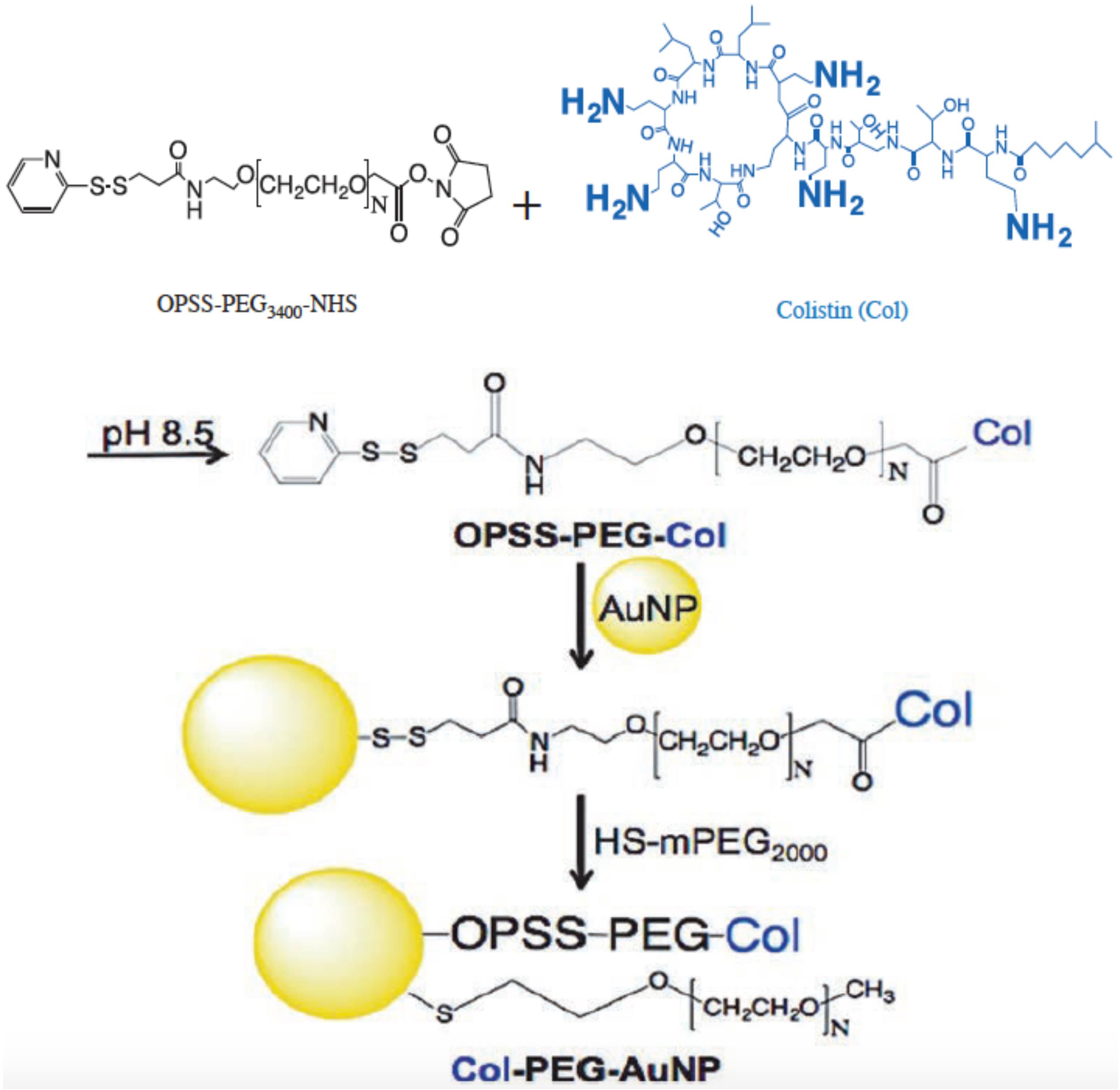

Figure 2.1. Synthesis scheme of Col-PEG-AuNP.

Characterization of functionalized AuNPs

TEM images consisted of highly mono-disperse NPs, as shown in Figure 2.2a-c, with an average NP core size of 23.2 nm. The EDS capabilities of the TEM confirmed the presence of gold in the NP core by characteristic X-rays at 2.120, 9.712, and 11.442 KeV (Fig 2.2d).

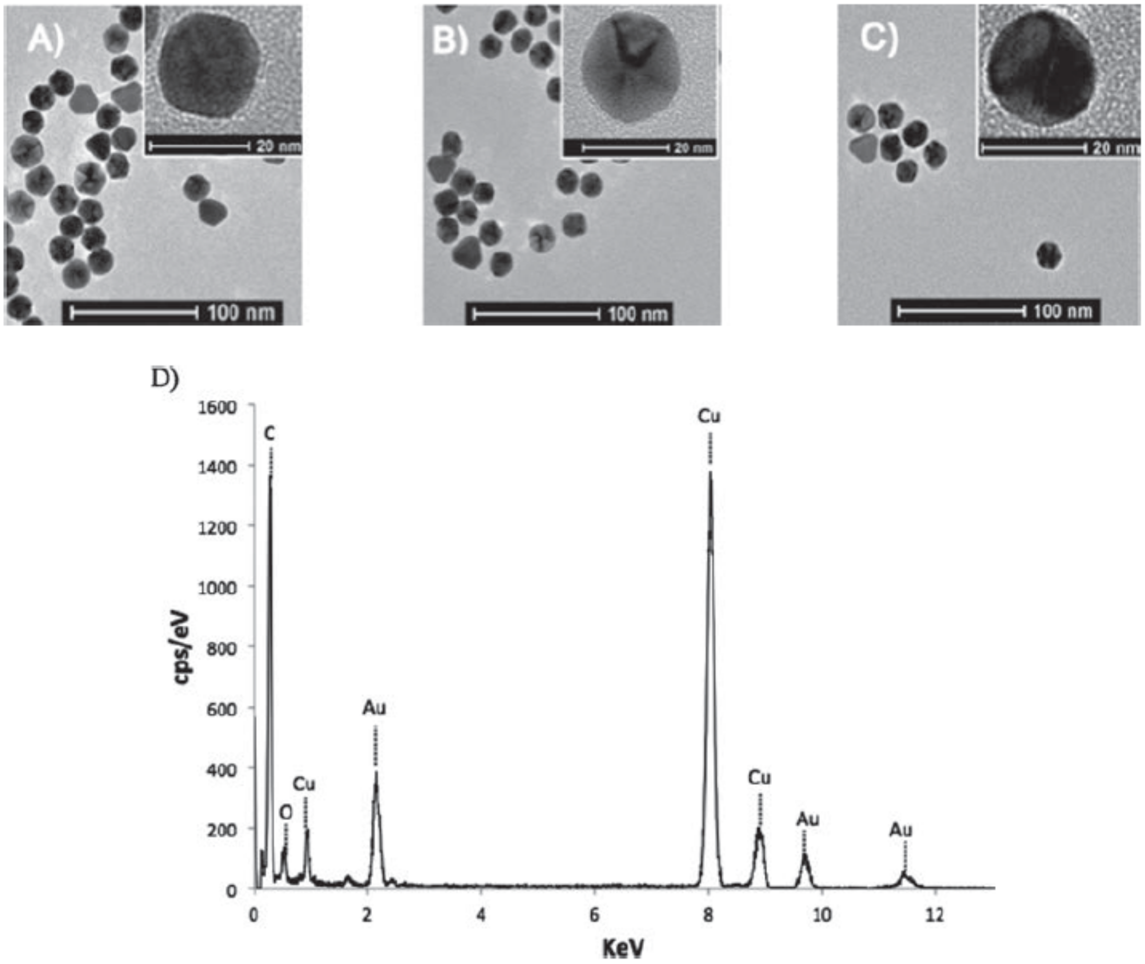

Figure 2.2. TEM, representative images of nanoparticles. (**a**) AuNP, (**b**) PEG-AuNP, (**c**) Col-PEG-AuNP. **d**, TEM-EDS of Col-PEG-AuNPs verified the presence of Au in the sample, confirming the nanoparticle core composition. The copper (Cu) signals were a result of the carbon film-backed copper grids used.

Confirmation of Colistin-PEG_{3400}-OPSS and NHS-PEG_{3400}-OPSS conjugation to AuNPs

The successful conjugation of Colistin-PEG_{3400}-OPSS and NHS-PEG_{3400}-OPSS to AuNPs was confirmed through zeta potential, size, and H^1 NMR spectroscopy measurements. The zeta potential of Col-PEG-AuNPs was significantly greater than control PEG-AuNPs or untreated AuNPs (Table 2.1). This increase in zeta potential was consistent with decoration of the AuNPs with strongly cationic colistin.

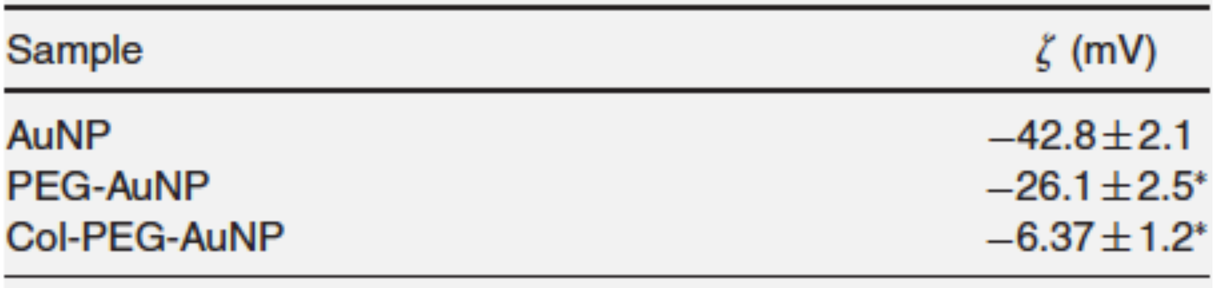

Sample	ζ (mV)
AuNP	-42.8 ± 2.1
PEG-AuNP	$-26.1 \pm 2.5^{*}$
Col-PEG-AuNP	$-6.37 \pm 1.2^{*}$

Table 2.1. Functionalization of AuNPs with NHS-PEG$_{3400}$-OPSS or Colistin-PEG$_{3400}$-OPSS significantly increased AuNP zeta potential (ζ) towards more positive values. ANOVA and Tukey's *post hoc* test prove that both Col-PEG-AuNP and PEG-AuNP zeta-potentials are significantly different than AuNP zeta-potential. Also, Col-PEG-AuNP and PEG-AuNP zeta-potentials are significantly different comparatively. $^{*}p < 0.05$

Passivating the AuNPs through PEGylation alone reduced the zeta potential of untreated AuNPs, presumably due to the partial shielding of the original surface charge. The addition of colistin to the Col-PEG-AuNPs further increased the zeta potential, presumably due to the colistin molecule corona, which is cationically charged at physiological pH values.

Size measurements of the PEG-AuNPs and Col-PEG-AuNPs (Fig 2.3a) supported ligand conjugation to the AuNPs and allowed an estimation of ligand length. The Colistin-PEG_{3400}-OPSS ligand was approximately 8.5 nm in length when bound to AuNPs, based on a diameter that was roughly 17 nm larger than that of unconjugated AuNPs. Conjugation of NHS-PEG_{3400}-OPSS had a similar effect on size, thereby providing further confidence of the successful generation of PEG-AuNPs.

The hydrodynamic radii of Col-PEG-AuNPs were smaller than those of PEG-AuNPs, as reported by DLS (Fig 2.3b). Attraction of the positively charged colistin molecules to the negatively charged AuNP surface was presumed to change the PEG linker conformation, resulting in the observed decrease in ligand length, relative to PEG-AuNPs that have a much greater negative zeta potential.

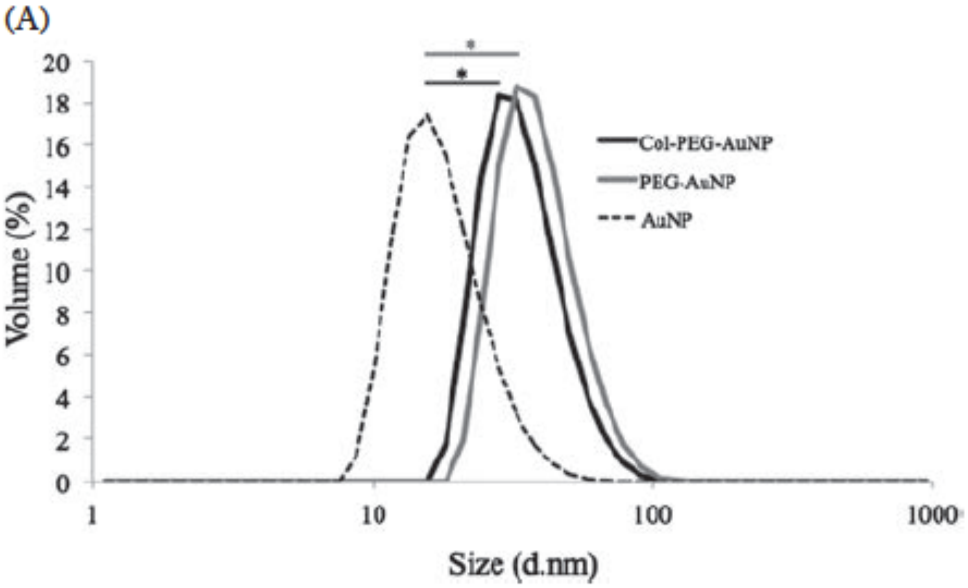

(B)

Sample	Size (d.nm)
AuNP	23.3±1.2
PEG-AuNP	45.3±2.3*
Col-PEG-AuNP	39.4±2.5*

Figure 2.3. Functionalization of AuNPs with NHS-PEG$_{3400}$-OPSS or Colistin-PEG$_{3400}$-OPSS significantly increased AuNP size. **a**, Nanoparticle diameter (d) was estimated by DLS. **b**, Mean size of each nanoparticle. ANOVA and Tukey's *post hoc* test prove that both Col-PEG-AuNP and PEG-AuNP size are significantly different than AuNP size. Also, Col-PEG-AuNP and PEG-AuNP size are significantly different comparatively. $*p < 0.05$

H^1 NMR spectroscopy confirmed conjugation of colistin to the AuNPs (Fig 2.4a). The Colistin-PEG$_{3400}$-OPSS ligands were treated with iodine to decouple the ligands from the AuNP surface and then measured using H^1 NMR[65]. This decoupling approach was utilized in order to prevent peak broadening due to the presence of AuNPs in the sample.

H^1 NMR results are shown in Figure 2.4, with the supernatant from iodine treated Col-PEG-AuNPs shown in Figure 2.4a and free colistin sulfate shown in Figure 2.4b. The protonated amine groups of colistin are identifiable in both spectrums (Fig 2.4a, 8.31ppm; Fig 2.4b, 8.38 ppm), consistent with successful conjugation of colistin to the AuNPs. Conjugation of colistin to the PEG$_{3400}$-OPSS linker was expected to cause diamagnetic shielding, increasing the electron density surrounding the colistin molecule. The physical shift of the protonated colistin amine peak upfield, as seen by comparing Figure 2.4a to Figure 2.4b, is consistent with diamagnetic shielding and is further evidence that the colistin was bound to the PEG$_{3400}$-OPSS linker.

The supernatant of Col-PEG-AuNPs without the addition of iodine was also analyzed using H^1 NMR (Fig 2.4c) over the course of 7 days. This analysis was performed in order to estimate the amount of colistin containing molecules that were not particle bound and possibly released from the surface of the nanoparticles over time. The relative gain and number of counts taken to generate the H^1 NMR spectrums of the non-iodinated Col-PEG-AuNP samples were scaled to allow direct comparison to the iodinated Col-PEG-AuNP H^1 NMR spectrum.

Due to the absence of a protonated amine peak (8.31 ppm) in the H^1 NMR spectrum of non-iodinated Col-PEG-AuNPs (Fig 2.4c), it was concluded that the amount of colistin ligand released from the surface of the nanoparticles was below the NMR mass limit of detection (500 ng), and, therefore, insignificant. Stoichiometry of the reaction and H^1 NMR data support a concentration of colistin bound to particles of 3.9 μ*M* colistin/mg AuNP, or 3400 colistin ligands per AuNP. This reflects approximately 95% of total AuNP surface coverage, based on a 0.35 nm^2 PEG footprint area[66]. This was the maximum number of colistin containing ligands that could be loaded onto the surface of a single AuNP while remaining water dispersible. The H^1 NMR spectrum of iodine treated PEG-AuNPs is shown in Figure 2.4d. It can be seen that no signal was present at 8.31 ppm, indicating the absence of colistin in the sample.

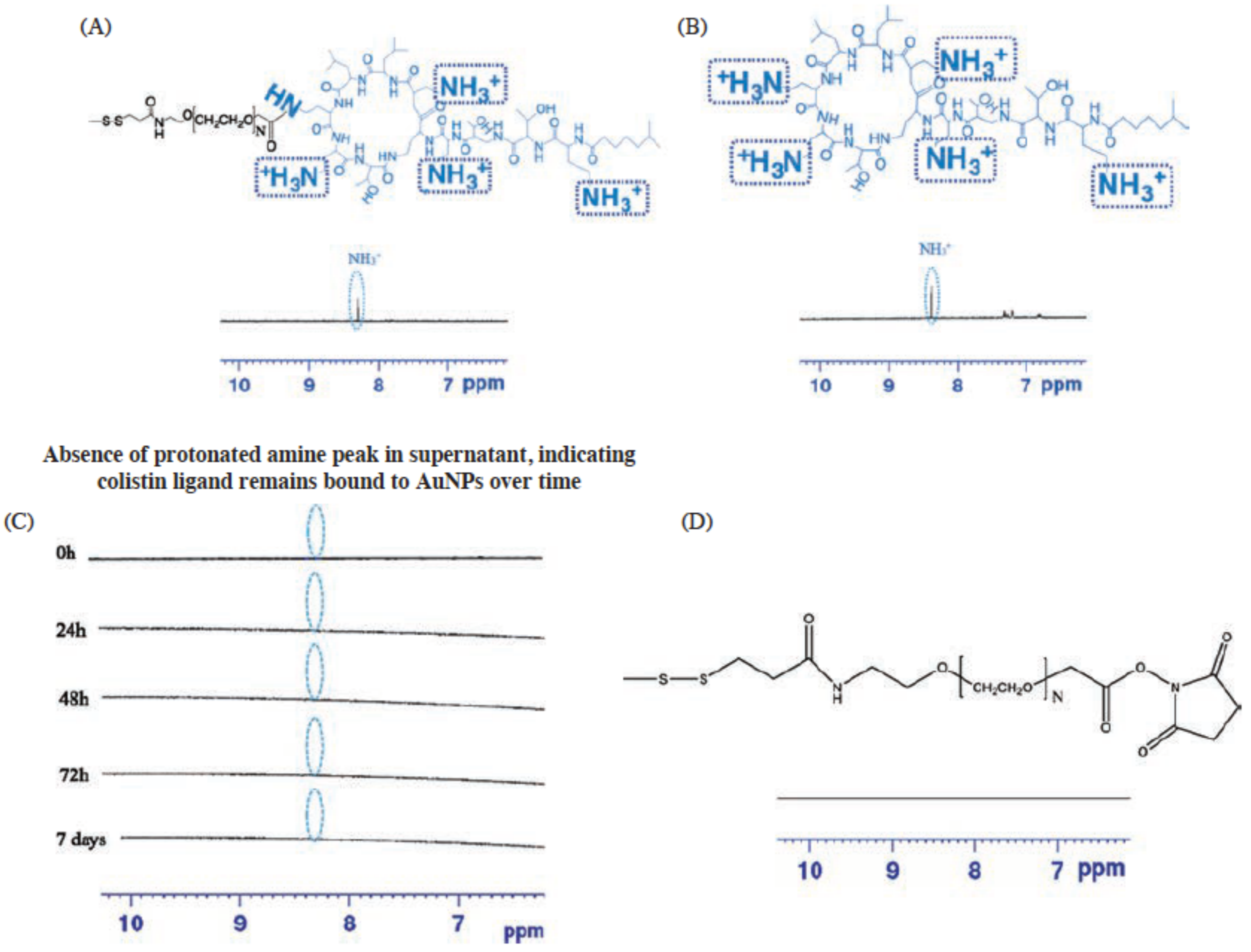

Figure 2.4. H^1 NMR spectrums of Col-PEG-AuNP supernatant verified that the colistin-containing molecules were bound to AuNPs. **a**, Supernatant of iodinated Col-PEG-AuNPs. The peak indicated at 8.31 ppm was assigned to the protonated amine groups of colistin. The presence of protonated amine groups in (a) confirmed successful colistin conjugation. **b**, Free colistin sulfate (mass of 500 ng). The peak indicated at 8.38 ppm was assigned to the protonated amine groups of colistin. **c**, Supernatant of pelleted, non-iodinated Col-PEG-AuNPs stored in PBS, pH 7.4 (21ºC). Following 0h, 24h, 48h, 72h, and 7 days, no peak was present at 8.31 ppm, indicating a colistin concentration lower than the limit of detection. This demonstrates that no significant amount of colistin ligand was released from the surface of the nanoparticles during storage. **d**, Supernatant of iodinated PEG-AuNPs. No peak was present at 8.31 ppm, indicating the absence of colistin.

In vitro cytotoxicity studies

AlamarBlue is a cell membrane-permeable dye that both changes fluorescent properties and color in response to a chemical reduction caused by cell metabolic activity[67]. With alamarBlue it is possible to compare control group cell viability against experimental group cell viability, from which cytotoxicity can be analyzed quantitatively. After a 24 h incubation period, the cell viability of mammalian cells treated with Col-PEG-AuNPs or PEG-AuNPs was no different than untreated cells (Ctrl) (Fig 2.5a, 2.5b).

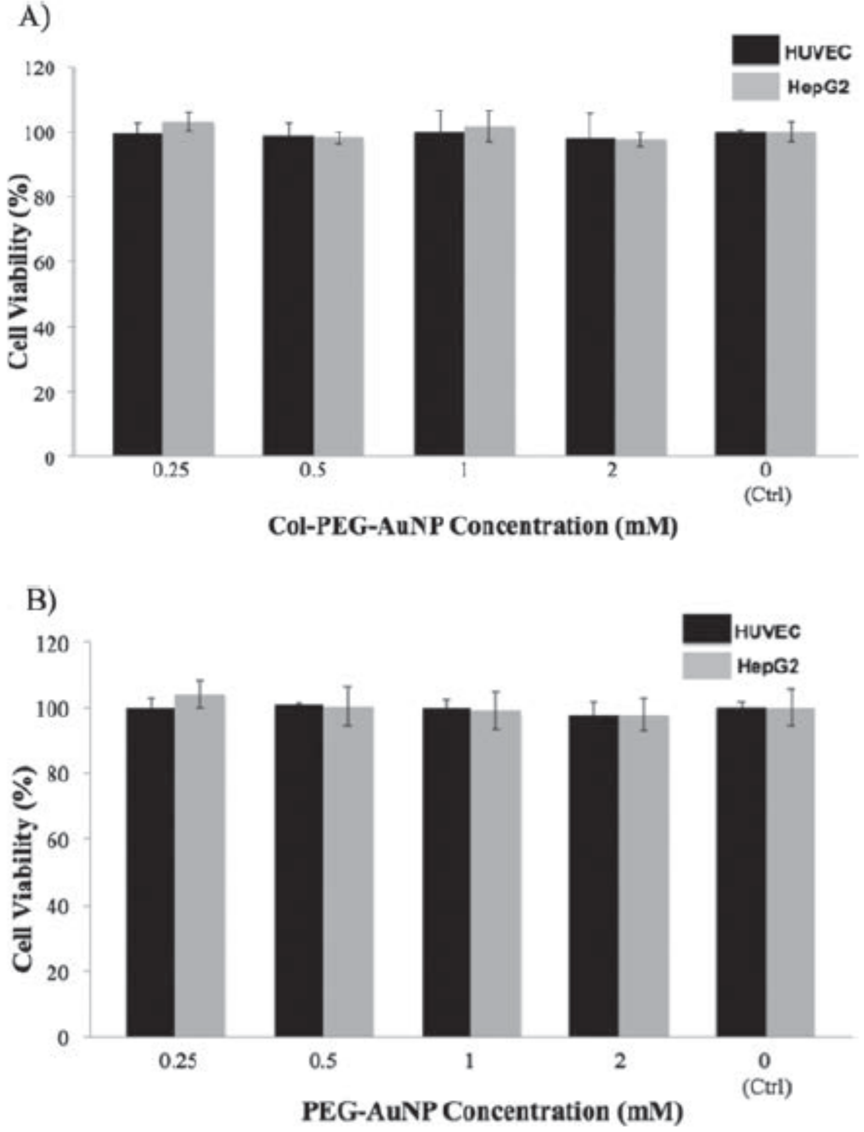

Figure 2.5. (a) Col-PEG-AuNPs and (b) PEG-AuNPs demonstrated cellular compatibility with HUVEC and HepG2 cells. HUVEC and HepG2 cells were treated with different nanoparticle formulations at various concentrations. **a**, HUVEC and HepG2 cell viability was quantified by the alamarBlue viability assay following 24 h treatment with Col-PEG-AuNPs. **b**, HUVEC and HepG2 cell viability was quantified by the alamarBlue viability assay following 24 h treatment with PEG-AuNPs. Treatment with Col-PEG-AuNPs or PEG-AuNPs did not cause cell toxicity. Data were normalized to control cells (Ctrl, 0.0), and are shown as mean ± SD (*n* = 3). (*p*-values not significant).

Free colistin cytotoxicity was also evaluated *in vitro* using HepG2 and HUVEC mammalian cell lines with alamarBlue[56]. Cell viability above 90% was observed with free colistin sulfate concentrations equal to or less than 90 µ*M*. In comparison, cell viability of only approximately 80% was observed when administering colistin sulfate at a concentration of 900 µ*M* (Fig 2.6).

The two forms of colistin commercially available are colistin sulfate and colistimethate sodium. It is recommended that colistin sulfate be used for colistin susceptibility testing[59]. However, colistimethate sodium is the less toxic of the two and, therefore, is used more frequently for parenteral use. After inactive colistimethate sodium is delivered parenterally, it is hydrolyzed in order to be converted to colistin and, therein, exhibit antibacterial activity[59]. The intravenous colistimethate sodium dosage recommended in the United States for sepsis treatment is about 13 mg/kilogram (kg) of body weight per day[59]. The recommended doses for colistin base activity are 2.5–5 mg/kg per day in two to four divided doses. This is equivalent to about 6.67–13.3 mg/kg of colistimethate sodium per day[59].

Based on a 105 patient study by Nation et al., the steady-state plasma concentration of colistin ranges from 0.48 to 9.38 mg/liter (average 2.36 mg/liter) following a 200 mg median daily dose of colistin base activity[68]. This steady-state plasma concentration of 0.48 to 9.38 mg colistin/liter is equivalent to 0.42 µ*M* to 8.1 µ*M* colistin concentration. Therefore, the 90 µ*M* colistin sulfate concentration evaluated in the mammalian cell culture model significantly exceeds the upper limit of steady-state plasma concentrations of colistin base activity.

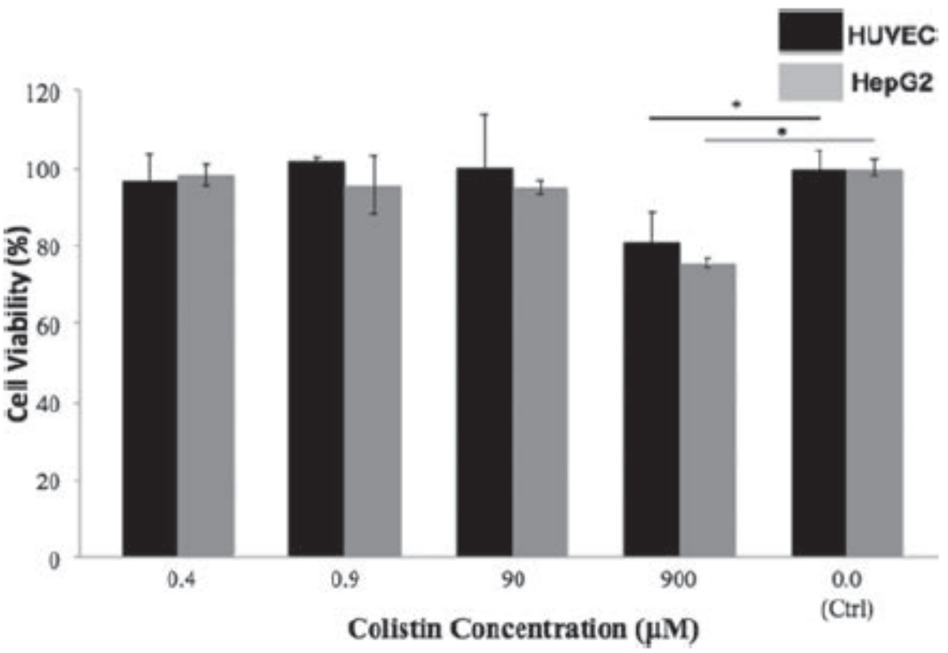

Figure 2.6. Cellular toxicity was not induced by free colistin sulfate at concentrations less than 90 μ*M*. HUVEC and HepG2 cell viability was quantified by the alamarBlue viability assay following 24 h treatment with colistin. Treatment with colistin sulfate caused cellular toxicity at a colistin sulfate concentration of 900 μ*M* in both cell types. Data were normalized to control cells (Ctrl, 0), and are shown as mean ± SD ($n = 3$). $^*p < 0.05$ compared to Ctrl.

***In vitro* hemocompatibility**

Avoiding destabilization and nonspecific interactions with cells and other blood components is key to general hemocompatibility and important for future applications of these materials in contact with blood. A design goal was to maximize the allowable duration for blood contact time with NPs in order to allow for passive bacterial association or active bacterial targeting by intact, bioactive NPs. *Ex vivo* experiments in human whole blood were done to measure nonspecific RBC interactions and the stability of AuNPs. After 1 h incubation in a solution of isolated RBCs, Col-PEG-AuNPs, PEG-AuNPs, and free colistin sulfate were retained in the serum fraction and did not cause hemolysis (Table 2.2, Table 2.3). PEGylation improves hemocompatibility of similarly sized NPs[69], and we hypothesized that surface PEGylation could be an avenue to further enhance stability. The PEGylation design presumably contributed to the observed lack of adverse interactions between blood cells and Col-PEG-AuNPs. Greater opportunity for Col-PEG-AuNP interaction with *A. baumannii* is one consequence of the extended allowable blood contact time exhibited by these NPs.

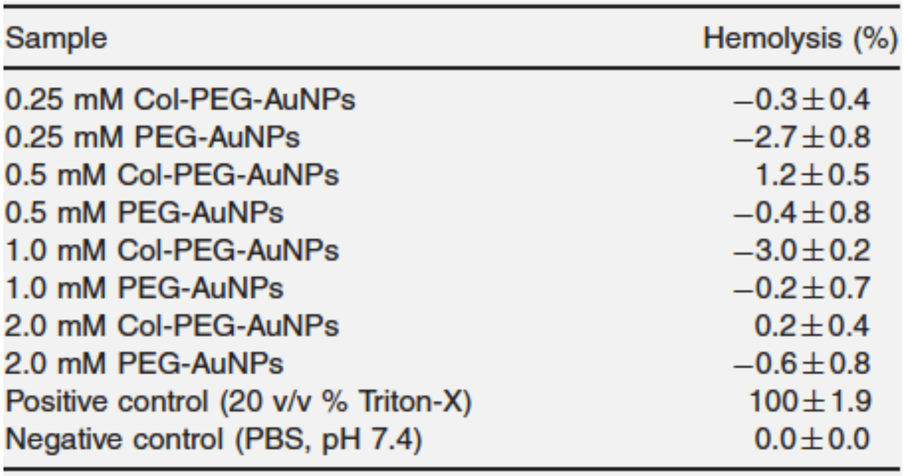

Sample	Hemolysis (%)
0.25 mM Col-PEG-AuNPs	−0.3 ± 0.4
0.25 mM PEG-AuNPs	−2.7 ± 0.8
0.5 mM Col-PEG-AuNPs	1.2 ± 0.5
0.5 mM PEG-AuNPs	−0.4 ± 0.8
1.0 mM Col-PEG-AuNPs	−3.0 ± 0.2
1.0 mM PEG-AuNPs	−0.2 ± 0.7
2.0 mM Col-PEG-AuNPs	0.2 ± 0.4
2.0 mM PEG-AuNPs	−0.6 ± 0.8
Positive control (20 v/v % Triton-X)	100 ± 1.9
Negative control (PBS, pH 7.4)	0.0 ± 0.0

Table 2.2. After 1 h incubation in a solution of isolated RBCs, Col-PEG-AuNPs and PEG-AuNPs were retained in the serum fraction and did not cause hemolysis. Four different concentrations of Col-PEG-AuNPs (2, 1, 0.5, 0.25, and 0 m*M*) and PEG-AuNPs (2, 1, 0.5, 0.25, and 0 m*M*) were prepared in PBS, pH 7.4, respectively. Samples were made in quadruplicate and hemolysis experiments were performed in quadruplicate. Triton-X (20 v/v %) was used as a positive control. The results were expressed as the arithmetic mean ± standard deviation (SD).

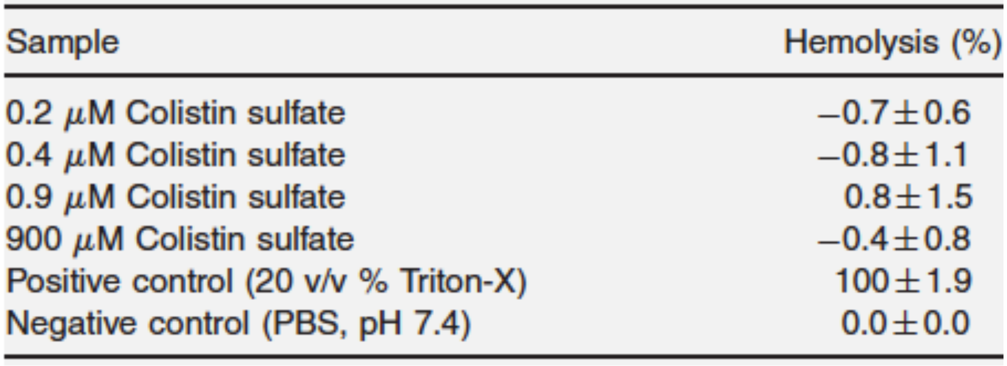

Sample	Hemolysis (%)
0.2 μM Colistin sulfate	−0.7 ± 0.6
0.4 μM Colistin sulfate	−0.8 ± 1.1
0.9 μM Colistin sulfate	0.8 ± 1.5
900 μM Colistin sulfate	−0.4 ± 0.8
Positive control (20 v/v % Triton-X)	100 ± 1.9
Negative control (PBS, pH 7.4)	0.0 ± 0.0

Table 2.3. After 1 h incubation in a solution of isolated RBCs, colistin sulfate was retained in the serum fraction and did not cause hemolysis. Four different concentrations of colistin sulfate (0.2, 0.4, 0.9, and 900 μ*M*) were prepared in PBS, pH 7.4, respectively. Samples were made in quadruplicate and hemolysis experiments were performed in quadruplicate. Triton-X (20 v/v %) was used as a positive control. The results were expressed as the arithmetic mean ± standard deviation (SD).

Nanoparticle binding to *A. baumannii*

The primary component of the outer membrane of Gram-negative bacteria, including *A. baumannii*, is LPS. LPS is composed of lipid A, a core oligosaccharide, and an outer polysaccharide. Lipid A is the innermost aspect of the LPS, as well as the most conserved component of the structure[70]. The proposed binding mechanism between colistin and *A. baumannii* involves lipid A. At physiological pH values, the primary amine groups of the colistin heptapeptide ring and fatty acid tail become protonated, thereby allowing electrostatic interactions with the negatively charged phosphate groups of lipid A[42]. Initial electrostatic interaction between colistin and *A. baumannii* leads to hydrophobic interaction between the fatty acid tail of colistin and the acyl chains of lipid A[43]. The conjugation chemistry of Colistin-PEG_{3400}-OPSS was designed to preserve and protect the molecular characteristics of colistin that are responsible for antibiotic activity and binding to *A. baumannii*. Conjugation of colistin to the heterobifunctional PEG was hypothesized to use any single, similarly reactive amine group of the colistin heptapeptide ring. This colistin conformation leaves the four remaining, comparably reactive protonated amine groups of colistin in their active state and free to interact with the cell envelope of *A. baumannii*.

Col-PEG-AuNPs associated with the cell envelope of *A. baumannii* (ATCC 17978), as imaged by STEM (Fig 2.7a). High-angle annular dark-field (HAADF)-STEM analysis of Col-PEG-AuNPs association with *A. baumannii* (ATCC 17978)*,* Figure 2.7b, verified that gold (Au) and nitrogen (N) were present in the sample, thereby confirming the presence of Col-PEG-AuNPs and bacteria[71,72]. In the HAADF-STEM image shown in Figure 2.7b, contrast is directly related to atomic number. This allowed for identification of chemical elements present in the sample. In this case, gold was pseudocolored to identify the Col-PEG-AuNPs (Fig 2.7c), whereas nitrogen was pseudocolored to identify the bacteria (Fig 2.7d). Further analysis of Figure 2.7b provided the complete elemental make-up of the sample (Fig 2.7, Fig 2.9). Figures 2.7a and 2.7b suggest that

Col-PEG-AuNPs attached to the surface of *A. baumannii*. PEG-AuNPs did not bind to the bacterial surface (Fig 2.7e), confirming that colistin is an effective targeting ligand. The HAADF-STEM image shown in Figure 2.7f allowed for identification of chemical elements present in the PEG-AuNP sample. The EDS spectrum (Fig 2.10) verified the presence of bacteria through elemental analysis, but elemental gold was not present in the sample (Fig 2.7g, Fig 2.7h), indicating that PEG-AuNPs did not bind to *A. baumannii*.

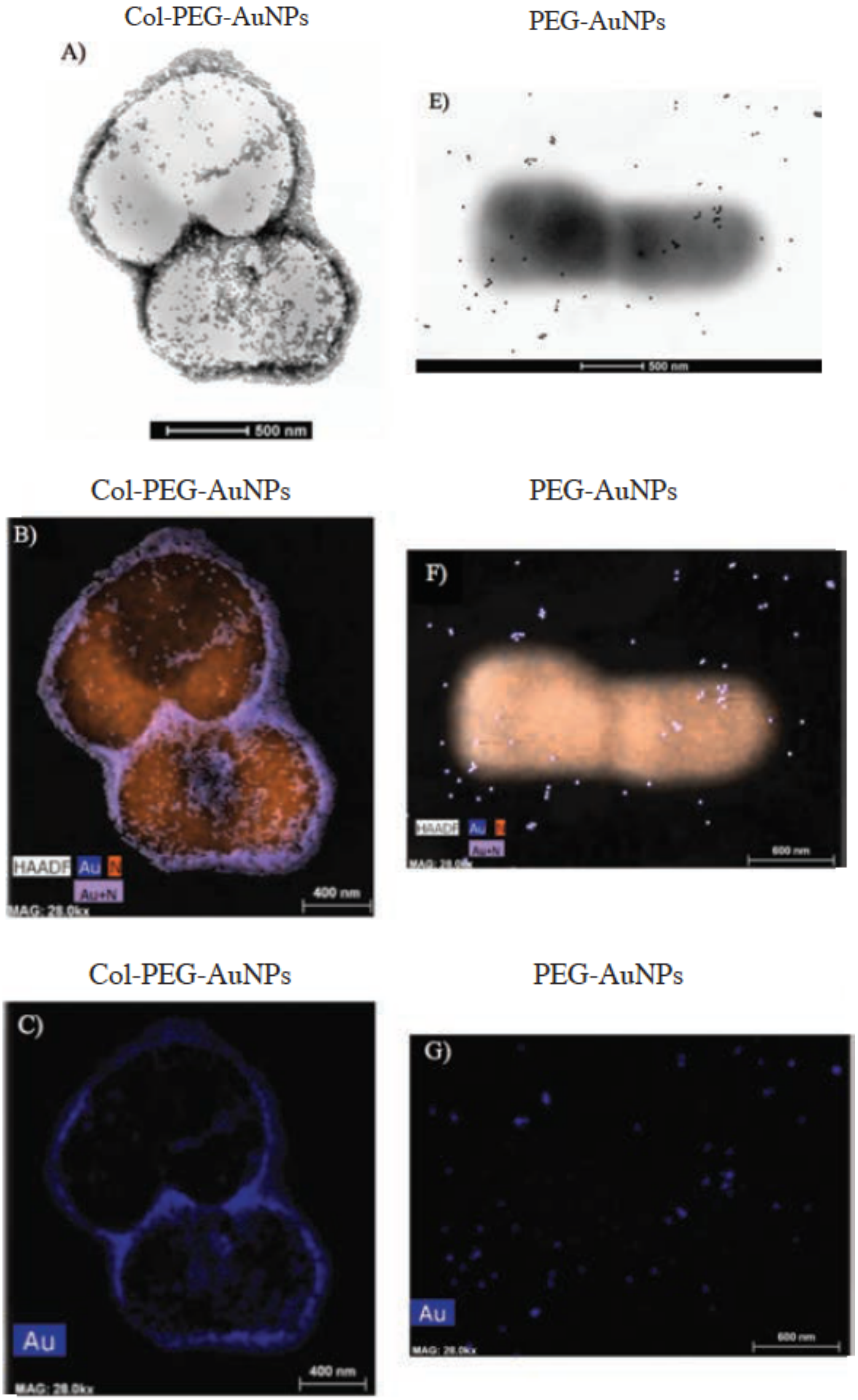

Col-PEG-AuNPs

PEG-AuNPs

Col-PEG-AuNPs

PEG-AuNPs

Col-PEG-AuNPs

PEG-AuNPs

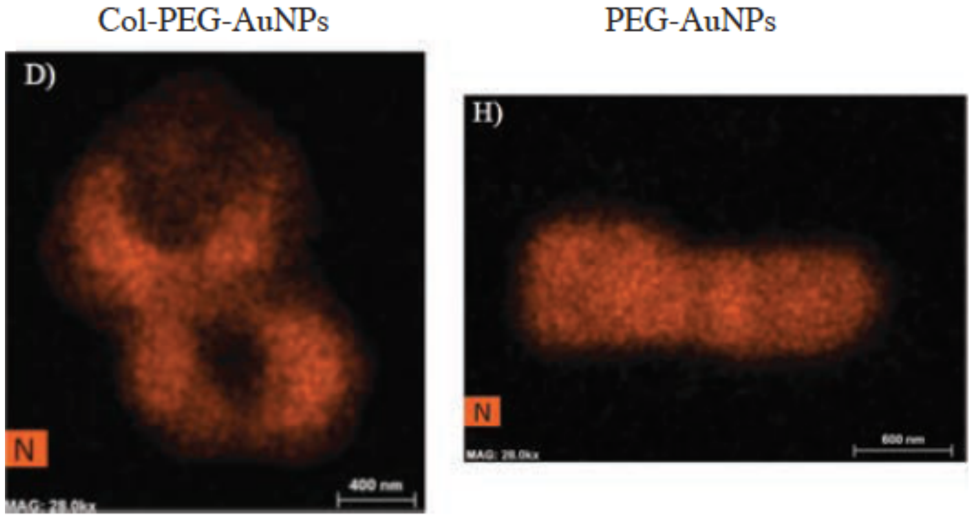

Figure 2.7. HAADF-STEM imaging of Col-PEG-AuNP association with *A. baumannii* (ATCC 17978) (a & b) suggests that the targeting ligand of colistin is required for nanoparticle binding to *A. baumannii*. **a**, STEM of Col-PEG-AuNPs bound to *A. baumannii*. **b**, HAADF-STEM view of the sample analyzed in panel (a). The sample was analyzed using HAADF techniques to form atomic resolution images in which gold (**c**) and nitrogen (**d**) are pseudo-colored. **e**, STEM of PEG-AuNPs incubated with *A. baumannii*. **f**, HAADF-STEM view of the sample analyzed in panel (e). The sample was evaluated for the presence of gold (**g**) and nitrogen (**h**) using HAADF techniques. The lack of gold in (g) indicates that PEG-AuNPs were not associating with *A. baumannii.*

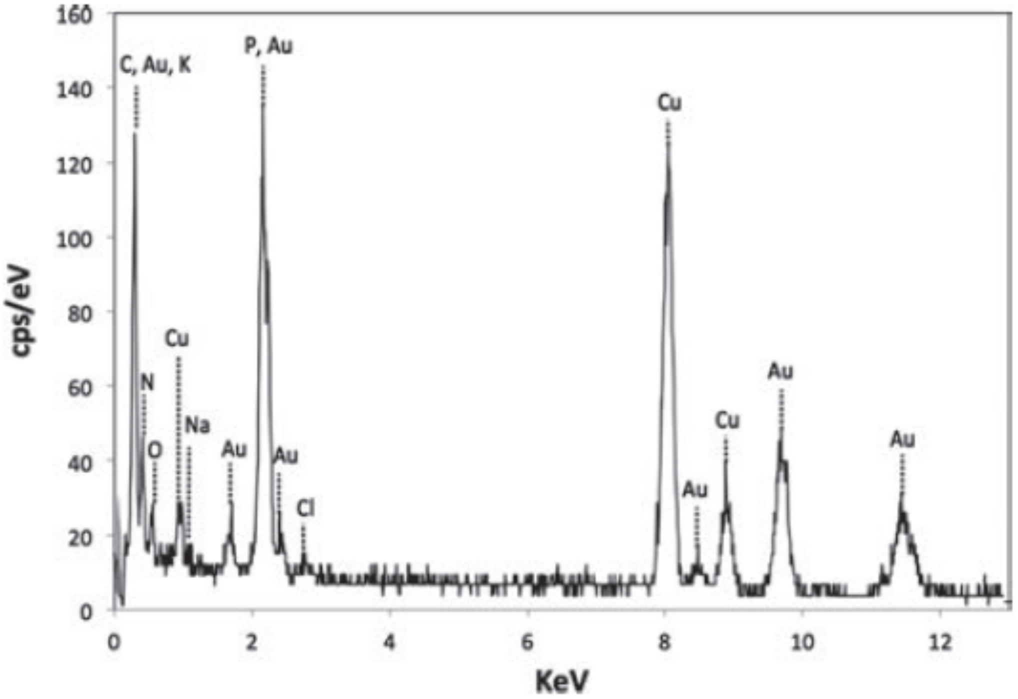

Figure 2.8. EDS spectrum of Figure 2.7b confirmed that Col-PEG-AuNPs, indicated by Au peaks, were associated with *A. baumannii*, indicated by phosphate (P), potassium (K), sodium (Na), nitrogen (N), and chlorine (Cl) peaks. The Cu signals were a result of the carbon film-backed copper grids used.

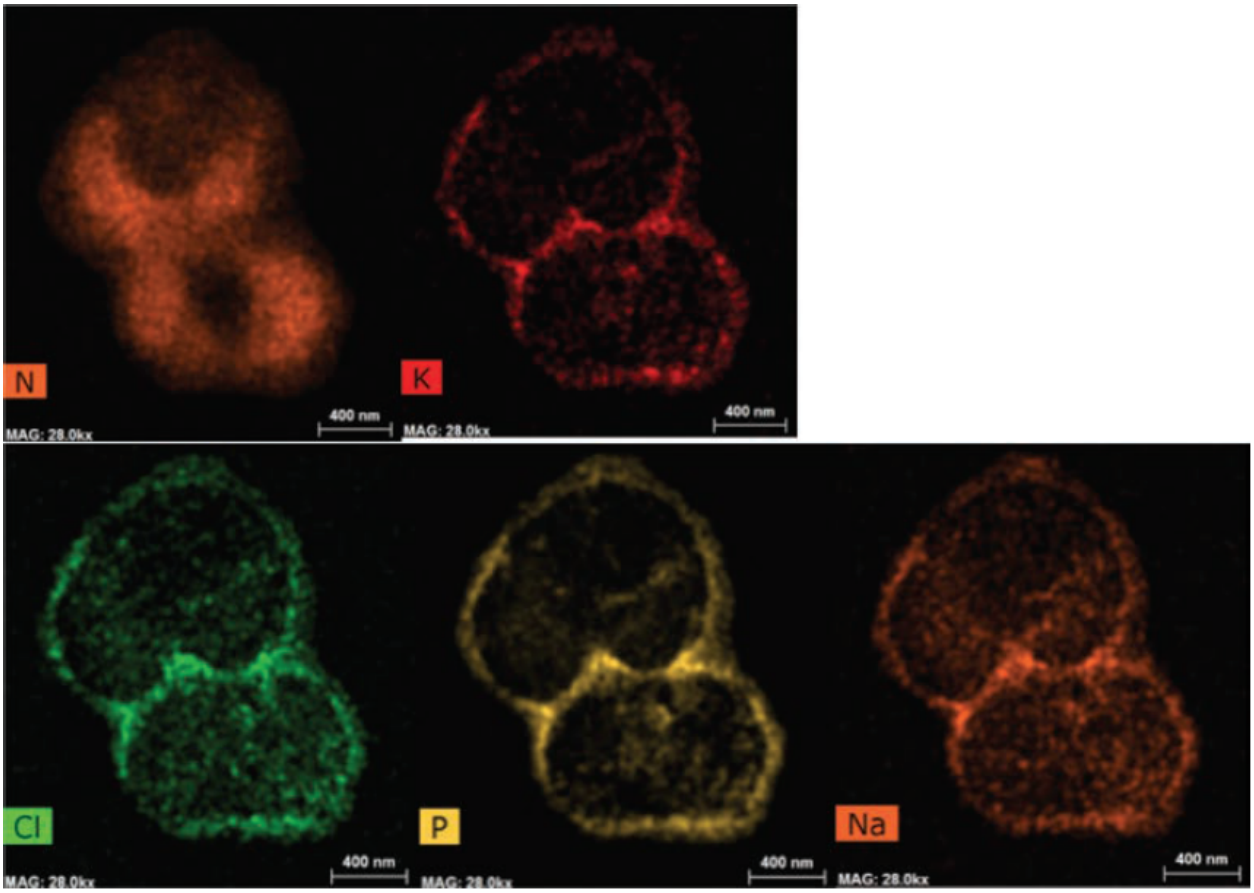

Figure 2.9. HAADF-STEM images in combination with EDS further confirmed the elemental composition of *A. baumannii*. N, K, Cl, P, and Na are the core elements that make up *A. baumannii*.

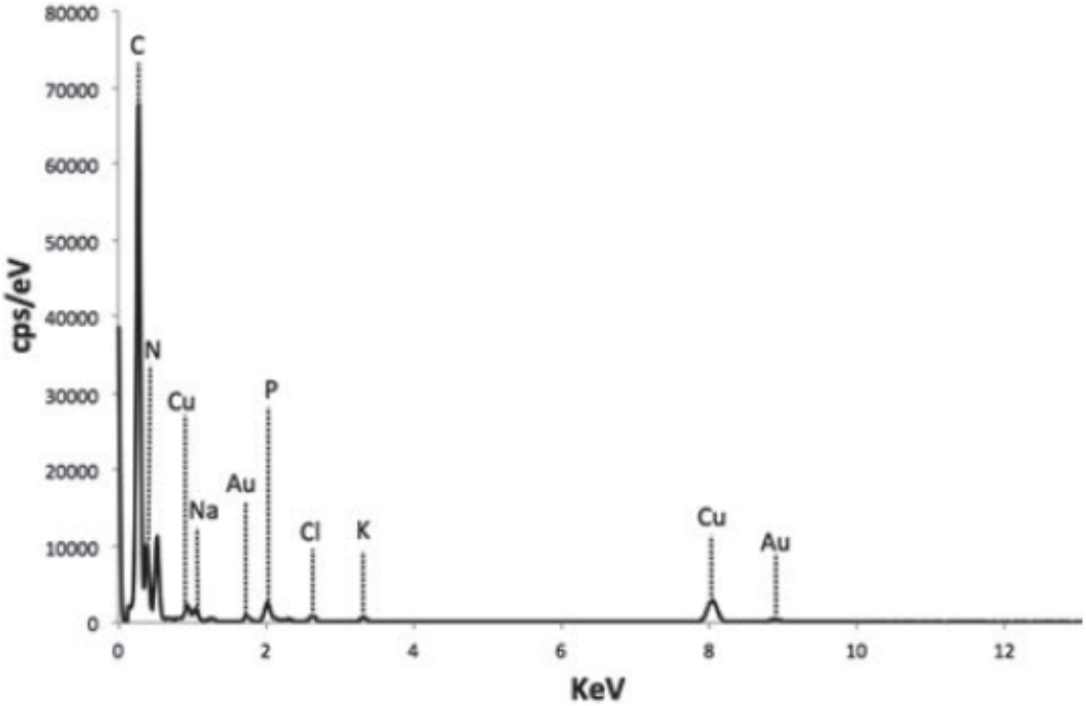

Figure 2.10. EDS spectrum of PEG-AuNPs incubated with *A. baumannii* lacks Au, indicating that PEG-AuNPs were not bound to *A. baumannii*. P, K, Na, and Cl peaks confirmed the presence of bacteria. The Cu signals were a result of the carbon film-backed copper grids used.

***A. baumannii* binding kinetics**

Col-PEG-AuNP binding to *A. baumannii* was characterized as a function of the extent of colistin decoration per NP (Col:NP ratio), holding the NP:*A. baumannii* ratio constant. Fastest binding occurred when using a 3.9 µ*M* colistin concentration functionalized to the AuNP surface, which is consistent with colistin base plasma concentrations seen in the clinical setting[68]. To achieve a 3.9 µ*M* colistin concentration, approximately 3400 Colistin-PEG_{3400}-OPSS ligands were bound to a single AuNP, based on the molecular dimensions of PEG and number of AuNPs. The kinetics of Col-PEG-AuNP association with *A. baumannii* was characterized by a spin filtration technique as described in the Methods section. Following the addition of *A. baumannii* to Col-PEG-AuNPs, the rate of association was evaluated over a 2 h time period. Col-PEG-AuNP association with *A. baumannii* was analyzed using three different strains of *A. baumannii*, which included ATCC 17978, ATCC 19606, and ATCC 19606C (colistin resistant).

Nanoparticle attachment to *A. baumannii* was dependent upon the presence of the colistin targeting ligand, as shown in Figure 2.11. The rate of Col-PEG-AuNP binding to *A. baumannii* is described by a two-parameter, exponential curve in the form of:

$$\mathrm{A} = \mathrm{A}_{Max} * \left(1 - e^{-t/\tau}\right) \tag{2.3}$$

where A (number) represents the number of Col-PEG-AuNPs bound to a single *A. baumannii*, and t (min) represents time. The constants for the exponential curve are A_{Max} (maximum number of Col-PEG-AuNPs per *A. baumannii*), the final asymptotic value of this system, and τ (min), the time constant.

The maximum number of Col-PEG-AuNPs bound to a single *A. baumannii* (A_{Max}) varied from strain to strain. It was estimated that A_{Max} is approximately equal to 1228 Col-PEG-AuNPs per *A. baumannii* ATCC 19798 (Fig 2.11a). The time constant, τ, represents the time required for 63% of maximal Col-PEG-AuNP binding per *A. baumannii*, or A_{Max}. In this system, τ is equivalent to 9.6 minutes. Therefore, in describing Col-PEG-AuNP binding to *A. baumannii* strain ATCC 17978, Equation (2.3) can be more completely represented as:

$$\mathrm{A} = 1228 * \left(1 - e^{-t/9.6}\right) \tag{2.4}$$

Half-maximal binding in this case occurs when A is equal to half of A_{Max}, or when 614 Col-PEG-AuNPs are bound to a single *A. baumannii* ATCC 17978 cell (~6.7 min).

It was estimated that A_{Max} is approximately equal to 1182 Col-PEG-AuNPs per *A. baumannii* ATCC 19606 (Fig 2.11b). The time constant, τ, is equivalent to 10.2 minutes. Therefore, in describing Col-PEG-AuNP binding to *A. baumannii* strain ATCC 19606, Equation (2.3) can be represented as:

$$\mathrm{A} = 1182 * (1 - e^{-t/10.2}) \tag{2.5}$$

Half-maximal binding in this case occurs when 591 Col-PEG-AuNPs are bound to a single *A. baumannii* ATCC 19606 cell (~7.1 min). The association rate of Col-PEG-AuNPs with ATCC 17978 is not significantly different than that of Col-PEG-AuNPs with ATCC 19606. This indicates that the Col-PEG-AuNPs associate similarly with both *A. baumannii* ATCC 17978 and *A. baumannii* ATCC 19606.

The rate of Col-PEG-AuNP association with colistin resistant *A. baumannii* (ATCC 19606C) was also evaluated. In this case, A_{Max} is approximately equal to 584 Col-PEG-AuNPs per *A. baumannii* ATCC 19606C (Fig 2.11c). The time constant, τ, is equivalent to approximately 10.7 minutes. Col-PEG-AuNP binding to *A. baumannii* strain ATCC 19606C can be represented as:

$$\mathrm{A} = 584 * (1 - e^{-t/10.7}) \tag{2.6}$$

Under these conditions, half-maximal binding occurs when 292 Col-PEG-AuNPs are bound to a single *A. baumannii* ATCC 19606C cell (~7.4 min). The A_{Max} value associated with Col-PEG-AuNP binding to colistin resistant *A. baumannii* (ATCC 19606C) is significantly less than the A_{Max} values seen in Equations (2.4) and (2.5). It is proposed that this is most likely due to changes in the outer membrane of colistin resistant *A. baumannii* (ATCC 19606C), which would affect the binding of colistin to the bacterial cell[59].

The kinetic analysis suggests that the binding rate, τ, of colistin-functionalized nanoparticles to colistin resistant *A. baumannii* (ATCC 19606C) is equal to that of colistin sensitive strains (ATCC 19606 and ATCC 17978). However, the maximum number of colistin binding events per *A. baumannii* cell is significantly reduced by colistin resistance, as measured by A_{Max}. These results are consistent with functional LPS at a reduced surface concentration on colistin resistant *A. baumannii*.

The PEG-AuNP control samples, in the absence of colistin, did not exhibit time dependent binding behavior with any of the three strains of *A. baumannii* that were evaluated (Fig 2.11a, 2.11b, and 2.11c). This further confirmed that nanoparticle attachment to *A. baumannii* was dependent upon the presence of the colistin targeting ligand. Colistin is effective as a targeting ligand even in the case of colistin resistant *A. baumannii* (ATCC 19606C), as seen in Figure 2.11c.

A)

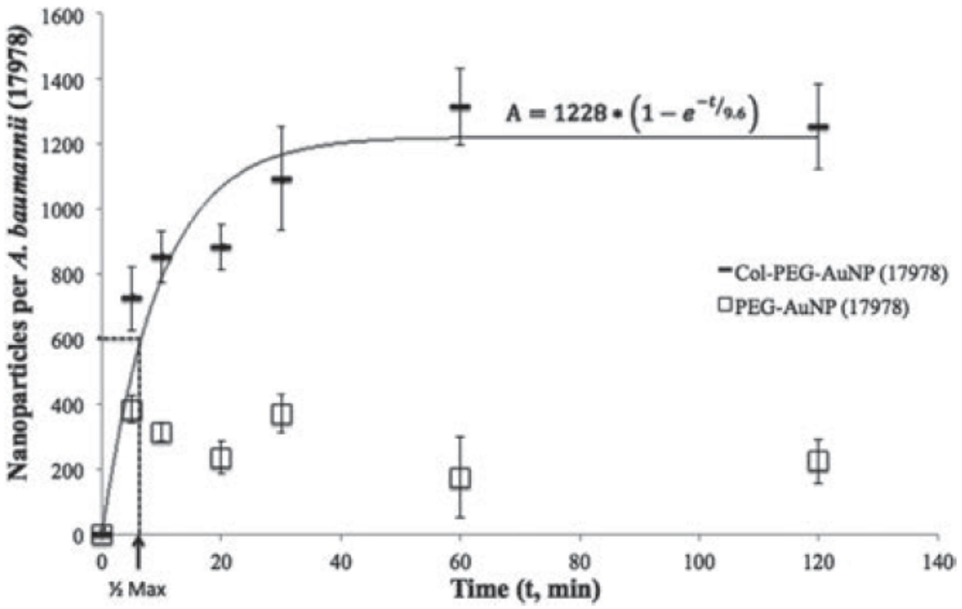

Nanoparticles per *A. baumannii* (17978)
1600
1400
1200
1000
800
600
400
200
0
A = 1228 • (1 − e^{−t/9.6})
Col-PEG-AuNP (17978)
PEG-AuNP (17978)
0
20
40
60
80
100
120
140
½ Max
Time (t, min)

B)

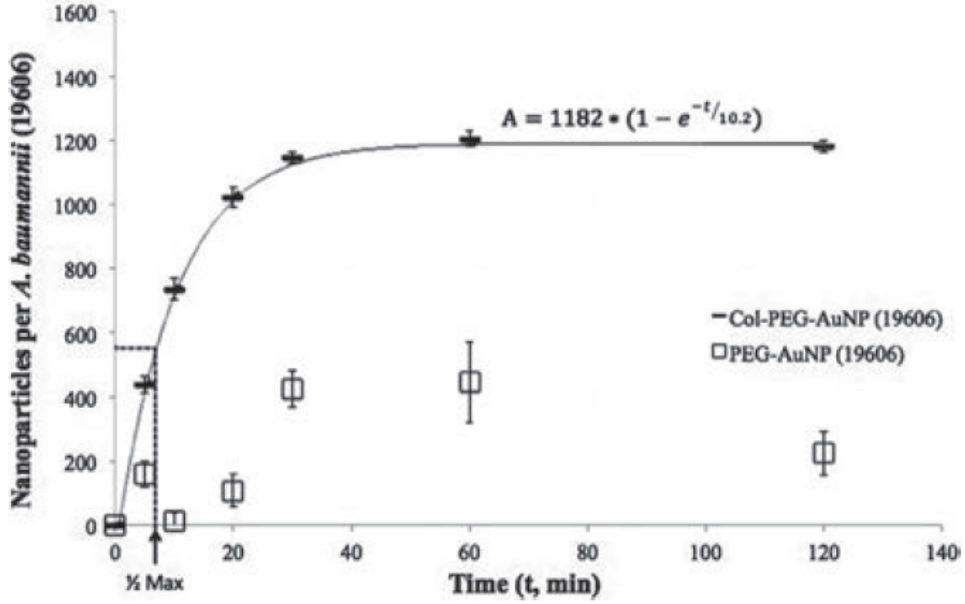

Nanoparticles per *A. baumannii* (19606)
1600
1400
1200
1000
800
600
400
200
0
A = 1182 • (1 − e^{−t/10.2})
Col-PEG-AuNP (19606)
PEG-AuNP (19606)
0
20
40
60
80
100
120
140
½ Max
Time (t, min)

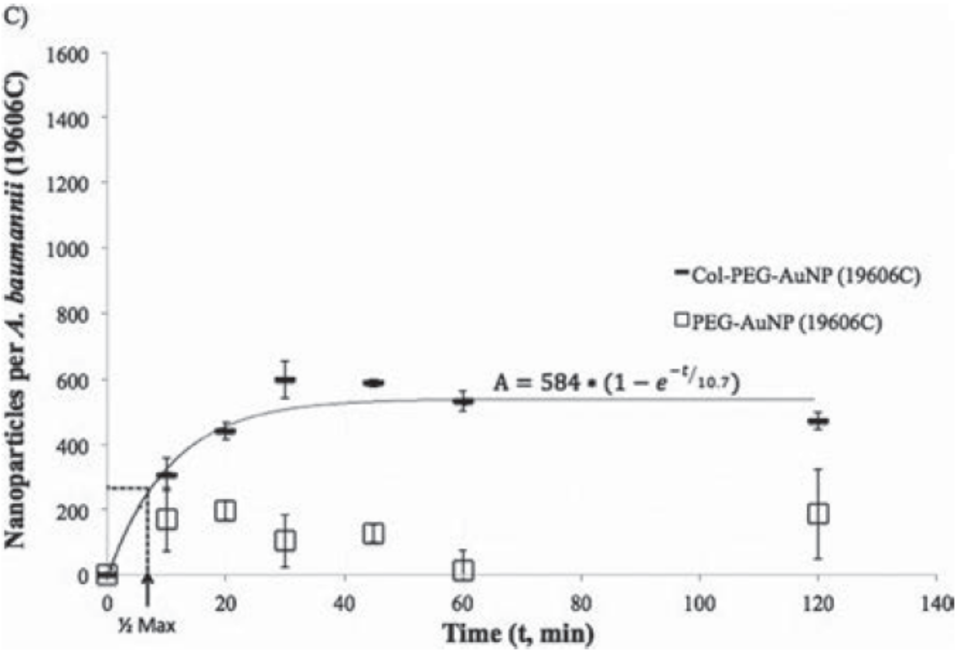

Figure 2.11. Col-PEG-AuNPs rapidly and specifically associated with *A. baumannii* (ATCC 17978, ATCC 19606, ATCC 19606C), whereas PEG-AuNPs did not specifically bind the bacteria. **a**, Col-PEG-AuNPs rapidly and specifically associated with *A. baumannii* (ATCC 17978), reaching 50% maximum saturation within 6.7 min, whereas PEG-AuNPs did not specifically bind the bacteria. **b**, Col-PEG-AuNPs rapidly and specifically associated with *A. baumannii* (ATCC 19606), reaching 50% maximum saturation within 7.1 min, whereas PEG-AuNPs did not specifically bind the bacteria. **c**, Col-PEG-AuNPs specifically associated with colistin-resistant *A. baumannii* (ATCC 19606C), reaching 50% maximum saturation within 7.4 min, whereas PEG-AuNPs did not specifically bind the bacteria. For all three *A. baumannii* strains evaluated, including colistin resistant (ATCC 19606C), interaction of Col-PEG-AuNPs with *A. baumannii* was significantly different than the interaction of PEG-AuNPs with *A. baumannii*. ANOVA and *post hoc* analysis prove that Col-PEG-AuNP binding to *A. baumannii* is significantly different than that of PEG-AuNPs at all time points.

Conclusions

This work, for the first time, presented a mathematical description of the binding kinetics between colistin-functionalized nanoparticles and three different *A. baumannii* strains, including a colistin resistant strain. The novel nanoparticle system with colistin as an *A. baumannii* targeter covalently conjugated to the distal end of PEG eliminated the possibility of colistin disassembly through electrostatic interactions. Additionally, the use of a ligand presumably reduced colistin steric hindrance and increased nanoparticle-bacteria association.

Colistin-functionalized nanoparticles specifically associated with *A. baumannii*, whereas PEG-AuNPs did not. The rapid rate of nanoparticle-bacteria association mediated through colistin enables the consideration of new approaches to bacterial detection and isolation. Colistin is projected to support extraction of particle-bound *A. baumannii* using methods similar to Singh et al. and Lee et al.[24,52]. Because colistin is FDA approved and readily available, this design may be further developed and translated for use in the clinical setting and for water purification purposes. Rapid, colistin mediated binding of nanoparticles to *A. baumannii* also potentially enables new advances in the detection and purification of Gram-negative bacteria from other environmental samples, such as food and soil.

Summary

A colistin functionalized nanoparticle that combines the properties necessary to target and bind to *Acinetobacter baumannii*, including drug-resistant variants, was designed, fabricated, and characterized. A comparable variant of the colistin functionalized nanoparticle, a PEGylated nanoparticle, was fabricated and characterized to substantiate the results and conclusions of this study. The colistin functionalized nanoparticle was carefully designed and tuned to promote rapid bacterial binding while reducing colistin steric hindrance through the use of a heterobifunctional linker. Utilizing colistin as a targeting motif is advantageous because it is a readily available and has been used in the clinical setting for decades. This design simplifies development and facilitates regulatory considerations relative to the use of genetically engineered or new biomacromolecular ligands. Results support the claims that: (1) colistin functionalized nanoparticles were fabricated and (2) colistin can be used as targeting motif to capture *A. baumannii*, including (3) drug-resistant variants. **This work successfully fulfills Specific Aim 1 of this dissertation**. Furthermore, this work was published in the *Journal of Biomedical Nanotechnology*, Volume 12, Issue 9 (Fig 2.12) [73].

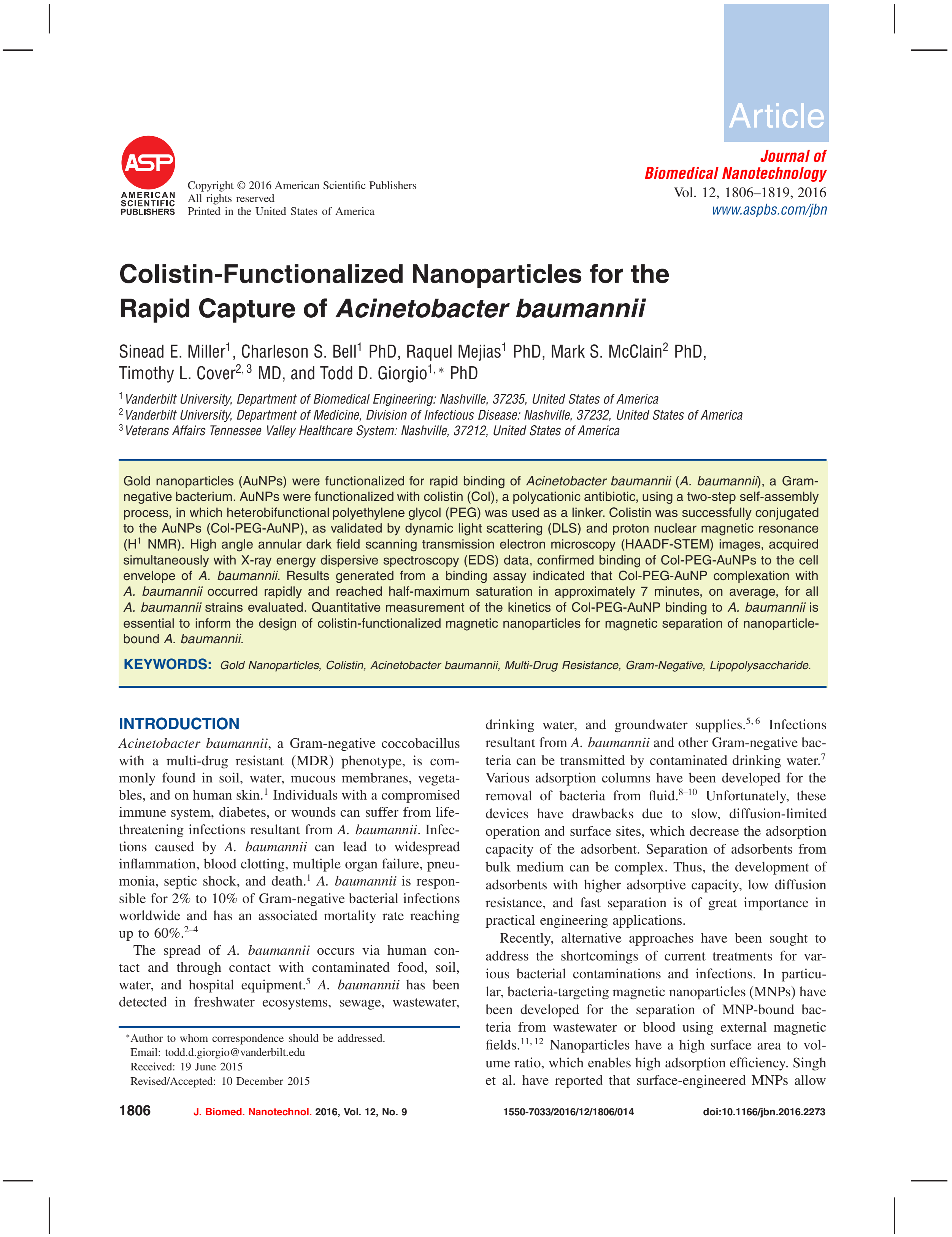

Article

Journal of
Biomedical Nanotechnology
Vol. 12, 1806–1819, 2016
www.aspbs.com/jbn

Colistin-Functionalized Nanoparticles for the Rapid Capture of *Acinetobacter baumannii*

Sinead E. Miller[1], Charleson S. Bell[1] PhD, Raquel Mejias[1] PhD, Mark S. McClain[2] PhD,
Timothy L. Cover[2,3] MD, and Todd D. Giorgio[1,*] PhD

[1] *Vanderbilt University, Department of Biomedical Engineering: Nashville, 37235, United States of America*
[2] *Vanderbilt University, Department of Medicine, Division of Infectious Disease: Nashville, 37232, United States of America*
[3] *Veterans Affairs Tennessee Valley Healthcare System: Nashville, 37212, United States of America*

Gold nanoparticles (AuNPs) were functionalized for rapid binding of *Acinetobacter baumannii* (*A. baumannii*), a Gram-negative bacterium. AuNPs were functionalized with colistin (Col), a polycationic antibiotic, using a two-step self-assembly process, in which heterobifunctional polyethylene glycol (PEG) was used as a linker. Colistin was successfully conjugated to the AuNPs (Col-PEG-AuNP), as validated by dynamic light scattering (DLS) and proton nuclear magnetic resonance (H^1 NMR). High angle annular dark field scanning transmission electron microscopy (HAADF-STEM) images, acquired simultaneously with X-ray energy dispersive spectroscopy (EDS) data, confirmed binding of Col-PEG-AuNPs to the cell envelope of *A. baumannii*. Results generated from a binding assay indicated that Col-PEG-AuNP complexation with *A. baumannii* occurred rapidly and reached half-maximum saturation in approximately 7 minutes, on average, for all *A. baumannii* strains evaluated. Quantitative measurement of the kinetics of Col-PEG-AuNP binding to *A. baumannii* is essential to inform the design of colistin-functionalized magnetic nanoparticles for magnetic separation of nanoparticle-bound *A. baumannii*.

KEYWORDS: *Gold Nanoparticles, Colistin, Acinetobacter baumannii, Multi-Drug Resistance, Gram-Negative, Lipopolysaccharide.*

INTRODUCTION

Acinetobacter baumannii, a Gram-negative coccobacillus with a multi-drug resistant (MDR) phenotype, is commonly found in soil, water, mucous membranes, vegetables, and on human skin.[1] Individuals with a compromised immune system, diabetes, or wounds can suffer from life-threatening infections resultant from *A. baumannii*. Infections caused by *A. baumannii* can lead to widespread inflammation, blood clotting, multiple organ failure, pneumonia, septic shock, and death.[1] *A. baumannii* is responsible for 2% to 10% of Gram-negative bacterial infections worldwide and has an associated mortality rate reaching up to 60%.[2–4]

The spread of *A. baumannii* occurs via human contact and through contact with contaminated food, soil, water, and hospital equipment.[5] *A. baumannii* has been detected in freshwater ecosystems, sewage, wastewater, drinking water, and groundwater supplies.[5,6] Infections resultant from *A. baumannii* and other Gram-negative bacteria can be transmitted by contaminated drinking water.[7] Various adsorption columns have been developed for the removal of bacteria from fluid.[8–10] Unfortunately, these devices have drawbacks due to slow, diffusion-limited operation and surface sites, which decrease the adsorption capacity of the adsorbent. Separation of adsorbents from bulk medium can be complex. Thus, the development of adsorbents with higher adsorptive capacity, low diffusion resistance, and fast separation is of great importance in practical engineering applications.

Recently, alternative approaches have been sought to address the shortcomings of current treatments for various bacterial contaminations and infections. In particular, bacteria-targeting magnetic nanoparticles (MNPs) have been developed for the separation of MNP-bound bacteria from wastewater or blood using external magnetic fields.[11,12] Nanoparticles have a high surface area to volume ratio, which enables high adsorption efficiency. Singh et al. have reported that surface-engineered MNPs allow

---

[*] Author to whom correspondence should be addressed.
Email: todd.d.giorgio@vanderbilt.edu

Received: 19 June 2015
Revised/Accepted: 10 December 2015

1806 J. Biomed. Nanotechnol. 2016, Vol. 12, No. 9 1550-7033/2016/12/1806/014 doi:10.1166/jbn.2016.2273

Figure 2.12. Publication in *Journal of Biomedical Nanotechnology*, Volume 12, Issue 9 [73].

CHAPTER III

DYNAMIC COMPUTATIONAL MODEL TO INFORM BACTERIAL SEPARATION REQUIREMENTS

The rise of multi-drug resistance has decreased the effectiveness of antibiotics, which has led to increased mortality rates associated with symptomatic bacteremia, or bacterial sepsis. To combat decreasing antibiotic effectiveness, extracorporeal bacterial separation approaches have been proposed to capture and separate bacteria from blood. However, sepsis is dynamic and involves host-pathogen interactions across various anatomical sites. I developed a mathematical model that quantitatively describes the kinetics of pathogenesis and progression of sepsis under various conditions, including bacterial separation therapy, to better understand disease mechanisms and quantitatively assess the biological impact of bacterial separation therapy. Model validity was tested against experimental data from published studies. This is the first multi-compartment model of sepsis in mammals that includes extracorporeal bacterial separation and antibiotic treatment, separately and in combination.

The addition of an extracorporeal bacterial separation circuit reduced the predicted time of total bacteria clearance from the blood of an immunocompromised rodent by 49%, compared to antibiotic treatment alone. Implementation of bacterial separation therapy resulted in predicted multi-drug resistant bacterial clearance from the blood of a human in 97% less time than antibiotic treatment alone. The model also proposes a quantitative correlation between time-dependent bacterial load among tissues and bacteremia severity, analogous to the well-known ‘area under the curve’ for characterization of drug efficacy. The engineering-based mathematical model developed may be useful for informing the design of extracorporeal bacterial separation devices. This work enables the quantitative identification of the characteristics required of an extracorporeal bacteria separation device to provide biological benefit. These devices will potentially decrease the bacterial load in blood. Additionally, the devices may achieve bacterial separation rates that allow consequent acceleration of bacterial clearance in other tissues, inhibiting the progression of sepsis, including multi-drug resistant variations. Results from this chapter will fulfill Specific Aim 2 of my dissertation.

Introduction

Symptomatic bacteremia is a common cause of severe sepsis[74]. In the United States, Gram-negative bacteria cause approximately 70% of hospital acquired infections in intensive care units[75], while up to half of all bloodstream infections are caused by Gram-negative bacilli[76]. Infections caused by Gram-negative bacteria are of particular concern because these organisms are highly efficient at acquiring and up-regulating various mechanisms that promote multi-drug resistance (MDR)[77]. Global concern revolves around the ever-increasing number of infections caused by MDR Gram-negative bacteria, in particular *Acinetobacter baumannii* and *Klebsiella pneumoniae*[59].

A. baumannii and *K. pneumoniae* are both Gram-negative bacilli with MDR phenotypes. These bacteria are commonly found in the hospital setting and reside in internal parts of the human body[44,78]. One of the strongest risk factors for developing a Gram-negative bloodstream infection is a compromised immune system. More specifically, those suffering from neutropenia, or lack of neutrophils in the blood, run a significantly higher risk for developing a bloodstream infection than healthy individuals[79,80]. *A. baumannii* and *K. pneumoniae* infections can lead to multiple consequences, such as widespread inflammation, blood clotting, multiple organ failure, pneumonia, septic shock, and death. The crude mortality rate associated with an *A. baumannii* or *K. pneumoniae* bloodstream infection in an immunocompromised patient can exceed 70%[79,81,82].

Treatment of a bloodstream infection requires eradication of bacteria from the blood, but also from other tissues, including the source of infection. The clearance of bacteria by the host immune response is similar to the pharmacokinetic clearance of drugs. Therefore, the clearance of bacteria from the host may be interpreted using a multi-compartment model with each compartment representing a tissue into which bacteria may enter and exit, replicate, or be eliminated by treatment. Bacteria can be transferred among tissues and eventually be eliminated through an immune response, therapeutic treatment, or a combination of both. Unlike drugs, bacteria proliferate prior to host recognition, and bacteria continue to proliferate in the case of an unsuccessful host defense.

Bacterial clearance from the bloodstream in a physiologically based pharmacokinetic (PBPK) model was first described in 1983 by Cheewatrakoolpong et al.[83]. The group analyzed the kinetics of bacterial clearance from the blood and mesenteric lymph nodes of mice using a two-compartment computational model. More recently, Kang et al. developed a mathematical model that predicts bacterial clearance solely from the bloodstream[26]. In the Kang et al. model, the group incorporated the effects of an extracorporeal bacterial separation device that continuously removes bacteria from flowing blood using a magnetic nanoparticle-based separation technique. The mathematical model successfully predicted the optimal magnetic nanoparticle sizes required for removal of bacteria from whole blood. This model enabled predictions of particle–pathogen collision and magnetophoresis rates, which allowed for determination of how these factors influence magnetic pathogen separation from blood under flow using a microfluidic magnetic separation device. The biological impact of bacterial separation in the host, however, was not incorporated into this model.

The work by Kang et al. can be expanded into a five-compartment model that accounts for physical and immunological interactions, bacterial net growth, transport among tissues (lungs, spleen, liver, blood), antibiotic treatment, and extracorporeal removal of bacteria from the blood. This type of expanded, dynamic model can be used to characterize time-dependent, tissue-specific bacterial load in symptomatic bacteremia. Also, such a model could be used to characterize the biological impact of bacterial separation from the blood, and, potentially, predict the utility as a therapeutic treatment option in conjunction with antibiotic treatment. Consequently, we developed a pharmacokinetic model of *A. baumannii* and *K. pneumoniae* sepsis in order to provide a quantitative and flexible framework useful for both experimental and analytical work in this area.

A five-compartment dynamic model, consisting of five first-order homogenous ordinary differential equations, was developed to study the biodistribution of *A. baumannii* and *K. pneumoniae* during bacterial sepsis in mammals. This pharmacokinetic model was used to assess the combination of broad-spectrum colistin antibiotic treatment and extracorporeal bacteria separation from the blood on the overall time-dependent bacterial burden in infected living systems. Colistin, a naturally occurring cationic decapeptide isolated from *Paenibacillus polymyxa* var. *colistinus*[53], is a potent broad-spectrum antimicrobial. This antibiotic is commonly used for the treatment of challenging Gram-negative pathogens[84], including *A. baumannii*.

The time course of a bacterial infection within important tissues of immunologically normal rodents was described using the mathematical model. The same measures were then used to examine the impact of suppressed immunity. The efficacy of antibiotic administration in immunosuppressed rodents exposed to a bacterial challenge was also analyzed. Finally, the potential benefit of extracorporeal bacterial isolation and removal from blood, in terms of bacterial load by compartment, was assessed in both rodent and human mathematical models.

Analyzing results from this model of multi-organ infection with a PBPK mathematical approach provides an opportunity to evaluate the efficacy of extracorporeal bacterial separation from the bloodstream in combination with various antibiotic treatment regimens. For the first time, a modeling approach based on experimentally obtained data allows quantitative exploration of the impact of extracorporeal bacterial separation in combination with antibiotic treatment.

Materials and Methods

Kinetic Model and Parameter Values

A five-compartment kinetic model was developed to explore the pathogenesis kinetics and treatment of sepsis (Fig 3.1). It was assumed that infection occurred via intratracheal instillation of a 10^7 CFU/mL Gram-negative bacteria (*Acinetobacter baumannii* or *Klebsiella pneumoniae*) bolus into the lung compartment. This is a common bacterial concentration used to establish and study rodent sepsis models[85]. Also, the most common site of infection leading to sepsis in humans is the lungs[86,87]. Bacterial exchange among all five compartments, which included the lungs, spleen, liver, blood, and bacterial separation device, was programmed as specified by the model construction and parameters extracted from experimental studies of sepsis. The lungs, liver, spleen, and blood were included because all have experimentally demonstrated the most significant and rapid uptake of blood-borne bacteria[88]. Kinetics were assumed to be first order. Bacteria proliferated (p (h^{-1})) within the lungs, spleen, liver, and blood, and were cleared (c) by immunological interactions at rates (h^{-1}) specific to each compartment. No experimental evidence was available to distinguish p from c *in vivo*, therefore, the two terms were considered as a single net bacterial growth rate (G_x (h^{-1})). Bacterial transport between compartments was represented as a function of the blood flow rate, Q, the compartment volume, V, and a partitioning coefficient, x[88]. The partition coefficient represented the ratio of bacteria concentration between compartments and was proportional to the concentration of bacteria in the donor compartment[88]. Bacterial separation efficiency, $f(r_f)$, represented the percent of target bacterial cells separated by the bacterial separation compartment (CFU mL^{-1}) per total number of target bacterial cells (CFU mL^{-1}).

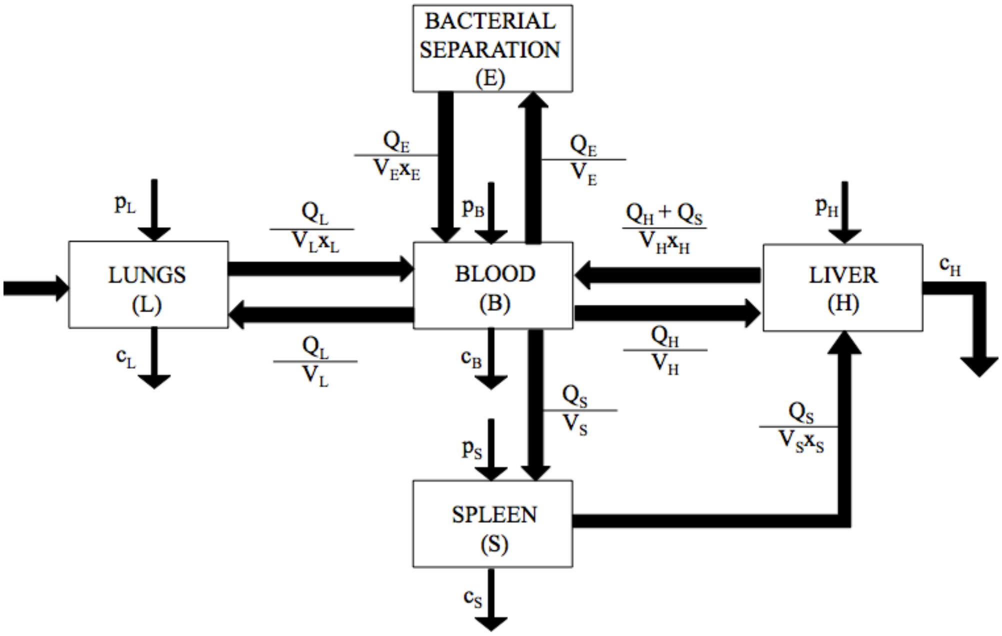

Figure 3.1. The five-compartment kinetic model describing bacterial pathogenesis. Intratracheal instillation of a Gram-negative bacteria bolus initially occurred in the lung compartment, with initial concentration L_0 (CFU mL^{-1}). Bacterial proliferation rates (p, h^{-1}), clearance rates (c, h^{-1}), and transport rates between compartments were included in the model schematic. The rate of bacterial transport between compartments was represented as a function of blood flow rate per compartment volume (Q/V, mL h^{-1}), modified by an experimentally determined partitioning coefficient (x, dimensionless).

Five first-order homogenous ordinary differential equations (ODEs) were used as a model representation of the physiological features of the system. The system of equations was based on previously published pharmacokinetic models[88,89]. Each autonomous ODE represented the instantaneous rate of change of bacteria concentration in the respective compartment,

$$\frac{dL}{dt} = \big((G_L) * L\big) + \left(\frac{Q_L}{V_L} * B\right) - \left(\frac{Q_L}{V_L x_L} * L\right) \tag{3.1}$$

$$\frac{dS}{dt} = \big((G_s) * S\big) + \left(\frac{Q_s}{V_s} * B\right) - \left(\frac{Q_s}{V_s x_s} * S\right) \tag{3.2}$$

$$\frac{dH}{dt} = \big((G_H) * H\big) + \left(\frac{Q_H}{V_H} * B\right) + \left(\frac{Q_s}{V_s x_s} * S\right) - \left(\frac{Q_H + Q_s}{V_H x_H} * H\right) \tag{3.3}$$

$$\frac{dE}{dt} = \left(\frac{Q_E}{V_E} * B * f(r_f)\right) - \left(\frac{Q_E}{V_E x_E} * E * \left(1 - f(r_f)\right)\right) \tag{3.4}$$

$$\begin{aligned}\frac{dB}{dt} = {} & \big((G_B) * B\big) + \left(\frac{Q_H + Q_s}{V_H x_H} * H\right) + \left(\frac{Q_L}{V_L x_L} * L\right) + \left(\frac{Q_E}{V_E x_E} * E * \left(1 - f(r_f)\right)\right) \\ & - \left[\left(\frac{Q_H}{V_H} + \frac{Q_s}{V_s} + \frac{Q_L}{V_L} + \left(\frac{Q_E}{V_E} * f(r_f)\right)\right) * B\right]\end{aligned} \tag{3.5}$$

where *L*, *S*, *H*, *E*, and *B* were the bacterial concentrations (CFU mL^{-1}), in the lungs, spleen, liver, extracorporeal bacterial separation device, and blood, respectively. The model was designed such that bacteria were transported from the spleen into the liver via hepatic portal circulation. Liver (H, hepatic) circulation was divided into splenic portal venous blood and the combination of hepatic arterial flow and its tributaries. Mouse and human organ mass values were based on published literature and were used to describe organ volumes, *V*[88]. Organ blood flow rates, *Q*, and blood:organ partition coefficients, *x*, were also gathered from previously published data[88]. Empirical values used to describe compartmental volumes, blood flow rates, and partition coefficients can be found in Table 3.1a and 3.1b and Table 3.2.

Compartment	**Blood Flow Rate, *Q* (mL min^{-1} g^{-1})**	**Volume, *V* (g or mL)**
Lungs (L)	6.84	2.10
Spleen (S)	1.20	0.15
Liver (H)	1.50	1.99
Extracorporeal Bacterial Separation Device (E)	Variable	0.032

Table 3.1a. Model parameters, rodent[88].

Compartment	**Blood Flow Rate, *Q* (mL min^{-1} g^{-1})**	**Volume, *V* (g or mL)**
Lungs (L)	1.14	1315
Spleen (S)	1.97	127
Liver (H)	0.97	830
Extracorporeal Bacterial Separation Device (E)	Variable	90

Table 3.1b. Model parameters, human[90–93].

Compartment	**Partition Coefficient, *x* (Immunocompromised)**	**Partition Coefficient, *x* (Non-Immunocompromised)**
Lungs (L)	3	93
Spleen (S)	28	59
Liver (H)	79	749
Extracorporeal Bacterial Separation Device (E)	1	1

Table 3.2. Partition coefficient model parameters[88].

The rodent model was based on 58.5 ml of blood per kg of bodyweight[94]. A mouse weighing 31 g would have a total blood volume of approximately 1.80 mL. Subsequent calculations were scaled to account for the 5000 mL average total blood volume of humans.

The net bacterial growth rates, G_x, in each compartment of non-immunocompromised subjects, along with immunocompromised neutropenic subjects, can be found in Table 3.3a and 3.3b. These values were derived from published literature in which the total bacterial burden was measured in each compartment of a rodent over a specific period of time. This data has not been reported for human subjects. Therefore, net bacterial growth rates in human compartments were based on rodent models.

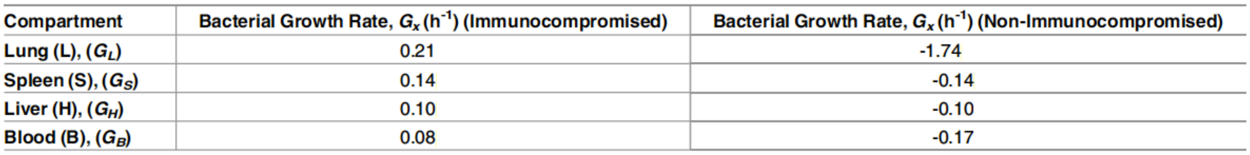

Compartment	Bacterial Growth Rate, G_x (h^{-1}) (Immunocompromised)	Bacterial Growth Rate, G_x (h^{-1}) (Non-Immunocompromised)
Lung (L), (G_L)	0.21	-1.74
Spleen (S), (G_S)	0.14	-0.14
Liver (H), (G_H)	0.10	-0.10
Blood (B), (G_B)	0.08	-0.17

Table 3.3a. Net bacterial growth rates, *A. baumannii*[88,95–98].

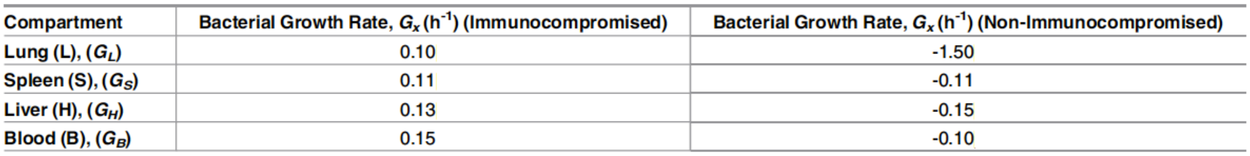

Compartment	Bacterial Growth Rate, G_x (h^{-1}) (Immunocompromised)	Bacterial Growth Rate, G_x (h^{-1}) (Non-Immunocompromised)
Lung (L), (G_L)	0.10	-1.50
Spleen (S), (G_S)	0.11	-0.11
Liver (H), (G_H)	0.13	-0.15
Blood (B), (G_B)	0.15	-0.10

Table 3.3b. Net bacterial growth rates, *K. pneumonia*[99–101].

Net bacterial growth rates corresponding to each compartment following colistin antibiotic treatment are displayed in Table 3.4a and 3.4b[102,103]. Experimental evidence was not available to distinguish *p* from *c in vivo*. However, it was possible to deduce single net bacterial growth rates (G_x (h^{-1})) by analyzing literature that reported the total bacterial burden in each compartment before and after colistin treatment.

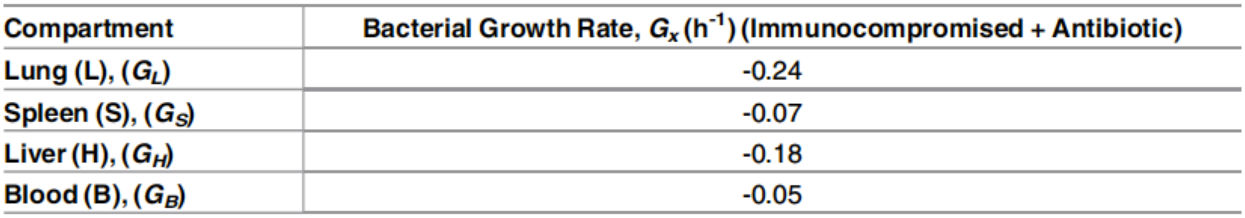

Compartment	Bacterial Growth Rate, G_x (h^{-1}) (Immunocompromised + Antibiotic)
Lung (L), (G_L)	-0.24
Spleen (S), (G_S)	-0.07
Liver (H), (G_H)	-0.18
Blood (B), (G_B)	-0.05

Table 3.4a. Net bacterial growth rates, *A. baumannii* with colistin[103].

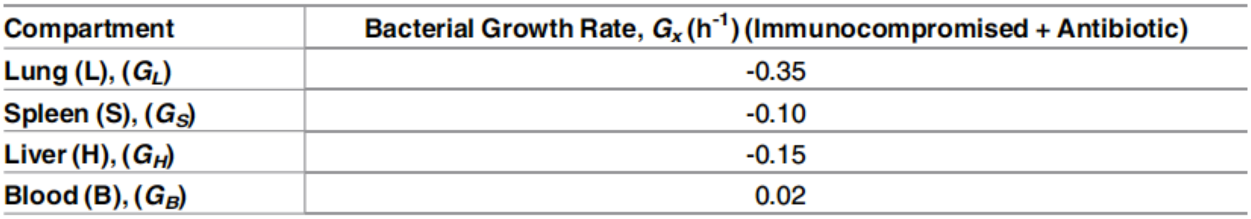

Compartment	Bacterial Growth Rate, G_x (h^{-1}) (Immunocompromised + Antibiotic)
Lung (L), (G_L)	-0.35
Spleen (S), (G_S)	-0.10
Liver (H), (G_H)	-0.15
Blood (B), (G_B)	0.02

Table 3.4b. Net bacterial growth rates, *K. pneumoniae* with colistin[102,103].

Magnetic Separation Component Design

The bacterial separation (E) component of the model embodied a fluidic device in which continuous magnetic separation of Gram-negative bacteria from non-Newtonian particulate blood flow occurred. The magnetic separation device consisted of two steps, together comprising the total magnetic separation efficiency, $f(r_f)$: 1) Gram-negative bacteria–targeted magnetic nanoparticles bound to the bacterial cells and 2) the magnetic separation of nanoparticle-bacteria complexes from the blood. Total magnetic separation efficiency, $f(r_f)$, of bacteria from the blood was dependent upon magnetic nanoparticle size, blood viscosity, and magnetic forces. The modeling parameters and equations used to calculate the value of $f(r_f)$ were based on previous studies[26,104].

Briefly, the value of $f(r_f)$ was calculated for various nanoparticle sizes by determining the binding kinetics between the magnetic nanoparticles and bacteria. Assuming that all bacteria bound to magnetic nanoparticles were removed by the magnetic fluidic device, the binding efficiency, $x(r_f)$, was represented by

$$x(r_f) = \left(1 - e^{(-c_e(k_d + k_{shear}) * b * t)}\right) * 100 \tag{3.6}$$

where b was the concentration of magnetic nanoparticles, k_d the diffusion collision rate constant, k_{shear} the shear collision rate constant, and c_e ($3.7 * 10^{-4}$ <dimensionless>) an empirical constant representing the binding efficiency of bacteria to the magnetic nanoparticles in whole blood[26].

Then, the effects of the magnetophoretic separation of the magnetic nanoparticle-bound bacteria from the blood under continuous flow were determined. The magnetic forces acting on the magnetic nanoparticle-bound bacteria directly impacted the magnetic separation efficiency. Therefore, the magnetic separation efficiency was estimated by calculating the magnetic force induced by our defined theoretical parameters,

$$F_{mag} = N * \frac{4\pi r_f^3}{3} * \frac{\Delta\chi}{2\mu_o} * B^2 \tag{3.7}$$

where r_f was the radius of a magnetic nanoparticle, μ_o was the magnetic permeability of vacuum

($4\pi * 10^{-7} < T\ m\ A^{-1} >$), B^2 was the magnetic field intensity ($B^2 = 40 < T^2\ m^{-1} >$), N was the number of magnetic nanoparticles bound to the bacteria cell, and Δχ (<dimensionless>) was the volumetric susceptibility of the magnetic nanoparticles[104]. The following conditions were used:

$$\Delta\chi = \frac{4 * 3.5 * \pi * r_f^3}{3} \tag{3.8}$$

$$N = 4 * \rho * \left(\frac{r_c}{r_f}\right)^2 \tag{3.9}$$

where r_c was the effective spherical radius of a pathogen (0.5 µm, *A. baumannii*[73]; 0.65 µm, *K. pneumoniae*[105]) and it was assumed, based on previous literature, that half of the cell surface was covered by magnetic particles (ρ = 0.5 <dimensionless>)[26,104].

Assuming a quasi-static motion,

$$F_{mag} = F_{drag} = 6\pi r_n \eta v_{mag} \tag{3.10}$$

where r_n was the effective hydraulic radius of the bacteria–nanoparticle complex and η was the blood viscosity ($4 * 10^{-3}$ <N s m^{-2}>)[26]. The variable r_n can be represented as

$$r_n = \sqrt[3]{r_c^3 + N * r_f^3} \tag{3.11}$$

For small particles, $F_{mag} = F_{drag}$ and, therefore, the magnetophoretic velocity (v_{mag}) of the magnetic nanoparticle-bacteria complex can be defined as

$$v_{mag} = \frac{r_n^2 N \Delta\chi B^2}{9\eta\mu_o} \tag{3.12}$$

Blood flowing through the magnetic extraction fluidic component at a flow rate of Q (L h^{-1}) resulted in an average linear velocity (v_1) of bacteria labeled with magnetic nanoparticles of

$$v_1 = \frac{Q}{a} \tag{3.13}$$

where a was the cross-sectional area of the device channel (0.002 m x 0.0006 m; width x height)[26]. The characteristic residence time, t_{res}, of the nanoparticle-bound bacteria in the magnetic fluidic device channel was approximated by

$$t_{res} = \frac{L_L}{v_1} \tag{3.14}$$

where L_L was the hypothetical length of the channel (L_L = 0.027 m)[26]. The magnetophoretic transverse time (t_{mag}), the time it takes the nanoparticle-bound bacteria to be extracted from the blood by the magnets of the fluidic device, was described by

$$t_{mag} = \frac{L_h}{v_{mag}} \tag{3.15}$$

where L_h was the height of the magnetic fluidic device channel (0.0006 m)[26].

The magnetic separation efficiency, $m(r_f)$, was then estimated by comparing the characteristic residence time (t_{res}) to the time required for the nanoparticle-bound bacteria to be extracted from the blood by the magnets of the fluidic device (t_{mag})[26].

$$m(r_f) = 100 * \frac{t_{res}}{t_{mag}}, t_{res} < t_{mag} \tag{3.16}$$

$$m(r_f) = 100, t_{res} \geq t_{mag} \tag{3.17}$$

Finally, the total magnetic separation efficiency, $f(r_f)$, for the two-step process was calculated using

$$f(r_f) = x(r_f) * m(r_f) \tag{3.18}$$

Maximum magnetic separation of bacteria from blood was predicted to occur when using magnetic nanoparticles with 25 nm radii. As the magnetic nanoparticle radius increased, the extraction efficiency decreased (Fig 3.2). Experimental and theoretical results from Kang et al. were used to validate this trend[26].

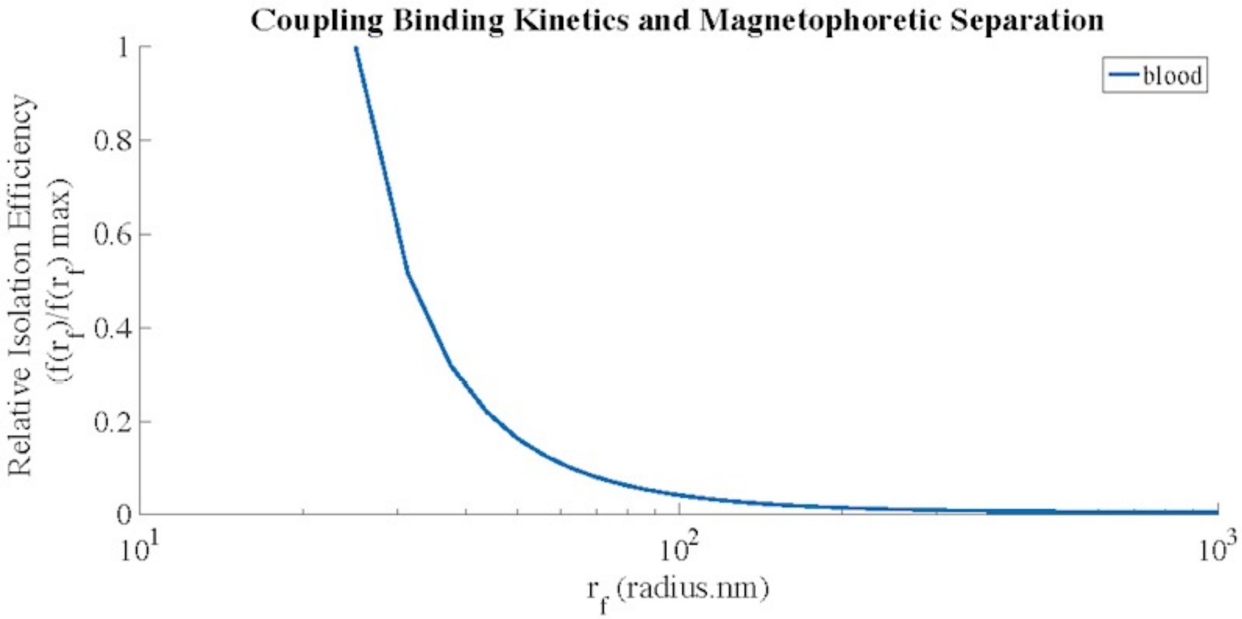

Figure 3.2. Magnetic separation efficiency, *f(r$_f$)*, of Gram-negative bacteria incubated with bacteria-targeting magnetic nanoparticles in whole blood. In the model predictions, the maximum magnetic separation efficiency occurred using magnetic nanoparticles with a radius of 25nm. The theoretical model prediction was verified by comparison to results published by Kang et al.[26].

Model Analysis

All analysis was written in Matlab R2015b (The Mathworks, Inc, Natick, Mass). The model equations were solved using the appropriate ODE solver in Matlab. The parameters values were verified by fitting the solution of the differential equations to experimental data found in literature.

Results and Discussion

Time Course of Bacterial Infection in Immunonormal Rodents

Non-immunocompromised rodents challenged intratracheally with a prepared inoculum of either *A. baumannii* 10^7 CFU/mL or *K. pneumoniae* 10^7 CFU/mL[85,106] were modeled. The overall bacterial burden for both Gram-negative species decreased over time in all compartments, although at different rates (Fig 3.3a and 3.3b). The blood compartment of the non-immunocompromised rodent mathematical model required the least amount of time to clear bacteria to a negligible amount ($\leq$ 1 CFU/mL), followed by the spleen, lungs, and liver. The bacterial clearance trends shown in Figure 3.3a and 3.3b were compared to experimental studies, in which total bacterial burden was reported for the liver, spleen, lungs, and blood of non-immunocompromised rodents following intratracheal bacterial challenge[88,95,96,107–109]. Within 24 hours of intratracheal bacterial challenge, the total bacterial uptake by the liver was the largest, and was followed by the spleen, lungs, and blood[107]. The results of our model were in agreement with experimental results previously described[88,95,96,107–109]. Bruhn et al. experimentally demonstrated that an *A. baumannii* bacterial load of 10^4 CFU/mL within the blood compartment of a normal rodent model was reduced to negligible bacterial densities at a rate of -0.06 $\log_{10}$ CFU/mL/h[97]. This *A. baumannii* clearance rate, characteristic of the non-immunocompromised rodent blood compartment, was in agreement with in our model predictions (Fig 3.3a). The blood compartment bacterial load dropped to half maximal concentration within approximately 40 hours of the onset bacterial challenge. This rate of bacterial clearance within the blood compartment was equivalent to -0.06 $\log_{10}$ CFU/mL/h. Also, Guo et al. have reported that normal rodents infected intratracheally with an *A. baumannii* bolus clear the infection from the lungs at a rate of –0.1 $\log_{10}$ CFU/mL/h[95]. The average *A. baumannii* clearance rate within the lung compartment of the dynamic model was also -0.1 $\log_{10}$ CFU/mL/h (Fig 3.3a), corresponding to published experimental data. Furthermore, the *A. baumannii* bacterial burden within the liver of a normal rodent decreased at a rate of -0.06 $\log_{10}$ CFU/mL/h[96], which was the same liver clearance rate produced by the mathematical modeling results.

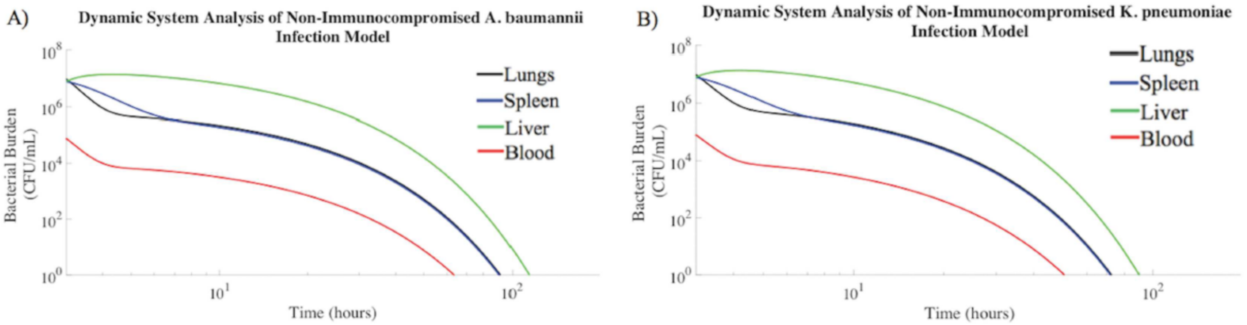

Figure 3.3. Bacterial burden decreased over time in tissue compartments of healthy rodents. Immunonormal rodents intratracheally inoculated with (**a**) *A. baumannii* (10^7 CFU/mL) or (**b**) *K. pneumoniae* (10^7 CFU/mL) were modeled. The median numbers of bacteria in each compartment observed experimentally were used as the initial conditions for these simulations[96–100], and trajectories were generated using the parameter estimates described in the Materials and Methods.

The mathematical model predictions were in quantitative agreement with experimental studies conducted by other laboratories. The model includes numerous physiological and microbiological parameters, which were chosen from first principles, not mathematical estimations. The agreement of model predictions with experimental data supports the validity of the model structure as representative of bacterial sepsis. The kinetic profiles of *A. baumannii* and *K. pneumoniae* concentration by tissue were similar for each set of assumptions evaluated in this work. Therefore, the remaining analysis of pathogenesis kinetics is described only for *A. baumannii*. The similar *K. pneumoniae* data is available in Appendix A.

Figure 3.3 suggests that an immunonormal rodent suppresses bacterial growth, with bacterial clearance from each compartment following a pattern of exponential decay. Model initial conditions were 3 hours post-inoculation, focusing the modeling effort on the slower processes of bacterial removal rather than the rapid distribution of bacteria[110]. Bacteria rapidly spread from the lungs to the bloodstream, which resulted in bacterial transport to other organs. The hematogenous spread of bacteria to other organ sites initially caused a rapid decrease in the bacterial burden of the blood compartment, but spread of infection increased the time required to suppress the infection.

Time Course of Bacterial Infection in Immunocompromised Rodents

A. baumannii and *K. pneumoniae* Gram-negative bacteria frequently cause sepsis in immunocompromised, neutropenic, elderly, and chronically ill individuals[111]. To better evaluate such cases, we modeled the onset of sepsis in neutropenic, immunocompromised rodents. Without treatment, the overall bacterial burden increased in neutropenic rodents until reaching a bacterial load associated with death[112,113]. This experimental condition was modeled in Figure 3.4. The fitted model agreed with published experimental data regarding bacterial burden over time in an untreated, immunocompromised rodent model[95]. Previously published experimental data demonstrated that a pulmonary *A. baumannii* bacterial burden within an immunocompromised rodent increased at a rate of +0.04 $\log_{10}$ CFU/mL/h[95,110], which was consistent with the mathematical modeling results (Fig 3.4). Modeling results also suggest that the *A. baumannii* bacterial burden associated with the blood compartment increased at a rate of +0.05 $\log_{10}$ CFU/mL/h, which was consistent with the experimental data published by Bruhn et al[97]. Approximately 100 hours following intratracheal exposure to 10^7 CFU/mL *A. baumannii*, neutropenic rodents succumb to the bacterial challenge[103,114]. This was consistent with the lethal bacterial concentration of 10^{10} CFU/mL at 96 hours predicted by mathematical modeling[103,113–115].

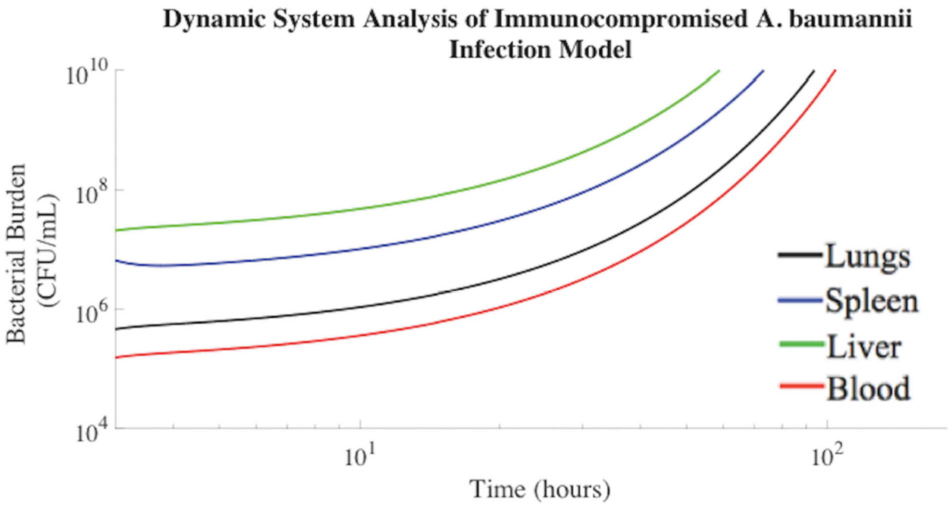

Figure 3.4. Bacterial burden increased over time in neutropenic rodents until reaching a lethal *A. baumannii* concentration. The median numbers of bacteria in each compartment observed experimentally in previous literature were used as the initial conditions for these simulations[98,101], and trajectories were generated using the parameter estimates shown in Materials and Methods.

The bacterial burden increases within the lungs, blood, and spleen compartments of Figure 3.4 are consistent with changes in bacterial transport out of the bloodstream, not simply suppressed bacteria clearance. Predictions obtained for the untreated, immunocompromised rodent model generated bacterial concentrations known to be lethal. Blood flow through the bacterial separation device compartment was set to zero in this scenario. All modeling parameters acquired and implemented were gathered directly from published experimental results and can be found in the Materials and Methods. Solutions from this multi-compartmental model were obtained in the absence of fitting parameters and mimicked experimental data, supporting the validity of the model.

Efficacy of Antibiotic Administration in Infected, Immunosuppressed Rodents

The most common treatment for sepsis is empiric, broad-spectrum antibiotic therapy. Therefore, colistin methanesulfonate antibiotic administration was incorporated into our mathematical model following the presentation of sepsis-like symptoms, which was presumed to occur when the bacterial concentration in the lungs reached 10^7 CFU/mL[110] and bacteria were completely distributed throughout all compartments. Bacteria rapidly distribute throughout the blood, liver, lungs, and spleen following exposure[88].

Following simultaneous intratracheal infusion of 10^7 CFU/mL *A. baumannii* and 3 mg/kg colistin methanosulfate, *A. baumannii* was cleared from the blood of the neutropenic rodent mathematical model within 55 hours (Fig 3.5). The rate constants pertaining to bacterial clearance following colistin methanosulfate administration were based on experimental data gathered experimentally by Pantopoulou et al. and Montero et al[103,116], as described in the Materials and Methods. The mathematical modeling (Fig 3.5) agreed with experimental data regarding the effects of colistin methanosulfate administration (3 mg/kg) on an *A. baumannii* bacterial burden in neutropenic rodent models, clearing the bacterial infection from the blood at a rate of -0.09 $\log_{10}$ CFU/mL/h[103,116].

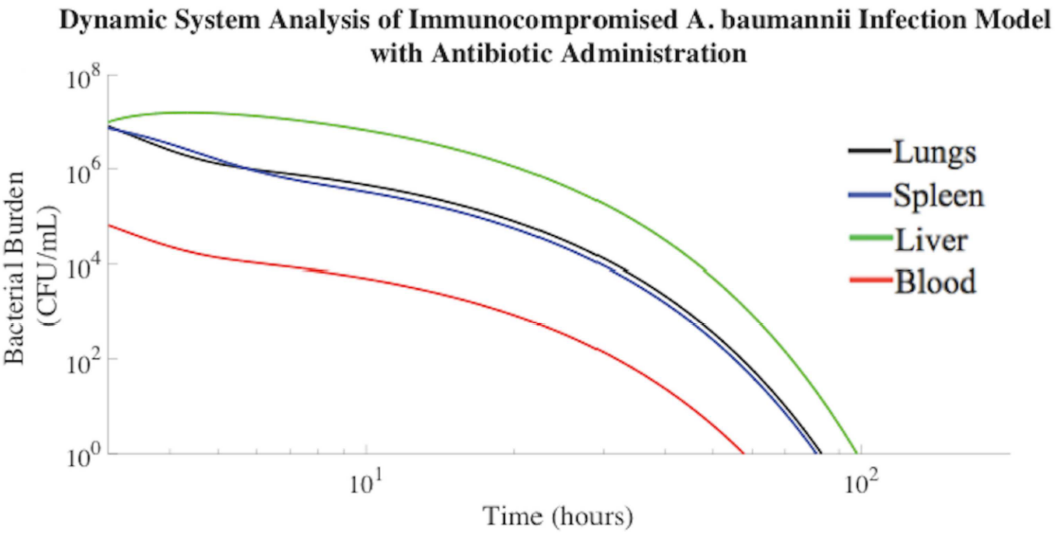

Figure 3.5. *A. baumannii* burden decreased post inoculation in immunocompromised rodents treated with colistin methanosulfate (3 mg/kg). The associated parameters are shown in Materials and Methods.

The area under the curve (AUC) was computed for each compartment displayed in Figure 3.5. The AUC reflects the total, time-dependent bacterial load experienced by each compartment of our model. Of note, the rodent mathematical model suggests that the liver consistently experienced the highest total bacterial burden, approximately an order of magnitude greater than the lungs, as indicated in Table 3.5. This result is consistent with the severe side effects observed during antibiotic treatment for sepsis, especially in immunocompromised and chemotherapy patients.

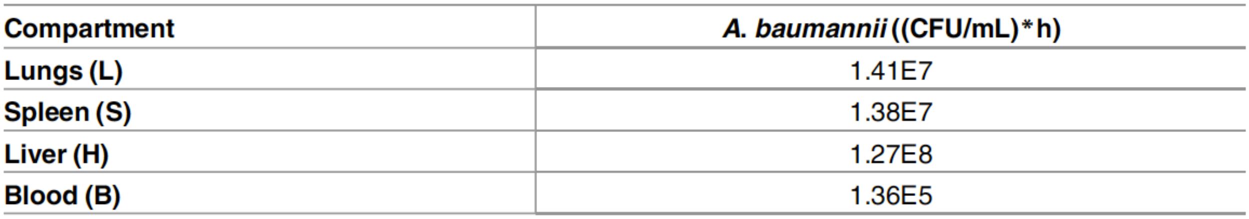

Compartment	*A. baumannii* ((CFU/mL)*h)
Lungs (L)	1.41E7
Spleen (S)	1.38E7
Liver (H)	1.27E8
Blood (B)	1.36E5

Table 3.5. *A. baumannii* burden experienced by immunocompromised rodent model administered colistin antibiotic.

Extracorporeal Bacterial Separation from Blood

Kang et al. have described the development of an extracorporeal bacterial separation device that can remove bacteria from blood[25]. The Kang et al. device employs magnetic nanoparticles to magnetically remove pathogens, including multi-drug resistant bacteria, from flowing blood in a microfluidic device. Experimental results using this magnetic nanoparticle-based bacterial separation device suggested that it significantly reduced the levels of bacteria in the blood of a rodent model. It was hypothesized that the spread of bacteria to distal organs would be significantly lowered with the decrease in bacterial concentration in the bloodstream[25]. Also, it was postulated that broad-spectrum antibiotic therapy, such as colistin methanosulfate, could be co-administered with this bacterial separation therapy, resulting in faster bacterial clearance rates.

Magnetic nanoparticle-based extracorporeal bacterial separation could prove to be an effective adjuvant therapy for sepsis treatment. To test this hypothesis, an extracorporeal bacterial separation device was incorporated into the kinetic mathematical model, integrating predictions of magnetic bacteria separation under microfluidic flow in combination with colistin methanosulfate antibiotic treatment. The approach was used to explore the possible benefits of magnetic nanoparticle-based bacterial separation from blood in conjunction with antibiotic treatment on the time-dependent bacterial load among organs during sepsis.

Bacterial Separation Combined with Antibiotic Therapy

The predicted effect of extracorporeal bacterial separation for the purpose of clearing *A. baumannii* from the blood is demonstrated in Figure 3.6. Addition of magnetic nanoparticle-based bacterial separation operating at an ideal 100% efficiency and processing one-fifth of the total blood volume per hour, in conjunction with antibiotic treatment, resulted in *A. baumannii* clearance from the blood compartment in 27 hours less time than antibiotic treatment alone (Fig 3.6). Bacterial clearance rate associated with this combined treatment was 49% faster than antibiotic treatment alone (Table 3.6). This is a significant result because for each hour that a septic patient is not effectively treated, the risk of mortality increases by 7.6%[117].

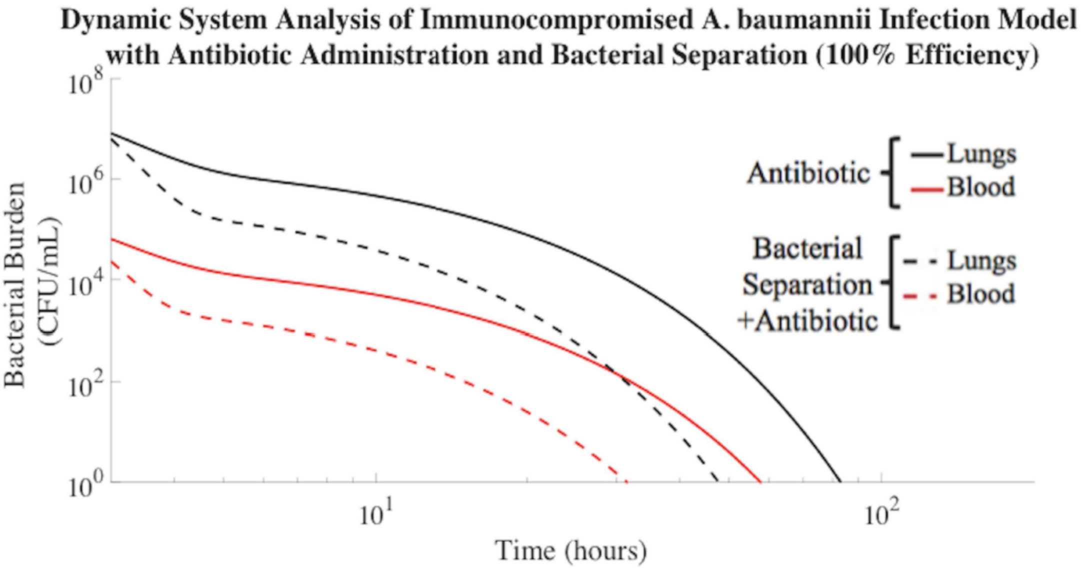

Figure 3.6. Bacterial separation (100% efficiency) combined with antibiotic administration improved *A. baumannii* clearance rate. *A. baumannii* cleared from the blood compartment of the immunocompromised rodent model in 28 h when implementing bacterial separation (100% efficiency) and antibiotic treatment. Antibiotic administration alone resulted in bacterial clearance from the blood compartment in 55 h.

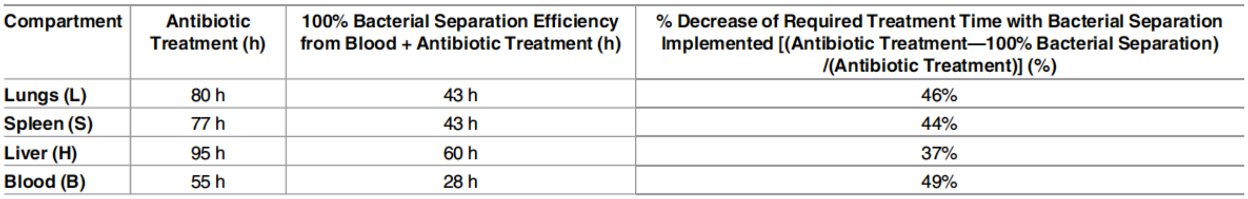

Compartment	Antibiotic Treatment (h)	100% Bacterial Separation Efficiency from Blood + Antibiotic Treatment (h)	% Decrease of Required Treatment Time with Bacterial Separation Implemented [(Antibiotic Treatment—100% Bacterial Separation) /(Antibiotic Treatment)] (%)
Lungs (L)	80 h	43 h	46%
Spleen (S)	77 h	43 h	44%
Liver (H)	95 h	60 h	37%
Blood (B)	55 h	28 h	49%

Table 3.6. *A. baumannii* clearance (≤1 CFU/mL) time improved upon addition of 100% efficient bacterial separation.

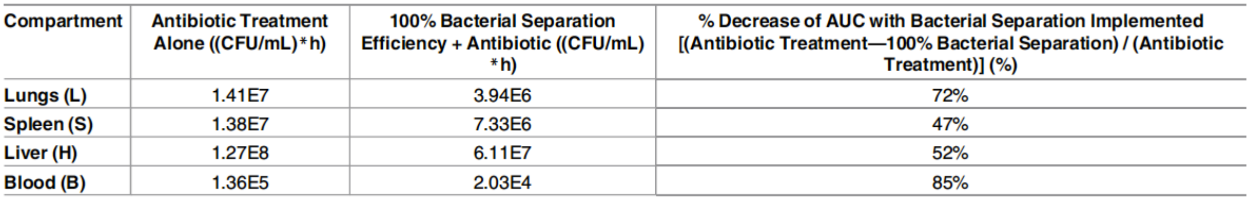

Compartment	Antibiotic Treatment Alone ((CFU/mL)*h)	100% Bacterial Separation Efficiency + Antibiotic ((CFU/mL) *h)	% Decrease of AUC with Bacterial Separation Implemented [(Antibiotic Treatment—100% Bacterial Separation) / (Antibiotic Treatment)] (%)
Lungs (L)	1.41E7	3.94E6	72%
Spleen (S)	1.38E7	7.33E6	47%
Liver (H)	1.27E8	6.11E7	52%
Blood (B)	1.36E5	2.03E4	85%

Table 3.7. Bacteria separation in immunocompromised *A. baumannii* rodent model reduced bacterial burden experienced.

The AUCs of Figure 3.6 were also evaluated. The model suggested that the liver experienced a 52% reduction in AUC with the addition of bacterial separation in the presence of antibiotic (Table 3.7). With bacterial separation occurring at 100% efficiency, the extracorporeal bacterial separation device had a significant impact on overall bacterial clearance and diffusion rates. The total bacterial burden in the blood compartment decreased by an order of magnitude compared to antibiotic treatment alone. Also, the incorporation of the 100% effective bacterial separation device into the model inhibited bacterial proliferation and diffusion from the initial inoculation point of the lungs, thereby lowering the overall bacteria burden in all compartments.

Device Optimization Based on Bacterial Separation Efficiency

Bacterial separation efficiency has a significant impact on the rate of bacteria removal from the blood compartment (Fig 3.7). As previously displayed in Table 3.6, 100% separation efficiency promoted the clearance of *A. baumannii* from the blood in 27 hours less time than antibiotic treatment alone. To explore the role of separation efficiency on predicted bacterial load *in vivo*, model analysis was carried out for separation efficiencies of 60% and 20%. This approach was intended to inform the design constraints of extracorporeal bacteria separation devices for impact in complex living systems. 60% bacterial separation efficiency resulted in clearance of *A. baumannii* from the blood compartment in 20 hours less time that antibiotic treatment alone (Table 3.8). As the separation efficiency further decreased to 20%, bacterial removal became ineffective. Therefore, device design features that impact bacterial separation efficiency and nonlinearly influence clearance must be considered for proposed applications.

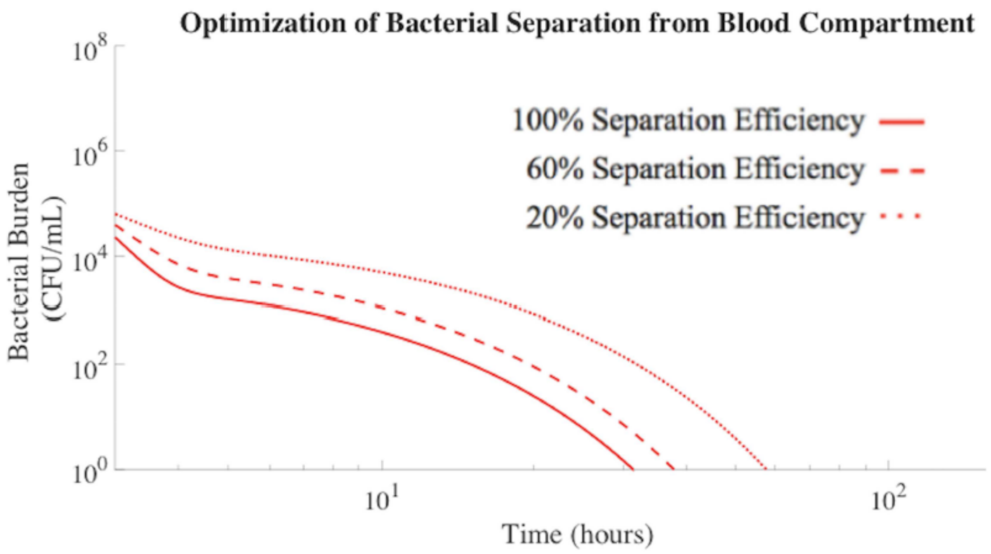

Figure 3.7. Bacterial separation (100% and 60% efficiency) improved *A. baumannii* clearance rates from the blood compartment. 20% bacterial separation efficiency was not efficient enough to impact the overall bacterial clearance rate and resulted in the same clearance rates as antibiotic treatment alone.

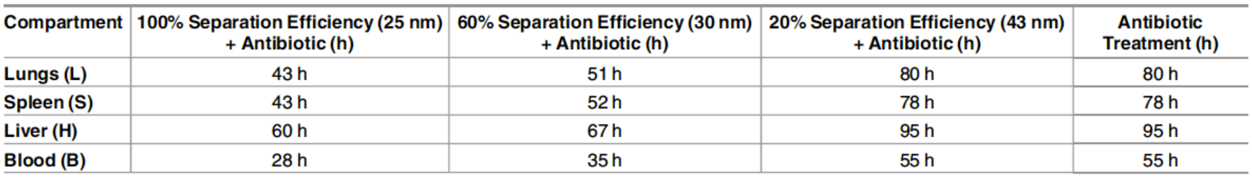

Compartment	100% Separation Efficiency (25 nm) + Antibiotic (h)	60% Separation Efficiency (30 nm) + Antibiotic (h)	20% Separation Efficiency (43 nm) + Antibiotic (h)	Antibiotic Treatment (h)
Lungs (L)	43 h	51 h	80 h	80 h
Spleen (S)	43 h	52 h	78 h	78 h
Liver (H)	60 h	67 h	95 h	95 h
Blood (B)	28 h	35 h	55 h	55 h

Table 3.8. *A. baumannii* clearance (≤1 CFU/mL) time in immunocompromised rodent model accelerated with improved bacterial separation efficiencies.

Total bacteria separation efficiencies produced by the mathematically modeled extracorporeal separation devices were dependent on nanoparticle size. As the nanoparticle radius increased, the bacterial separation efficiency decreased, resulting in slower clearance of bacteria from blood (Fig 3.8). The collision rate constant decreased as the nanoparticle radius increased, resulting in less total nanoparticle interaction with, and binding to, bacteria[26]. Once the nanoparticle radius exceeded approximately 40 nm, the efficiency of bacterial binding and capture was not significant enough to impact the overall rate of bacterial clearance. The optimal nanoparticle size for bacteria capture and removal was estimated to be 25 nm or less, which directly corresponded to previously published literature[26]. The reduced mass of smaller nanoparticles, however, decreases the magnetic attraction force[26]. Thus, careful attention to the design of the separation device is required to achieve efficiency compatible with predicted improvement in overall bacterial clearance. Therefore, multiple, interconnected nanotechnology design features are important considerations in magnetic nanoparticle-based bacterial separation devices.

The impact of bacterial separation efficiency was evaluated by the mathematical model and reported in terms of resultant total bacterial load, or AUC, experienced by each tissue compartment of an *A. baumannii* infected immunocompromised rodent. As the nanoparticle radius increased above 25 nm, the overall separation efficiency characteristic of the extracorporeal bacterial separation device decreased. Table 3.9 demonstrated that as the nanoparticle radius increased above 25 nm, the total bacterial burden experienced by each compartment also increased. All other parameters held constant, a nanoparticle radius of 43 nm is equivalent to a 20% separation efficiency, which has no significant effect on the AUC compared to antibiotic treatment alone. Therefore, in order for magnetic nanoparticle-based bacterial separation devices to aid in the reduction of the total bacterial burden within each compartment, the efficiency of bacterial separation from the blood compartment must exceed 20%.

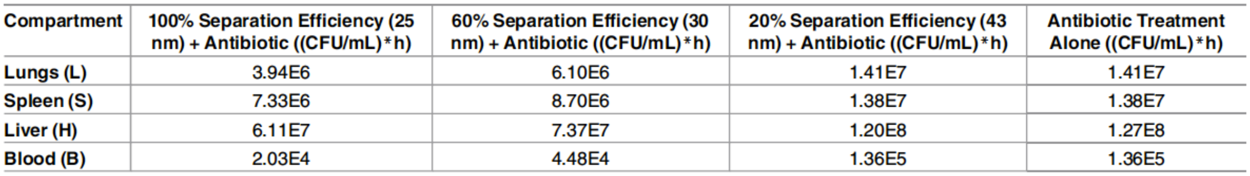

Compartment	100% Separation Efficiency (25 nm) + Antibiotic ((CFU/mL)*h)	60% Separation Efficiency (30 nm) + Antibiotic ((CFU/mL)*h)	20% Separation Efficiency (43 nm) + Antibiotic ((CFU/mL)*h)	Antibiotic Treatment Alone ((CFU/mL)*h)
Lungs (L)	3.94E6	6.10E6	1.41E7	1.41E7
Spleen (S)	7.33E6	8.70E6	1.38E7	1.38E7
Liver (H)	6.11E7	7.37E7	1.20E8	1.27E8
Blood (B)	2.03E4	4.48E4	1.36E5	1.36E5

Table 3.9. Bacteria separation efficiencies greater than 20% reduced bacterial burden in *A. baumannii* immunocompromised rodent model.

Bacterial Separation for Treatment of Bacterial Sepsis in Human Model

The use of extracorporeal bacterial separation for treatment of sepsis in humans has never been explored experimentally or by mathematical modeling. The successful rodent model was modified to explore the possible benefits of magnetic nanoparticle-based extracorporeal bacterial separation in humans during an episode of sepsis. By incorporating human parameters into the model and adjusting for the tissue volume differences of humans compared to rodents, we were able to estimate the impact of bacterial separation, in conjunction with antibiotic treatment. The model extrapolation to humans has known, and, likely, unknown limitations. However, this approach is a first step towards an understanding of the extracorporeal bacterial clearance necessary for biological impact.

Sepsis occurs in an adult humans when the bacterial burden reaches approximately 10 CFU/mL in the bloodstream or 10^3 CFU/mL in the lungs[118–120]. Therefore, our model incorporated these parameters as markers to indicate the time at which to apply extracorporeal bacterial separation and antibiotic treatment. Results suggested that *A. baumannii* clearance from the blood compartment was reduced by 14 hours with the addition of 100% efficient extracorporeal bacterial separation treatment, compared to antibiotic treatment alone (Fig 3.8). The flow rate through the bacterial separation compartment was programmed to process one-fifth of the total human blood volume per hour, similar to the blood flow rates used during kidney dialysis in humans. Based on the AUCs of Figure 3.8, the combination therapy approach decreased the total bacterial burden in the model compartments, with the most significant difference in the blood compartment (Table 3.10).

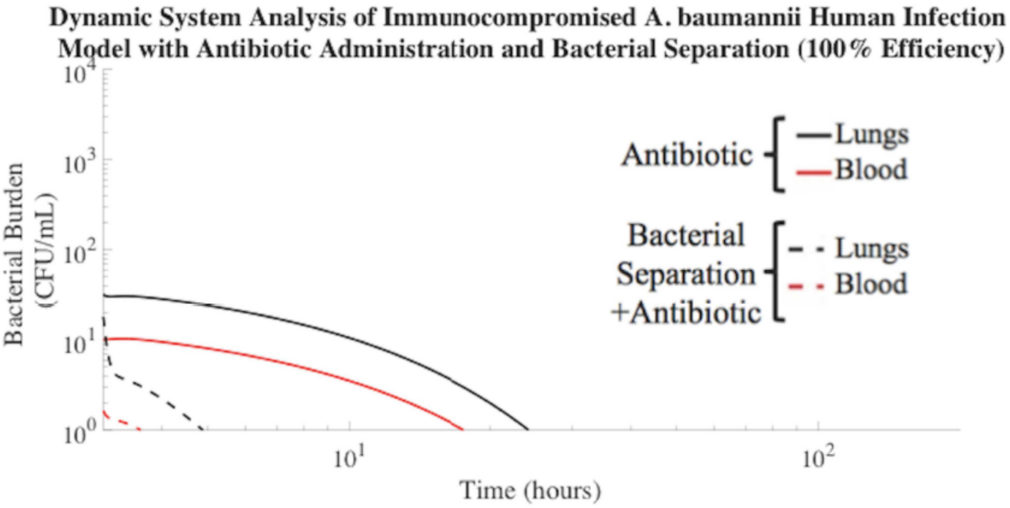

Figure 3.8. Bacterial separation (100% efficiency) with antibiotic treatment improved *A. baumannii* clearance from human blood compartment. This combination treatment resulted in *A. baumannii* clearance (≤1 CFU/mL) from the blood compartment in 1 h. The time required for *A. baumannii* to be cleared to a negligible concentration (≤ 1 CFU/mL) from the blood compartment of the human model with antibiotic administration alone was 15 h.

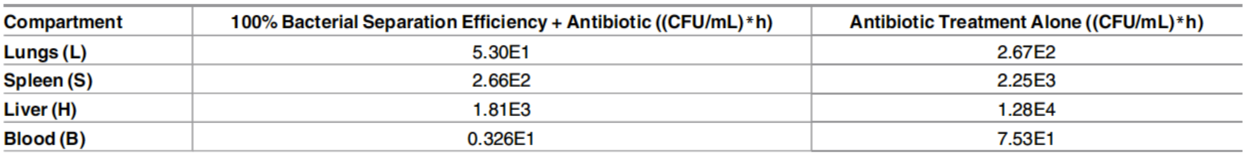

Compartment	100% Bacterial Separation Efficiency + Antibiotic ((CFU/mL)*h)	Antibiotic Treatment Alone ((CFU/mL)*h)
Lungs (L)	5.30E1	2.67E2
Spleen (S)	2.66E2	2.25E3
Liver (H)	1.81E3	1.28E4
Blood (B)	0.326E1	7.53E1

Table 3.10. Bacteria separation (100% efficiency) in *A. baumannii* human model reduced bacterial burden experienced.

This work is the first to estimate, by mathematically models, bacterial load as a surrogate of the ultimate biological impact of infection. Bacterial load, or AUC, is directly correlated to the progression of sepsis and death[121]. Therefore, extracorporeal bacterial separation devices designed to operate at high efficiencies would not only significantly reduce the total bacterial load, but may also inhibit the progression of sepsis. Inhibition of disease progression would provide additional time to identify ideal therapies for infected patients, while reducing the mortality rates associated with sepsis.

Bacterial Separation for Treatment of Multi-Drug Resistant Sepsis in Human Model

Bacterial species identification in the clinical setting takes one to three days, a time during which the patient is treated with broad-spectrum antibiotics. This method is not optimal, especially for patients suffering from MDR infections. Sepsis caused by a MDR infection is one of the most critical public health issues, even in first-world countries[122]. The increasing frequency of MDR bacterial strains is leading into the ‘post-antibiotic era’.

MDR-associated sepsis was mathematically modeled by assuming that the MDR *A. baumannii* were 50% less susceptible to antibiotic treatment than non-MDR *A. baumannii*. Bacterial infection that is 0% susceptible to antibiotic treatment behaves similarly to the trajectory shown in Figure 3.4 of untreated infection, whereas infection that is 100% susceptible to antibiotic treatment was shown in Figure 3.5. Choosing a MDR *A. baumannii* susceptibility of 50% allows for quantitative evaluation of model sensitivity to the degree of bacterial antibiotic resistance. Figure 3.9 described the clearance of MDR *A. baumannii* using the additional assistance of 100% efficient extracorporeal bacterial separation, compared to antibiotic treatment alone. The addition of extracorporeal bacterial separation operating at 100% efficiency resulted in MDR *A. baumannii* clearance from the blood of a human mathematical model in 1 h, which was 97% faster than antibiotic treatment alone. Antibiotics prove less effective in the treatment of MDR sepsis, which highlights the need for alternative treatment methods. Bacterial separation treatment methods have been shown to bind and remove multiple clinical isolates of antibiotic-resistant organisms[25].

This supports the development of new engineering-based bacterial separation devices to combat MDR bacteria and delay progression to septic shock.

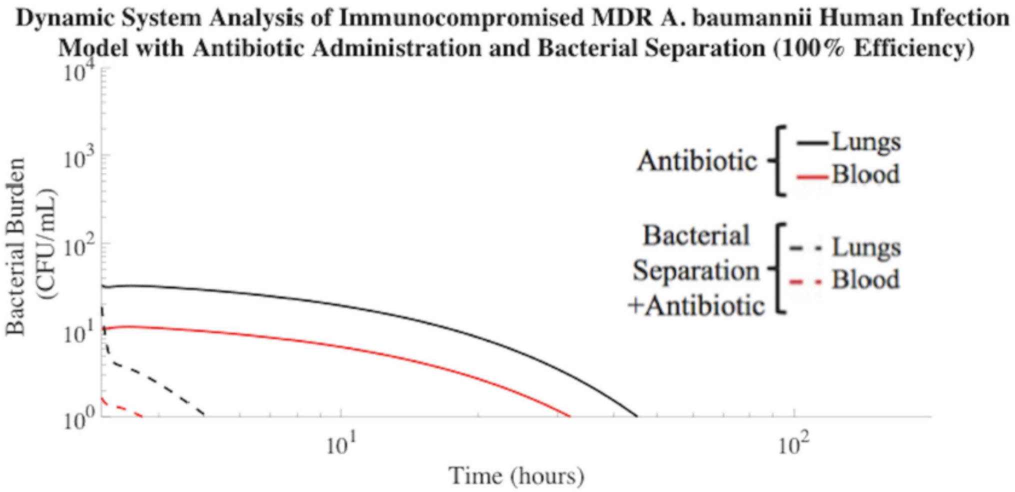

Figure 3.9. Treatment of MDR *A. baumannii* human model using 100% efficient bacterial separation with antibiotic treatment. Using this combination therapy, MDR *A. baumannii* clearance (≤ 1 CFU/mL) from the blood compartment of the human mathematical model occurred in 1 h. The time required for MDR *A. baumannii* to be cleared to a negligible concentration (≤1 CFU/mL) from the blood compartment with antibiotic administration alone was 29 h.

Conclusions

Mathematical modeling established that extracorporeal bacterial separation reduced the total bacterial burden in the bloodstream of a septic subject by an order of magnitude, compared to antibiotic treatment alone. This correlated to a 49% reduction in non-MDR bacterial exposure time due to the addition of extracorporeal bacterial separation therapy. Efficient bacterial separation also reduced the spread of bacteria to distal sites. Results further indicated that engineering-based bacterial separation devices could offer a particularly effective therapeutic strategy for patients suffering from MDR infections that render existing drug therapies inadequate. The addition of extracorporeal bacterial separation resulted in MDR bacterial clearance from the blood of a human mathematical model in 97% less time than antibiotic treatment alone. This was a notably important prediction because decreasing the length of bacterial infection significantly reduces the risk of mortality associated with sepsis[117]. The lack of antibiotics in the developmental pipeline, combined with the increasing rate of MDR, has created a dire need for the discovery of new therapies effective against MDR bacterial infections. Therefore, development of mathematical models is necessary to rapidly determine the effectiveness of new treatment therapies, such as extracorporeal bacterial separation. Our work was the first dynamic mathematical model to demonstrate the potential usefulness of extracorporeal bacterial separation for the treatment of sepsis and its MDR counterpart.

Engineers have had a profound impact on the development of disease treatment systems, such as kidney dialysis devices. It is clear that engineers also have a role to play in the design of extracorporeal bacterial separation devices. To aid in the optimization of bacterial separation device design, more experimental data quantifying bacterial load in living systems must be gathered to better understand the correlation between bacterial load and patient outcome.

Currently, data describing bacterial load in rodent systems is sparse, and corresponding human data is even less prevalent. These are key pieces of information that must be obtained in order to confidently design new treatment methods that reduce total bacterial burden, duration of infection, and the ‘post-antibiotic era’ threat. Designing extracorporeal bacterial separation devices that remove bacteria from the blood at a rate deemed biologically relevant by this information may inhibit the progression of sepsis, decrease overall mortality rates, and help combat MDR bacterial infections.

Summary

Extracorporeal blood cleansing devices are of particular interest as they possess the potential capability of pathogen removal from whole blood in the absence of effective antibiotic treatment. This model of sepsis suggests that blood cleansing devices have the potential to significantly reduce the bacterial load in the blood of septic animals and humans. We have computationally modeled and predicted the effects of broad-spectrum antibiotic treatment with and without the addition of bacterial separation therapy in subjects suffering from sepsis. Implementing mechanical bacterial separation reduced duration of infection by 49% in model subjects suffering from antibiotic sensitive sepsis, according to our modeling predictions. Furthermore, our model predicted even more significant effects in subjects suffering from antibiotic resistant infection. **This work successfully fulfills Specific Aim 2 of this dissertation**. Figure 3.10 highlights this work, which was featured in *PLOS ONE*, Volume 11, Issue 9 [27].

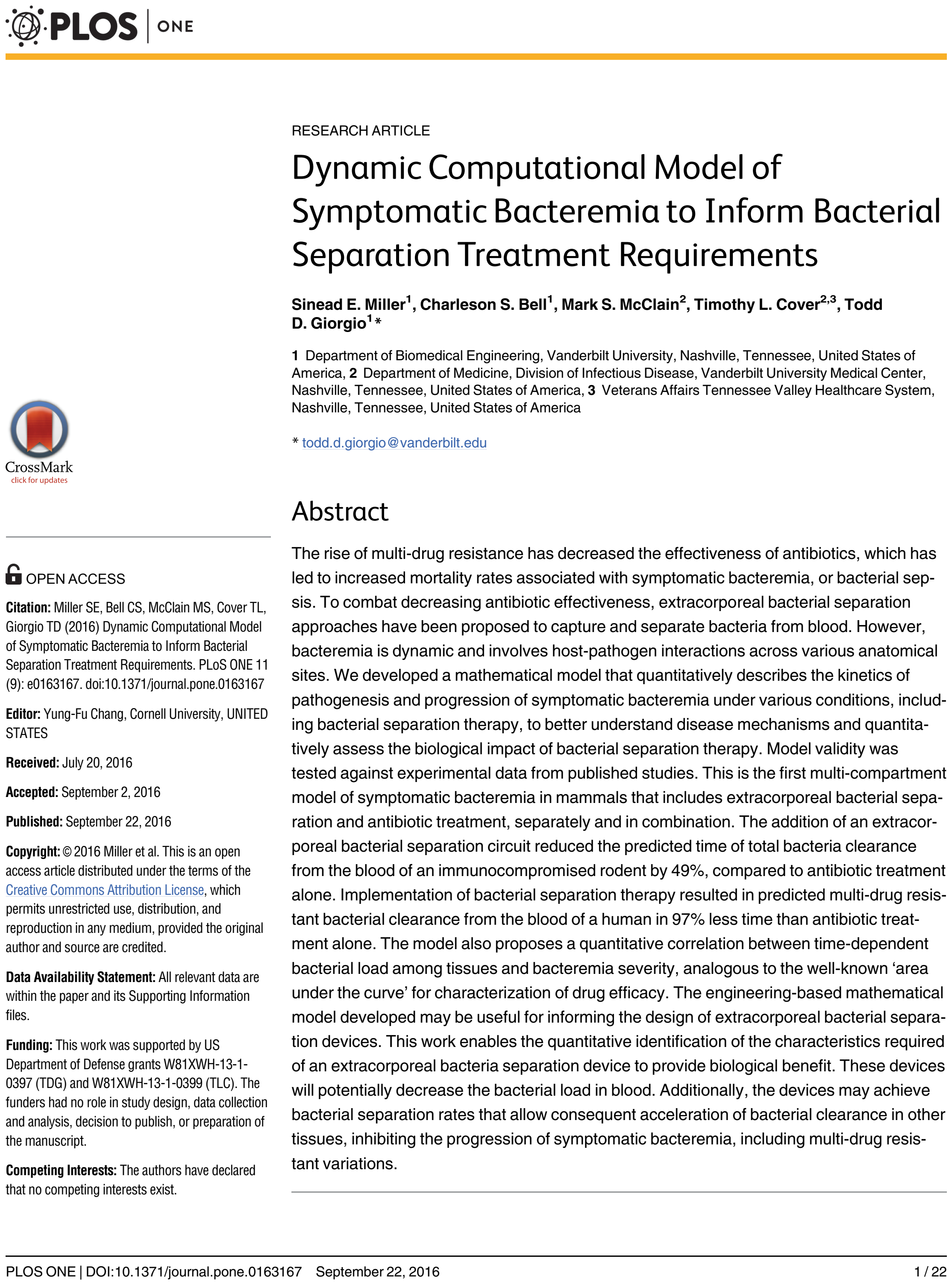

PLOS | ONE

RESEARCH ARTICLE

Dynamic Computational Model of Symptomatic Bacteremia to Inform Bacterial Separation Treatment Requirements

Sinead E. Miller[1], Charleson S. Bell[1], Mark S. McClain[2], Timothy L. Cover[2,3], Todd D. Giorgio[1]*

1 Department of Biomedical Engineering, Vanderbilt University, Nashville, Tennessee, United States of America, **2** Department of Medicine, Division of Infectious Disease, Vanderbilt University Medical Center, Nashville, Tennessee, United States of America, **3** Veterans Affairs Tennessee Valley Healthcare System, Nashville, Tennessee, United States of America

* todd.d.giorgio@vanderbilt.edu

Citation: Miller SE, Bell CS, McClain MS, Cover TL, Giorgio TD (2016) Dynamic Computational Model of Symptomatic Bacteremia to Inform Bacterial Separation Treatment Requirements. PLoS ONE 11 (9): e0163167. doi:10.1371/journal.pone.0163167

Editor: Yung-Fu Chang, Cornell University, UNITED STATES

Received: July 20, 2016

Accepted: September 2, 2016

Published: September 22, 2016

Data Availability Statement: All relevant data are within the paper and its Supporting Information files.

Funding: This work was supported by US Department of Defense grants W81XWH-13-1-0397 (TDG) and W81XWH-13-1-0399 (TLC). The funders had no role in study design, data collection and analysis, decision to publish, or preparation of the manuscript.

Competing Interests: The authors have declared that no competing interests exist.

Abstract

The rise of multi-drug resistance has decreased the effectiveness of antibiotics, which has led to increased mortality rates associated with symptomatic bacteremia, or bacterial sepsis. To combat decreasing antibiotic effectiveness, extracorporeal bacterial separation approaches have been proposed to capture and separate bacteria from blood. However, bacteremia is dynamic and involves host-pathogen interactions across various anatomical sites. We developed a mathematical model that quantitatively describes the kinetics of pathogenesis and progression of symptomatic bacteremia under various conditions, including bacterial separation therapy, to better understand disease mechanisms and quantitatively assess the biological impact of bacterial separation therapy. Model validity was tested against experimental data from published studies. This is the first multi-compartment model of symptomatic bacteremia in mammals that includes extracorporeal bacterial separation and antibiotic treatment, separately and in combination. The addition of an extracorporeal bacterial separation circuit reduced the predicted time of total bacteria clearance from the blood of an immunocompromised rodent by 49%, compared to antibiotic treatment alone. Implementation of bacterial separation therapy resulted in predicted multi-drug resistant bacterial clearance from the blood of a human in 97% less time than antibiotic treatment alone. The model also proposes a quantitative correlation between time-dependent bacterial load among tissues and bacteremia severity, analogous to the well-known 'area under the curve' for characterization of drug efficacy. The engineering-based mathematical model developed may be useful for informing the design of extracorporeal bacterial separation devices. This work enables the quantitative identification of the characteristics required of an extracorporeal bacteria separation device to provide biological benefit. These devices will potentially decrease the bacterial load in blood. Additionally, the devices may achieve bacterial separation rates that allow consequent acceleration of bacterial clearance in other tissues, inhibiting the progression of symptomatic bacteremia, including multi-drug resistant variations.

PLOS ONE | DOI:10.1371/journal.pone.0163167 September 22, 2016 1 / 22

Figure 3.10. Cover of work published in *PLOS ONE*, Volume 11, Issue 9 [27].

CHAPTER IV

FLUIDIC PLATFORM FOR CAPTURE OF BLOOD-BORNE PATHOGENS

The purpose of this chapter is to develop a microfluidic device capable of capturing *A. baumannii* from fluids. The double spiral microchannel is an attractive method for focusing micron-sized particles, but has never been successfully implemented for bacteria. Using the double spiral fluidic platform, I was able to separate and focus various sized microparticles, as well as *A. baumannii*. I geometrically designed the double spiral fluidic platform to cause *A. baumannii* to streamline near the microchannel walls. Also, I functionalized the double spiral walls with colistin to promote *A. baumannii* capture within the device. Results from Chapter IV will fulfill Specific Aim 3 of my dissertation. The work detailed in this chapter will be submitted for publication in a peer-reviewed journal during February of 2017.

Introduction

The presence of bacteria in the circulatory blood initiates a cascade of local and systemic regulatory mechanisms that can result in sepsis[1]. Sepsis is the leading cause of death in the critically ill in the United States[2,3]. Currently, no specific sepsis treatment is available. Treatment relies on early recognition and rapid administration of appropriate antibiotics, fluid resuscitation, and vasoactive medications[123,124]. Early, effective antibiotic therapy is essential and improves patient outcomes[125,126]. However, sepsis-associated mortality remains unacceptably and persistantly high, highlighting the need for new sepsis therapies.

Much research has been done to evaluate experimental adjunct treatments for sepsis, such as extracorporeal cytokine filtration[127], recombinant human activated protein C[128], corticosteroids[129], human recombinant lactoferrin[130], and immunomodulation[131]. Although immunomodulation has been widely anticipated, the heterogeneity of the patient population and the complexity of sepsis pathogenesis have limited advancement of these experimental approaches. Blockage of single mediators, such as interleukin-1 (IL-1) or tumor necrosis factor-alpha (TNF-α), has shown little promise in improving sepsis survival. Cytokine removal has displayed encouraging results in animal studies, however, results are believed to be a consequence of modulating other downstream mechanisms rather than the direct impact of cytokine removal[132]. Benefits of endotoxin clearance have shown efficacy in animal studies, but have yet to demonstrate improvement of septic patient outcomes[29,133].

Mechanical bacterial removal using magnetic nanoparticles has been reported to improve survival of septic rodent models[25]. Surface modification of nanoparticles using bacterial targeting ligands can lead to the efficient and reproducible capture of several important pathogenic bacteria[52,73,134]. However, these approaches suffer from potential limitations in scale-up for treatment of large living systems and uncertain regulatory hurdles in regard to blood contact with nanoparticles. Treatment addressing either a single molecular activator/inhibitor or isolation of the bacterial source is likely to insufficiently addresses the complexity of sepsis. It is imperative to develop a clinically translatable, alternative therapy for sepsis that can remove both the pathogenic bacteria and modulate the resulting molecular effectors to help mitigate the systemic inflammatory response characteristic of sepsis and inhibit sepsis progression.

We have designed and validated a blood purification device that is capable of removing endotoxin and Gram-negative bacteria, including drug resistant strains, from peripheral blood using inertial-based cell separation in combination with a broad-spectrum polycationic ligand. We expect that the device can be simply modified to also remove Gram-positive bacteria, providing a system capable of removing bacteria in the absence of strain identification, in addition to sequestering endotoxins. This device is based on a double spiral microfluidic design. We demonstrate, for the first time, the use of inertial-based forces for the focusing and separation of bacteria from flowing fluids, including whole, human blood. This novel blood purification technique resulted in significant removal of bacteria and endotoxin from circulation, making this device a promising adjuvant treatment and potential diagnostic for sepsis and other pathogenic diseases.

Our technology is the first to overcome the issues observed in blood purification therapies that utilize membrane-based or column-type filters for removal of inflammatory mediators and other toxins from blood. Inertial-based focusing avoids clogging, poor efficiency of targeted element removal, and excessive removal of useful substances, such as blood components, which limit the translational potential of existing approaches.

In laminar Poiseuille flow, the hyperbolic velocity profile has a maximum velocity at the centroid of the channel and zero velocity at the walls of the channel[135]. The lift forces (F_L) acting on particles are dominated by wall-induced (F_1) and shear-induced (F_2) lift forces[31,136,137]. These lift forces act in conjunction to yield a particle equilibrium position between the channel wall and centerline where the oppositely directed lift forces are equal and generate narrow particle bands[31,138–140]. The net lift force (F_L) that causes particles to migrate away from the channel center and walls is estimated as, $F_L = f_L(Re,x_L)\rho U_m^2 a_p^4/D_h^2$, where the lift coefficient (f_L) is a function of the channel Reynolds number Re ($Re = \rho U_m D_h/\mu$) and the particle position (x_L) within the cross-section of the channel[32,136,141]. D_h is the microchannel hydraulic diameter, ρ *and* μ are the density and viscosity of fluid, U_m is the maximum fluid velocity, and a_p is the particle diameter.

In curved microfluidic channels, non-uniform inertia of fluid results in the development of secondary transverse flows, or Dean vortex flows, in the top and bottom halves of the channel (Fig 4.1)[31]. The dimensionless Dean number (De), used to characterize the Dean vortex flow in a curved microchannel, can be defined as, $De = (\rho U_f D_h)/\mu)\sqrt{(D_h/2R)}$, where R is the radius of curvature and U_f is the average fluid velocity[142]. Assuming Stokes drag, the magnitude of the Dean drag force (F_D) exerted on particles due to these flows can be estimated by[142] $F_D = 5.4*10^{-4}(\pi)(\mu)(De^{1.63})(a_p)$.

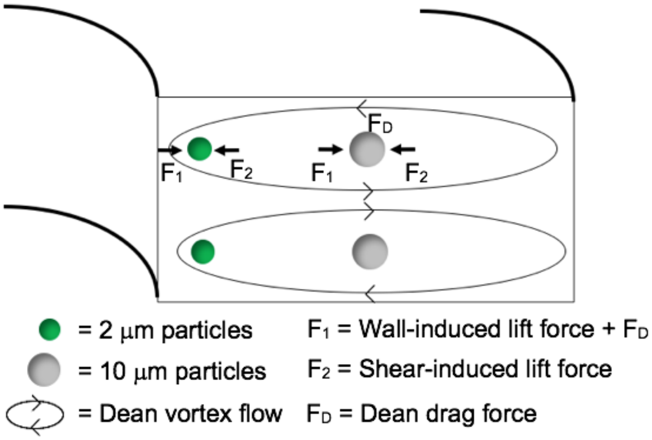

Figure 4.1. Asymmetry in a spiral channel. Transverse Dean flows exert a Dean drag force (F_D) on particles flowing in a spiral channel. The competition between wall lift force, shear lift force, and Dean drag force results in differential migration of particles to unique equilibrium positions dependent of particle size[143].

The equilibrium positions of particles in flow are primarily determined by the interactions between lift forces and Dean drag force. The double spiral geometry in this design was formulated to cause bacteria-sized particles to occupy equilibrium positions near the microchannel walls when exposed to a flow rate of 0.2 mL min^{-1}. This allows bacteria to come in close proximity to the polycationic ligand functionalized microchannel walls, which leads to bacteria and endotoxin capture. To accomplish this, the double spiral microchannel was dimensionally designed to have a 406 mm length (L), 300 μm width (W), and 15 μm height (H) with six spiral loops for each direction (Fig 4.2). Our work is the first to accomplish hydrodynamic separation and capture of bacteria and endotoxin in a curved geometry. The double spiral microchannel described has a low aspect ratio ($H/W = 0.05$). The low aspect ratio of the microchannel rapidly forces particles and bacteria to migrate to final equilibrium positions.

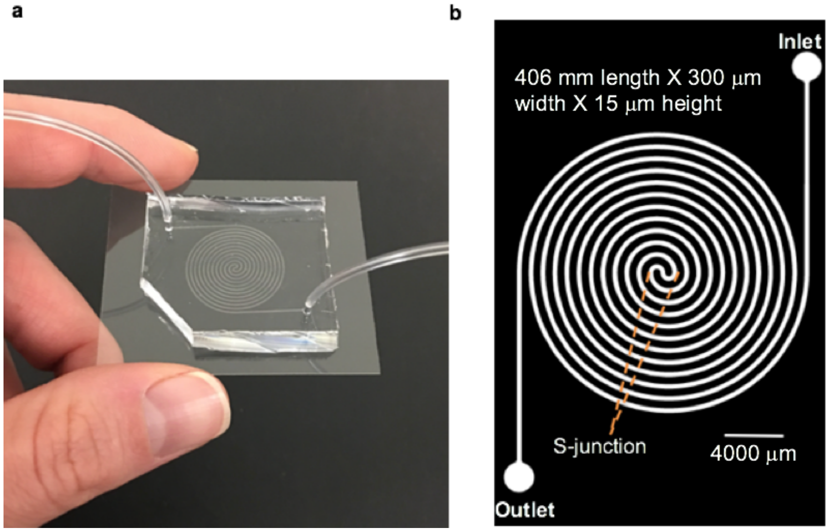

Figure 4.2. Double spiral microfluidic design to maximize bacterial separation efficiency. **a**, Fabricated PDMS microfluidic device consisting of two, 6-loop spiral microchannels joined at the S-junction to form a double spiral channel with one inlet and one outlet for particle/bacterial cell separation. **b**, CAD drawing of the double spiral fluidic module employed to create the master mold.

Materials and Methods

Synthesis of Colistin-PEG-Silane ligand

NHS-PEG-Silane (*N*-Hydroxysuccinimide-Polyethylene glycol$_{1000}$-Silane, Nanocs, Inc., Lot #160429) (30 mg mL^{-1}) was dissolved in ethanol/water, pH 5 (50/50 v/v%, pH adjusted with acetic acid). 35 mg mL^{-1} of colistin sulfate (Sigma-Aldrich, Lot #SLBN5158V) was added to the NHS-PEG-Silane solution. The solution was vortexed for 30 seconds and then allowed to react at 21°C for 2 h. NHS was used to couple a heterobifunctional NHS-PEG-Silane linker to one of the five similarly reactive L-α-diaminobutyric acid (Dab) residues of colistin, resulting in Colistin-PEG-Silane[59–61,73].

PEG-Silane ligand solution preparation

PEG-Silane (Polyethylene glycol$_{1000}$-Silane, Nanocs, Inc., Lot #160706OH) (30 mg mL^{-1}) was dissolved in ethanol/water, pH 5 (50/50 v/v%, pH adjusted with acetic acid). The solution was vortexed for 30 seconds and then allowed to incubate at 21°C for 2 h.

Design and fabrication of device

In designing the proposed double spiral microfluidic device, the effects of Dean drag and the lift forces were accounted for. The spiral geometry in this design was formulated to cause 2 μm particles (a_p) to occupy a single equilibrium position near the microchannel inner wall at a flow rate of 0.2 mL/min. To accomplish this, the microchannel was designed to be 300 μm wide and 15 μm high (a_p/h ~0.13).

Microchannel hydraulic diameter, D_h, was calculated as follows

$$D_h = \frac{2wh}{(w+h)} = 2.857\text{E}^{-5}\ \text{m} \tag{4.1}$$

where w is the channel width (300 μm) and h is the channel height (15 μm). The average fluid velocity, U_f, at the desired volumetric flow rate of 3.33E-9 m^3/s is calculated as follows

$$U_f = \frac{Q}{A} = \frac{3.33E^{-9}\ m^3/s}{4.5E^{-9}\ m^2} = 0.74\ {}^{m}/_{s} \tag{4.2}$$

where *A* is the vertical cross sectional area (width * height) of the channel. The magnitude of the secondary Dean flows, *De*, can now be solved[142]:

$$De = \frac{\rho U_f D_h}{\mu}\sqrt{\frac{D_h}{2R}} = 0.285 \tag{4.3}$$

where ρ is the density of fluid (ρ_{blood} = 1060 kg m^{-3}), μ is the fluid viscosity ($\mu_{blood} = 3*10^{-3}$ kg m^{-1} s^{-1}), and *R* is the radius of curvature (0.0098 m) of the convex surface of the channel path. Depending on particle size, channel geometry, and flow rate, transverse secondary Dean flows can entrap particles in one of the two Dean vortices. Assuming Stokes drag, the Dean drag force, F_D, exerted on particles due to these flows can be calculated:

$$F_D = 5.4 * 10^{-4}\pi\mu De^{1.63}a_p \tag{4.4}$$

where a_p is the particle diameter. In addition to F_D, the particles also experience a net lift force (F_L), which is a combination of shear induced inertial lift forces and wall induced lift forces. Asomolov et al. derived an equation for net inertial lift force that takes into account both shear-induced and wall-induced lift forces[136]:

$$F_L = \rho G^2 C_L a_p^4 \tag{4.5}$$

where *G* is the shear rate of the fluid (s^{-1}) and C_L is the lift co-efficient as a function of the particle position across the channel cross-section. The shear rate of the fluid, *G*, is given by $G = U_{max}/D_h$. U_{max} is the maximum fluid velocity (m s^{-1}) and can be approximated as $2U_f$[142]. C_L is assumed to have an average value of 0.5[144,145]. If the Dean drag force acting on the particles is less than the corresponding net lift force, then the lift force dominates and the particles equilibrate. A summary of the magnitude of the forces imposed on 2 μm, 5 μm and 10 μm particles using the described fluidic device is shown in Table 4.1.

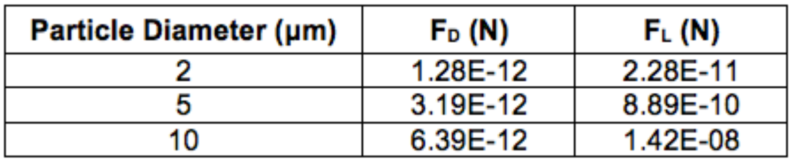

Particle Diameter (μm)	F_D (N)	F_L (N)
2	1.28E-12	2.28E-11
5	3.19E-12	8.89E-10
10	6.39E-12	1.42E-08

Table 4.1. Summary of Dean drag force (F_D) and the net lift force (F_L) acting on 2, 5 and 10 μm particles at 0.2 mL/min.

To achieve complete focusing of the 2 μm particles, it is also essential to determine the length of the spiral microchannel needed for the 2 μm particles to focus into a stream prior to reaching the channel outlets. The expression for particle lateral migration velocity (U_L) is[136]

$$U_L = \frac{\rho U_{max}^2 a_p^3 C_L}{3\pi\mu D_h^2} \tag{4.6}$$

The channel length (L_l) needed for the particles to streamline and focus is described by

$$L_I = \frac{U_f}{U_L} * L_M \tag{4.7}$$

where L_M is the migration length (m), or approximately one half of the channel width (150 μm). The calculated values of L_l are shown in Table 4.2.

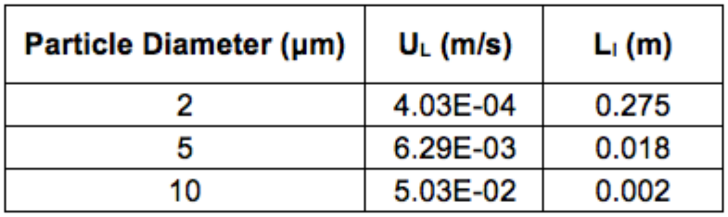

Particle Diameter (μm)	U_L (m/s)	L_l (m)
2	4.03E-04	0.275
5	6.29E-03	0.018
10	5.03E-02	0.002

Table 4.2. Summary of necessary channel length for focusing (L_l).

The double spiral channel length must be sufficiently long in order to satisfy the condition of L_l, thereby allowing formation of a single ordered stream of 2 μm particles along the channel wall prior to reaching the outlet region. The length of the double spiral microchannel was fixed at 0.406m.

The microfluidic device pattern was designed and drawn in AutoCAD software (AutoCAD 2014, AutoDesk, Inc.). The design consisted of a 6-loop double spiral microchannel with one inlet and one outlet. The microchannel rotates clockwise for 6 loops, changes direction through the S-junction, then rotates counterclockwise to form the double spiral. The double spiral microchannel has dimensions of 406 mm *L*, 300 μm *W*, and 15 μm *H*. The spacing between two adjacent loops is 500 μm. The outermost radius of curvature is 9.8 mm. Standard photolithographic techniques[146] were used to generate a mold from a silicon master that was spin coated with a SU8-2010 (MicroChem Corp.) layer (WS-400 Lite Series Spin Processor, Laurell Technologies Corp.) on a 4-inch silicon wafer (Nova Electronic Materials). After soft baking at 95 °C for 5 minutes, the SU-8 layer was patterned using a mask aligner (MJB 3 Mask Aligner, Suss MicroTech) with a UV light (Novacure 2100, Exfo Inc.) and a negative photomask (Infinite Graphics, Inc.). After subsequent post-exposure bake steps at 95 °C for 5 min, the wafer was developed using SU-8 developer (MicroChem Corp.). A final hard bake was performed for 5 min at 150 °C. The wafer was used as the master mold to cast the microfluidic channels. Degassed PDMS (polydimethylsiloxane, mixed in a 10:1 ratio of PDMS base with curing agent, Sylgard 184, Dow Corning Inc.) was cast over the mold and baked at 65 °C for 4 h in an oven. The PDMS with embedded channels was subsequently cut by razor blade and removed from the master mold. One inlet and one outlet were punched through the PDMS using a 1.5 mm biopsy punch (Integra Miltex). The PDMS slab was then bonded to a glass substrate (43 mm X 50 mm, Ted Pella, Inc.) post oxygen plasma treatment (PDC-001 Plasma Cleaner, Harrick Plasma). Immediately following plasma treatment and bonding to the glass cover slip, 1/16” O.D. tygon microbore tubing (Cole Parmer Corp.) was inserted through both the inlet port and outlet port. Colistin was tethered to the double spiral microfluidic device channel walls using the Colistin-PEG-Silane linker and silane chemistry (Appendix B Fig B1)[147]. Colistin-PEG-Silane solution was flowed through the oxidized PDMS microchannel using a 1 mL luer-lock disposable syringe (Becton Dickinson). The Colistin-PEG-Silane solution was allowed to contact the microchannel surface for 30 min at 65 °C, according to well established silanization principals[148]. Use of the heterobifunctional Colistin-PEG-Silane linker was designed to enable colistin decoration of the microchannel walls with a PEG molecular spacer, which was intended to reduce steric hindrance of colistin interactions with bacteria and endotoxin. In the range of physiological pH values, the primary amine groups of colistin are protonated, and, therefore, positively charged[63,64]. The positive charge of colistin allows for binding to the negatively charged outer membrane of Gram-negative pathogens and endotoxin[42]. PEG-Silane functionalized devices were also synthesized using a very similar approach, and used as a PEGylated control group that lacked colistin decoration. No ligand was added to result in non-functionalized double spiral microfluidic devices.

Confirmation of colistin conjugation to microchannel walls

Fluorescent labeling of colistin within the colistinated double spiral microfluidic device was performed using ATTO 488 NHS ester (Sigma-Aldrich, Lot #BCBQ4012V). ATTO 488 NHS ester (2 mg mL^{-1}) was dissolved in dimethylsulfoxide (DMSO, Sigma-Aldrich) immediately prior to use. Labeling was carried out by adding the fluor to the colistinated microchannel, followed by incubation for 30 minutes at room temperature. The stained microchannel was then washed with phosphate buffer saline (PBS, Gibco, Lot #1806048), pH 7.4. The same protocol was used on the PEGylated microchannel as a control. The fluorescently stained microchannels were then imaged using a fluorescent microscope (EVOS FL, Invitrogen). Image-J software was used to quantitate the fluorescent intensity across the channel width of captured images. Dilutions of ATTO 488 NHS ester within non-functionalized microfluidic devices were used as references to generate an ATTO 488 NHS ester standard fluorescence calibration curve. The fluorescence intensity of the colistinated microchannel and the PEGylated microchannel were compared to that of the ATTO 488 NHS ester standard curve, which allowed for quantification of the number of colistin molecules per double spiral microchannel.

Colistin retention

The possibility of Colistin-PEG-Silane ligand disassembly from the surface of the double spiral microfluidic device under flow conditions was evaluated using MaxSignal® Colistin enzyme-linked immunosorbent assay (ELISA) test kit (BIOO Scientific, Lot #109501081415$626311708249). PBS, pH 7.4, was flowed through the colistinated double spiral microfluidic device at 0.2 mL min^{-1} for 2 h. Sample was collected from the device outlet at various time points (1, 2, 4, 5, 10, 20, 30, 45, 60, 120 minutes) for analysis. Total colistin content in each sample was quantified by the colistin ELISA according to the manufacturer's instructions. Absorbance was measured at 450 nm using a microtiter plate reader, and these values were used to calculate the colistin concentration in the samples according to the calibration curve (assay detection range, 0.5 to 50 ng/ml). Results from colistin ligand retention characterization prompted the washing of each double spiral microfluidic device continuously for 30 minutes with 70% ethanol prior to experimental use, resulting in negligible colistin release during the capture studies.

Microbial culture

Bacterial cultures (i.e., *Acinetobacter baumannii* ATCC17978, Colistin-resistant *Acinetobacter baumannii* 19606R[58], Colistin-resistant *Acinetobacter baumannii* 'Patient 2'[149]*, Klebsiella pneumoniae* ATCC70060*3, Bacillus subtilis* 1A578 (Bacillus Genetic Stock Center)[150,151], *Staphylococcus aureus* ATCC29213) were plated on LB agar (Sigma-Aldrich, Lot #SLBR1403V) and grown overnight at 37 °C. Single colonies of each strain were then inoculated in LB broth (1X) (Gibco, Lot # 1803272) and grown at 37 °C, shaking at 150 rpm. Cell concentrations were measured with OD595 spectrometry (Infinite F500, Tecan).

Inertial focusing visualization

Two types of polystyrene microspheres (Spherotech Inc.) with mean diameters of 10.2 μm ± 4 μm and 2 μm ± 0.3 μm were used to analyze particle focusing within the microchannel. Suspensions were provided at 1% w/v with 1 vol% of Tween-20 surfactant (Sigma-Aldrich) to prevent particle aggregation. Equal volumes of two suspensions were diluted to 0.1% w/v using de-ionized (DI) water. The fluorescent particles were individually introduced into the non-functionalized double spiral microchannel at 0.2 mL min^{-1} using an infusion syringe pump (Nexus 3000, Chemyx Inc.) connected to the input port of the microchannel through a 1 mL luer-lock tip syringe and 1/16" O.D. tygon inlet tubing. Particle trajectories and focusing within the double spiral channel were visualized in real-time using fluorescence microscopy (EVOS FL, Invitrogen). This process was repeated using SYTO®9 green fluorescent nucleic acid labeled (5 mM solution in DMSO, Molecular Probes, Lot #1687876A) *A. baumannii* ATCC17978. After a 5-minute incubation with SYTO® 9, the bacteria were washed three times with RNase-free, ultrapure water (USB Corp., Lot #4235512) and resuspended to a concentration of ~8 X 10^7 colony forming units (CFUs) mL^{-1}. The fluorescently labeled bacteria suspension was flowed through a PEGylated double spiral microfluidic device at 0.2 mL min^{-1} using an infusion syringe pump. Bacterial trajectories and focusing within the double spiral channel were visualized in real-time using fluorescence microscopy (EVOS FL, Invitrogen).

Susceptibility Testing

Colistin minimum inhibitory concentrations (MIC) of bacterial strains were confirmed by standard agar dilution methods[152]. Results were interpreted according to the Clinical and Laboratory Standards Institute susceptibility breakpoints[153].

Bacterial capture visualization

A. baumannii ATCC17978 was labeled with SYTO®9 as previously described in the 'inertial focusing visualization' methods section. The fluorescently labeled bacteria suspension was flowed through the colistinated and PEGylated double spiral microfluidic devices at 0.2 mL min^{-1} using an infusion syringe pump. The devices were then washed four times with PBS, pH 7.4, to remove any weakly bound bacteria. Fluorescent images of the microchannels were obtained using fluorescence microscopy (EVOS FL, Invitrogen). This process was repeated using fluorescently labeled *A. baumannii* ATCC17978 and *S. aureus* ATCC29213 spiked into EDTA-anticoagulated, whole human blood. Human blood was obtained from healthy donors with informed consent in accordance with the Vanderbilt University Human Subjects Institutional Review Board (IRB) (protocol number 111251).

Bacterial capture quantification

Testing of the pathogen-capture capacity of the colistinated and PEGylated double spiral microfluidic devices were carried out by first adjusting an *A. baumannii* ATCC17978 bacterial suspension to ~8 X 10^7 CFUs mL^{-1} in PBS, pH 7.4. A concentration of ~10^2 CFUs mL^{-1} was obtained by serial dilution of the initial suspension, which served as the control. Bacterial samples were infused through the colistinated double spiral microfluidic device at 0.2 ml min^{-1}, and samples were collected from the device outlet at 5 different time points (1, 2, 3, 4 and 5 minutes). This process was also repeated for the PEGylated double spiral microfluidic device. The recovered solutions from the outlet of the double spiral microfluidic devices were diluted in the same fashion as the control group. The collected samples and control were plated on LB-agar Petri dishes in triplicate (100 µL) for quantitating pathogen-capture capacity. Plates were incubated at 37 °C for 24 h, and colonies formed on the Petri dishes were counted. The number of the initial and recovered bacteria were calculated by multiplying the average number of colonies counted from the replicates by their respective dilution factor. The number of captured bacteria was determined by subtracting the number of recovered bacteria from the initial amount of bacteria (i.e. untreated control group). The capture capacity was calculated by dividing the number of captured cells by the number of initial cells. Capture capacity of the following bacterial strains in PBS, pH 7.4 was quantified: *A. baumannii* ATCC17978, colistin-resistant *A. baumannii* 19606R, colistin-resistant *A. baumannii* 'Patient 2', *K. pneumoniae* ATCC700603, and *B. subtilis* 1A578. This process was also repeated for *A. baumannii* ATCC17978 spiked into EDTA-anticoagulated, whole human blood.

Endotoxin binding assay

The Pierce LAL Chromogenic Endotoxin Quantification kit (Thermo Scientific, Lot # RG236327) was used according to the manufacturer's protocol to quantify the endotoxin capture capacity of the colistinated and PEGylated double spiral microfluidic devices, respectively. Briefly, *Escherichia coli* (*E. coli*) Endotoxin Standard (011:B4) was reconstituted in endotoxin-free water at a concentration of 1 EU mL^{-1} (Endotoxin Unit) and the solution was flowed through the colistinated double spiral microfluidic device at 0.2 ml min^{-1} using an infusion syringe pump. Samples were collected from the device outlet at 5 different time points (1, 2, 3, 4 and 5 minutes). This process was repeated for the PEGylated double spiral fluidic device. Collected samples were then analyzed for endotoxin concentration according to the manufacturer's protocol, and results were read at 450 nm.

Hematology studies

To determine whether treatment with the double spiral microfluidic device significantly changes blood hematologic parameters, 1 mL of EDTA-anticoagulated whole, human blood was collected from the colistinated device outlet after being flowed through the blood-cleansing device at 0.2 ml min^{-1}. This process was repeated for the PEGylated device. Red blood cell lysis was then analyzed to determine release of free hemoglobin in plasma. Plasma hemoglobin was measured by according to well-established protocols[57]. Following passage through the device, the blood samples were centrifuged (500 x g) and the supernatant was spectrophotometrically analyzed for hemoglobin release using a plate-reader (Tecan, Infinite M1000 Pro) at 451 nm in order to determine percent hemolysis relative to the Triton-X positive control. Triton X-100 (Sigma-Aldrich) was diluted in diH_2O to result in a 20 v/v % Triton-X detergent concentration, which served as the positive control. The negative control used was EDTA-anticoagulated whole, human blood that was not flowed through a double spiral microfluidic device (i.e. untreated). Percent of hemoglobin release was calculated according to the following equation: Hemoglobin release (%) = [(Sample$_{451nm}$ – Negative control$_{451nm}$)/(Positive control$_{451nm}$ – Negative control$_{451nm}$)] X 100%. Complete blood counts of each sample (i.e. untreated, colistinated device, PEGylated device) were performed by the Vanderbilt University Translational Pathology Shared Resource Core.

Device scale-up

A larger version of the initial double spiral microfluidic device was fabricated and functionalized using the previously described methods. The scaled-up version of the device consisted of a 4-loop double spiral microchannel with one inlet and one outlet. Dimensions of the scaled-up version were 323 mm *L*, 750 μm *W*, and 15 μm *H*. The spacing between two adjacent loops was 500 μm and the radius of the outermost curvature was 11.2 mm. The dimensions of the scaled-up device were adjusted such that the volume:surface area ratio was comparable to that of the initial device design. The bacterial capture capacity of the scaled-up device was characterized to compare the capture capacity to that of the smaller device. The ‘bacterial capture quantification’ assay using the scaled-up device was performed with *A. baumannii* ATCC17978.

Statistical analysis

All measured values are reported as an average mean of at least triplicate samples ± standard deviation (SD), as indicated by error bars. Significant differences were determined using a one-way ANOVA followed by *post hoc* Tukey’s multiple comparison test, as defined by *P* values < 0.01.

Results and Discussion

Colistin conjugation to microchannel walls

Fluorescent labeling and stoichiometric analysis were used to estimate that 1.76 μg of colistin was functionalized along the walls of the colistinated double spiral device (Appendix B Fig B2). The amount of colistin associated with the surface of this device is non-toxic to humans[59,68,73].

An ELISA was performed to estimate the amount of colistin-containing molecules that were released from the double spiral microfluidic device. Continuous flow for 2 hours resulted in approximately 300 ng of colistin release from the channel (Appendix B Fig B3).

Inertial particle focusing in the double spiral microfluidic device

Fluorescent polystyrene microparticles under continuous flow conditions were imaged within the non-functionalized double spiral microfluidic channel. At a volumetric flow rate of 0.2 ml min^{-1}, with corresponding $Re = 14.9$, 2 μm sized particles were focused near the inner wall of the microchannel (Fig 4.3a), while 10.2 μm size particles were focused near the center of the microchannel width (Fig 4.3b). The composite fluorescence images show the trajectories of the 10.2 μm (red stream) and 2 μm particles (green stream), with the larger particles approximating the trajectory of larger blood cells (i.e. red blood cells and white blood cells). Microparticles are inertially focused at equilibrium positions as a function of diameter. A clear separation of bacterial-sized particles from blood cell-sized particles is evident. *A. baumannii* ATCC17978 are inertially focused even closer to the channel wall than 2 μm diameter spherical particles. In addition, bacteria appear near both lateral surfaces of the double spiral device. These behaviors are in agreement with the inertial design as derived from net inertial lift force (F_L) and Dean drag force (F_D).

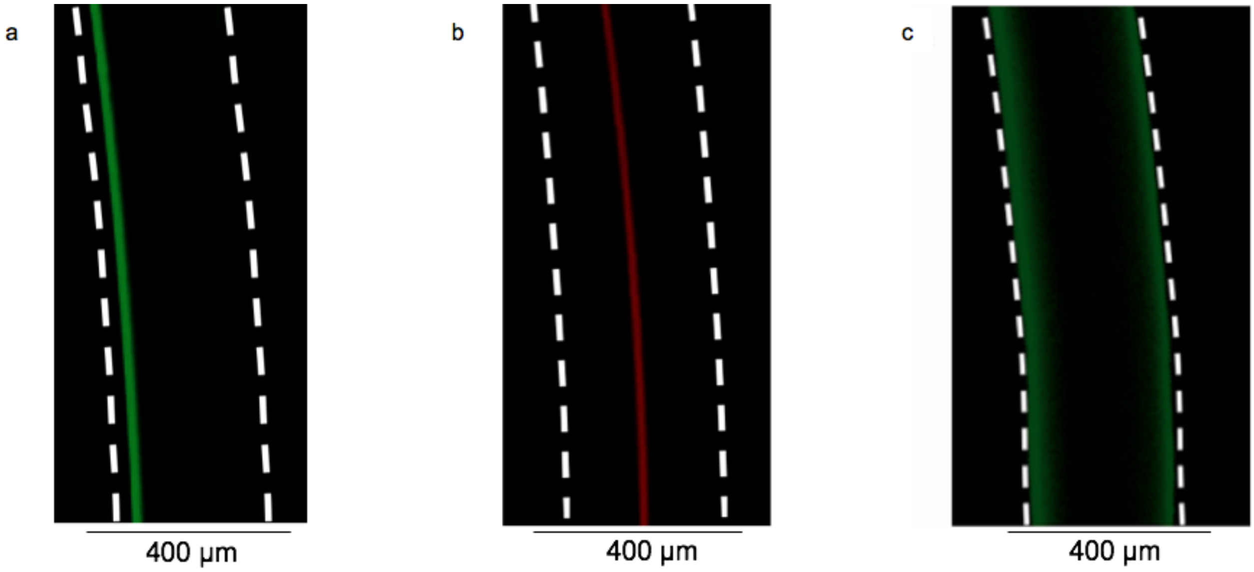

Figure 4.3. Microparticle and bacterial focusing within double spiral microchannel. Images were acquired within the double spiral microchannel at a continuous flow rate of 0.2 mL min^{-1}. **a**, Focusing of 2 μm particles (green) within the double spiral microchannel. **b**, Focusing of 10 μm particles (red) within the double spiral microchannel. **c**, Labeled *A. baumannii* ATCC17978 (green) focusing along the inner and outer walls of the double spiral microfluidic device c, Labeled *A. baumannii* ATCC17978 (green) focusing along the inner and outer walls of the double spiral microfluidic device.

Bacterial cell capture using surface-modified double spiral microfluidic device

A. baumannii ATCC17978 bacterial cells were chosen as the standard specimen for qualitatively and quantitatively evaluating the bacterial capture capacity of the colistinated and PEGylated double spiral microfluidic devices. Green, fluorescently labeled *A. baumannii* ATCC17978 are bound to the colistinated microchannel walls following passage through the microfluidic device at 0.2 mL min^{-1} and subsequent washing (Fig 4.4a and 4.4b**)**. However, significant bacterial capture did not occur within the PEGylated double spiral microfluidic device, presumably due to the absence of colistin surface functionalization (Fig 4.4c**)**.

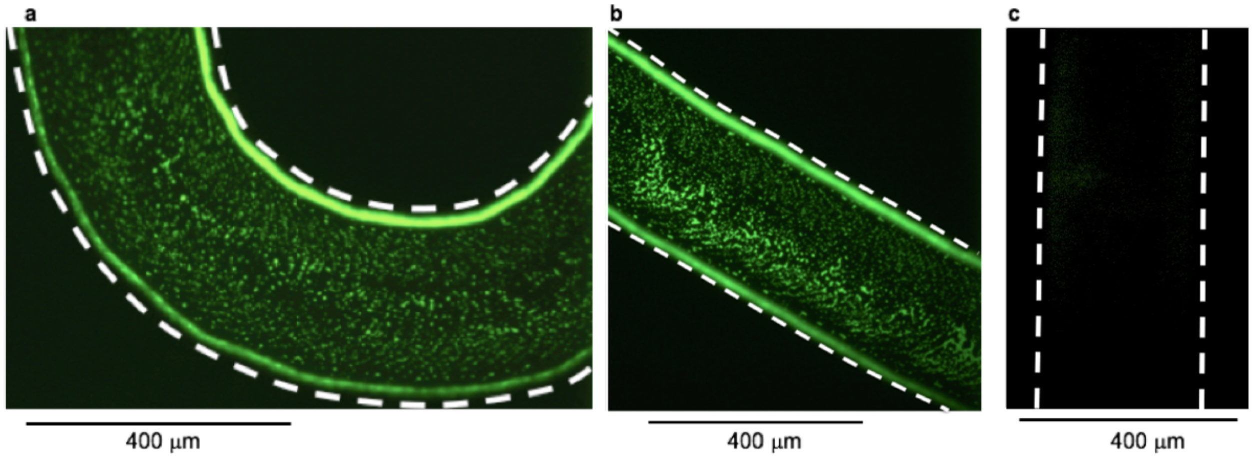

Figure 4.4. Fluorescently labeled bacteria captured along colistinated microchannel walls. **a & b**, Fluorescent images displaying *A. baumannii* ATCC17978 (green) captured within colistinated microfluidic device following washing. **c**, Fluorescent image displaying the lack of *A. baumannii* ATCC17978 capture within the PEGylated microfluidic device following washing.

Bacterial capture capacity was quantified by flowing 1 mL of *A. baumannii* ATCC17978 suspension in PBS, pH 7.4, through the microfluidic devices at a flow rate of 0.2 mL min^{-1}. A bacterial cell capture capacity of over 10^7 CFUs was achieved with a single passage through the colistinated double spiral microfluidic device (Fig 4.5a), as confirmed by the reduction of colonies that could be cultured from the fluid exiting the device. *K. pneumoniae* ATCC700603, another Gram-negative human pathogen, was also successfully removed from flowing fluid (Fig 4.5b). The colistinated double spiral microfluidic device also captured and removed antibiotic-resistant organisms, including colistin-resistant *A. baumannii* 'Patient 2'[149] and colistin-resistant *A. baumannii* 19606R[58], from flowing fluid (Fig 4.5c and 4.5d). These colistin-resistant strains are well characterized in literature and colistin-resistance was reconfirmed through MIC assessment (Appendix B Table B1). Binding of green fluorescent *A. baumannii* ATCC17978 to the colistinated double spiral microchannel device was strongly supported by PEG functionalization (Fig 4.5a – 4.5d). Colistinated and PEGylated devices did not capture Gram-positive *B. subtilis* 1A578, confirming specificity for Gram-negative pathogens in colistin-functionalized devices (Appendix B Fig B4).

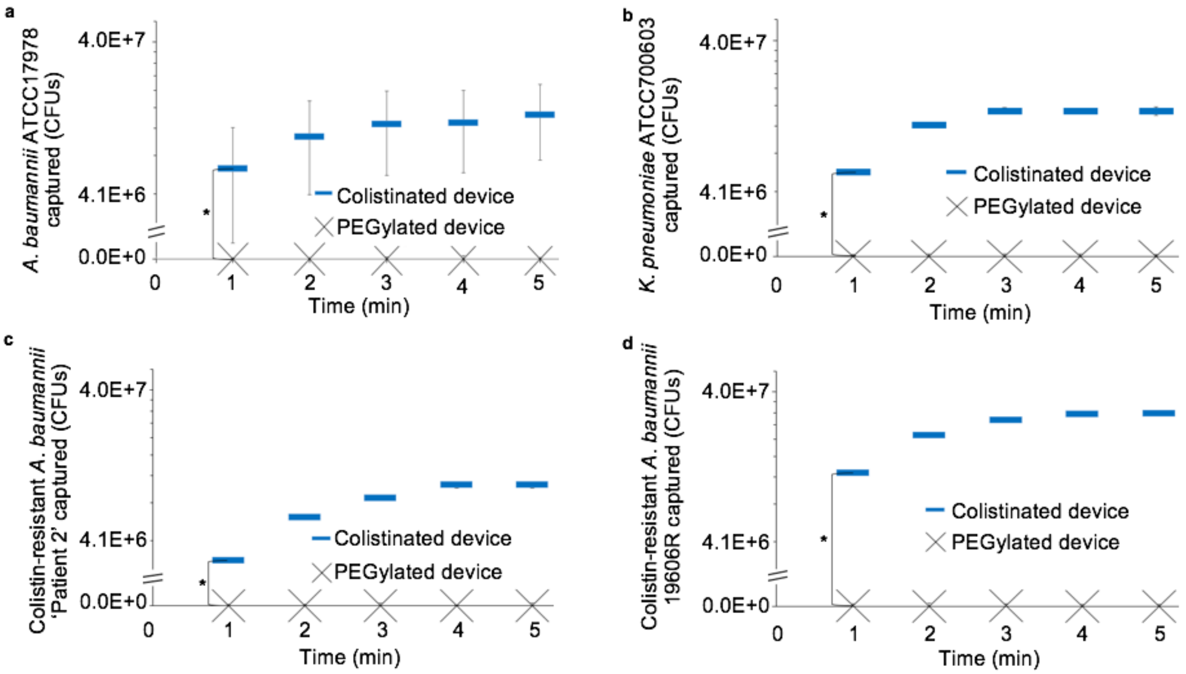

Figure 4.5. Quantification of bacterial capture capacity. Pathogen capture capacity of Gram-negative bacterial isolates when spiked into PBS and flowed through the colistinated and PEGylated double spiral microfluidic devices at 0.2 ml min^{-1}. **a**, *A. baumannii* ATCC17978. **b**, *K. pneumoniae* ATCC700603. **c**, Colistin-resistant *A. baumannii* ‘Patient 2’. **d**, Colistin-resistant *A. baumannii* 19606R. Results are plotted as the mean ± SD, $n = 3$. $*P < 0.01$.

Extracorporeal blood cleansing

The blood-cleansing capability of the double spiral microfluidic device was assessed using fresh, whole human blood that was EDTA-anticoagulated and experimentally contaminated with *A. baumannii* ATCC17978. A single colistinated double spiral microfluidic device removed approximately 10^7 colony forming units of bacteria from whole blood with one pass through the device at a flow rate of 0.2 ml min^{-1} (Fig 4.6a). Bacterial cell capture from flowing blood was also confirmed using fluorescence microscopy. Green, fluorescently labeled *A. baumannii* ATCC17978 is bound to the colistinated microchannel walls following passage of infected blood through the microfluidic device at 0.2 mL min^{-1} and subsequent washing (Fig 4.6b and 4.6c**)**. Gram-positive *S. aureus* ATCC29213 spiked in whole, human blood, however, did not bind to the colistinated microchannel walls, confirming specificity for Gram-negative pathogens in the colistin-functionalized devices (Fig 4.6d). Flowing whole, human blood through the colistinated and PEGylated double spiral microfluidic devices had no detectable effect on blood composition (Appendix B Table B2), nor did it induce red blood cell hemolysis (Appendix B Table B3).

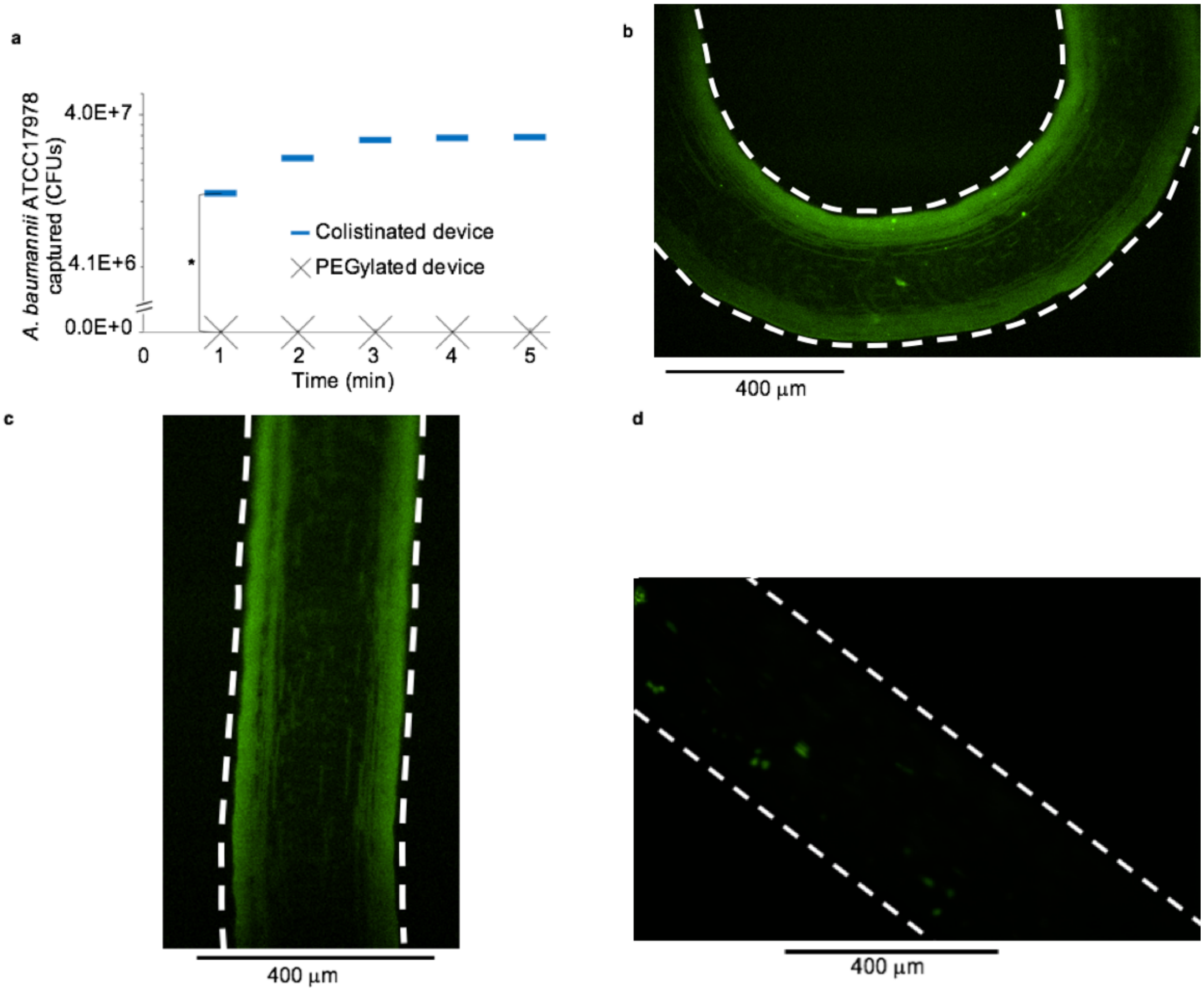

Figure 4.6. *Ex vivo* blood cleansing using the double spiral microfluidic device. **a**, Capture capacity for *A. baumannii* ATCC17978 when spiked into whole, human blood and flowed through the colistinated and PEGylated double spiral microfluidic devices at 0.2 ml min^{-1}. Results are plotted as the mean ± SD, $n = 3$. $^*P < 0.01$. **b & c**, Green fluorescently labeled *A. baumannii* ATCC17978 capture from whole, human blood following passage through colistinated double spiral microchannel at 0.2 mL min^{-1} and subsequent washing. **d**, Lack of green fluorescently labeled *S. aureus* ATCC29213 capture following passage through a colistinated double spiral microchannel at 0.2 mL min^{-1}, confirming specificity for Gram-negative pathogens in the colistin-functionalized devices.

Total bacterial capture capacity

The colistinated double spiral microfluidic device removed ~10^7 CFUs of live *A. baumannii* ATCC17978 (Fig 4.5a) and a similar quantity of *K. pneumoniae* ATCC700603 (Fig 4.5b) from PBS within 5 minutes of device operation. In addition, colistin-resistant strains of *A. baumannii* (i.e. *A. baumannii* 19606R and *A. baumannii* ‘Patient 2’) were captured with equal efficacy as the wild-type, colistin sensitive *A. baumannii* strain (Fig 4.7). Statistical analysis confirmed that the colistinated double spiral microfluidic device captured Gram-negative bacteria from whole, human blood at a capacity that is not significantly different than in PBS (Fig 4.7).

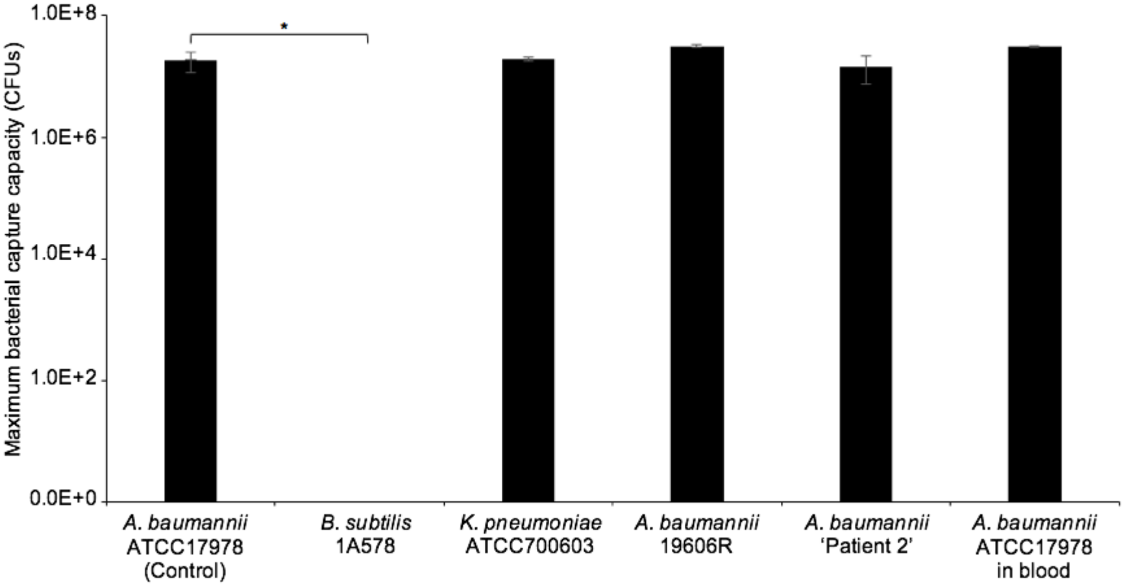

Figure 4.7. Total bacterial capture capacity of colistinated double spiral microfluidic device. The maximum bacterial load that a single colistinated double spiral fluidic device can capture is reported with respect to each bacterial strain indicated. *A. baumannii* ATCC17978 spiked in PBS served as the control. Capture of *A. baumannii* ATCC17978 was significantly different than the capture of *B. subtilis* 1A578. However, the capture of *A. baumannii* ATCC17978 was not significantly different than any other bacterial isolate listed. The maximum capture capacities of all other bacterial isolates listed (*K. pneumoniae* ATCC700603, *A. baumannii* 19606R, *A. baumannii* 'Patient 2', and *A. baumannii* ATCC17978 in blood) were also significantly different that of *B. subtilis* 1A578. Data were compared using one-way ANOVA followed by *post hoc* Tukey's multiple comparison test. Results are plotted as mean ± SD, $n = 3$. $^{*}P < 0.01$.

Quantification of endotoxin capture

Endotoxin, one of the principal components of the outer membrane of Gram-negative bacteria, also contributes to the systemic inflammatory response that is characteristic of sepsis[154]. Therefore, the removal of endotoxin from flowing fluid using the double spiral microfluidic device was assessed. Endotoxin was spiked into endotoxin-free water and continuously flowed through the device at 0.2 mL min^{-1} for 5 minutes, totaling 1 mL. Endotoxin was rapidly captured from the fluid passing through the colistinated double spiral microfluidic device, with endotoxin capture efficiency approaching 100% in single pass operation (Appendix B Fig B5). In contrast, endotoxin was not effectively captured using the PEGylated device, demonstrating the critical requirement for colistin in endotoxin retention in the double spiral.

Device scale-up for clinical translation

The capture capacity of the described colistinated double spiral microfluidic device is approximately 10^7 CFUs (Fig 4.7), which exceeds the requirements to treat a septic patient by more than two orders of magnitude[118–120]. However, for potential clinical translation, the flow rate associated with the current device design must be increased to enable treatment of larger animal models and humans. Therefore, a larger version of the double spiral fluidic design was developed to demonstrate the feasibility of scaling up the current design. The scaled-up version of the colistinated double spiral microfluidic device, operating at a flow rate three times greater than that used with the initial design, captured of over 10^7 *A. baumannii* ATTC17978 CFUs in single pass operation (Fig 4.8). Dimensions of the scaled-up device were selected to provide a volume to surface area ratio similar to that of the original device, while maintaining appropriate hydrodynamic particle focusing characteristics. The governing principles of fluid transport in closed conduits can be used to design a larger double spiral device with performance characteristics appropriate for increased treatment volumes.

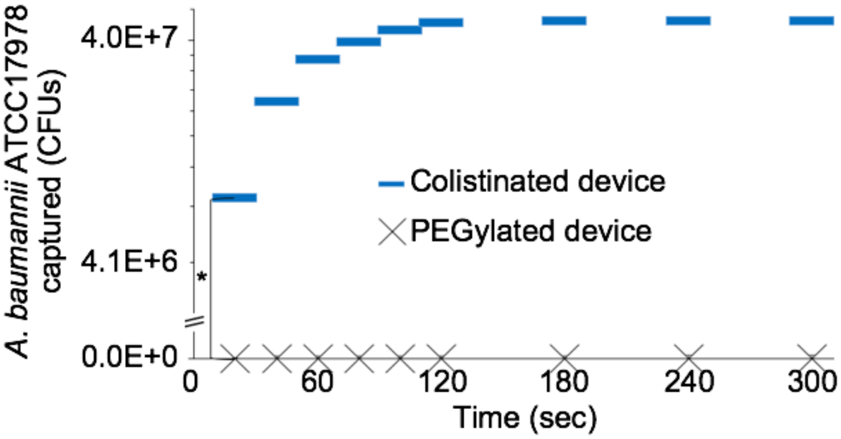

Figure 4.8. Bacterial capture capacity of larger double spiral microfluidic device. *A. baumannii* ATCC17978 spiked into PBS was flowed through larger colistinated and PEGylated double spiral microfluidic devices (328 mm *L* X 750 μm *W* X 15 μm *H*) at 0.6 mL min^{-1}. The *A. baumannii* ATCC17978 capture capacity of the microfluidic device was quantified over the time indicated. Results are plotted as the mean ± SD, *n* = 3. **P* < 0.01.

Asymmetric spiral-based microfluidic devices have previously been designed to achieve equilibration of large (>10 μm) microparticles[31,135,155]. This work is the first to successfully demonstrate the equilibration of 2 μm sized particles under continuous flow conditions within a double spiral microchannel. Figure 4.3a and 4.3b demonstrate that 2 μm particles ($a_p/H \sim 0.13$; $F_L > F_D$) and 10.2 μm particles ($a_p/H \sim 0.67$; $F_L > F_D$) are more influenced by inertial lift forces rather than Dean force, and thus equilibrate within the microchannel. These results are in agreement with the work by Kuntaegowdanahalli and Bhagat, validating that particles that satisfy $a_p/H \geq 0.07$ are able to focus and occupy a single equilibrium position within a microchannel [31,155]. The low aspect ratio of the channel design is believed to promote the focusing of smaller particles near the inner channel wall[32]. The larger 10 μm sized particles equilibrate near the center of the channel due to the larger wall-induced lift force experienced, in comparison to 2 μm particles[32,142,156].

Focusing positions of non-spherical particles are dependent on the particle's largest cross-sectional dimension[157,158]. *A. baumannii* ATCC17978, a rod-shaped (coccobacillus) bacterium, is typically 2 μm in length and 0.5 μm in width[73]. Hence, 2 μm particle focusing was evaluated (Fig 4.3a). However, non-spherical bacterial cells can freely rotate and experience strong rotational-induced lift forces while being inertially focused and sorted. At Reynolds numbers greater than 10, both spherical and rod-shaped particles generally follow the same focusing trend[159]. However, in microchannels with a low aspect ratio, such as the case with this design, rod-shaped particles focus to two equilibrium regions, one along the inner microchannel wall and the other along the outer microchannel wall[160], as experimentally confirmed (Fig 4.3c). Bacteria oscillate when close to the channel wall due to the rotational forces imposed on the rod-shaped particles[161]. Near-wall focusing combined with rotation inducing lift forces presumably allow for direct contact of bacteria with both the inner and outer colistin functionalized microchannel walls.

The requirement for colistin functionalization suggests that wild-type *A. baumannii* capture is mediated by colistin (Fig 4.4, Fig 4.5a and 4.5b). The colistin-dependent capture of two independently isolated *A. baumannii* strains that are strongly colistin resistant implies a previously unrecognized approach for the capture and removal of antibiotic-resistant bacteria (Fig 4.5c and 4.5d). This result is consistent with colistin-resistance as independent of colistin binding to the bacterial outer membrane. These colistin-resistant strains have increased expression of many genes involved in cell envelope and membrane biogenesis[58]. The inability of colistin functionalized double spiral devices to capture Gram-positive bacteria, such as *B. subtilis* 1A578, further supports the capture mechanism as colistin recognition since Gram-positive bacteria are insensitive to, and unable to bind, colistin.

Robust bacterial capture from blood is essentially identical to that for blood cell-free bacterial suspensions *in vitro* (Fig 4.6 and 4.7). The design of the double spiral spatially isolates the formed elements of the blood from the regions where bacterial binding occurs and is hypothesized to be responsible for bacterial capture efficiency that is not reduced in the presence of blood cells. The simplicity and robustness of this design supports the translational potential of the approach.

Use as a treatment modality in sepsis demands both increased flow capacity to accommodate the blood volume of larger living systems and a way to isolate Gram-positive bacteria. We demonstrate here the potential for scale-up using the same quantitative approach and design principles applied to the original device (Fig 4.8). *A. baumannii* capture occurs with equal effectiveness after increasing the cross-sectional area of the fluidic device while holding the volume to surface area ratio constant. Importantly, this proof of concept is easily expandable to include devices possessing capture agents for Gram-positive bacteria[134]. Combination devices will, presumably, offer the capability to remove bacteria regardless of presentation as Gram-positive, Gram-negative, or antibiotic resistant, thus enabling early treatment in the absence of positive bacterial culture or strain identification from a blood sample. Furthermore, the removal of bacteria and endotoxin offers a greatly needed, new approach for the treatment of sepsis.

Conclusions

This work describes a double spiral microfluidic device, which can separate and capture *A. baumannii* from whole blood continuously with a maximum bacterial capture capacity of approximately 10^7 CFUs. Compared to current sepsis therapies, such as antibiotic administration or immunomodulatory therapies, the double spiral fluidic platform has distinct advantages, including avoidance of clogging through size-based cell separation, an effective capture capacity, and removal of multi-drug resistant infections. This is the first device optimized specifically for size-based separation of bacteria from blood. The fluidic platform also eliminates the need for complex external force fields, making the device easy to fabricate and implement. Mechanically removing bacteria and endotoxins breaks the current paradigm of sepsis therapy that is focused on applying antibiotics following bacterial culture and identification. Continued development of this technology will enable use as an adjuvant sepsis therapy and provide a more streamlined path to clinical translation.

Summary

Removal of bacteria and endotoxin from blood could potentially be a valuable adjunct to antibiotics for the treatment of sepsis. However, the separation of pathogens from blood is generally challenging, since non-spherical bacterial cells and endotoxins cannot be easily removed by common filtration methods, such as pore-based hemoperfusion filters, without significant complication. We demonstrate that an inertial-based microfluidic device conjugated with a bacterial- and endotoxin-targeting ligand exhibits significant blood cleansing capabilities. The device described herein eliminates pathogens, including multi-drug resistant strains, from whole, human blood. The bacterial load captured by the compact, inertial-based microfluidic device exceeds the maximal bacterial load in septic patients by more than two orders of magnitude. These results provide the first proof-of-principle that extracorporeal extraction of pathogens and endotoxins using inertial-based fluidics may be used as a next-generation purification technology to reduce sepsis-associated morbidity and mortality. **This work successfully fulfills Specific Aim 3 of this dissertation.**

CHAPTER V

SYNOPSIS AND CONCLUSIONS

The goal of my dissertation work was to develop a transformative fluidic platform for removal of *Acinetobacter baumannii*, a leading cause of sepsis worldwide, from flowing fluids. In order to develop this fluidic platform, I overcame a number of hurdles. Initially, I planned to use magnetic nanoparticles for the capture and removal of *A. baumannii* from fluid. However, through computational modeling I discovered that this approach presented many complications due to the magnetophoretic separation limitations imposed by magnetic nanoparticle-pathogen complexes. Nevertheless, I was able to develop a colistin functionalized nanoparticle that allowed for binding of *A. baumannii* in a saline solution. This work demonstrated that colistin could be used as an *A. baumannii*-targeting motif. Based on this knowledge, I proceeded to develop a colistin functionalized fluidic platform for the separation and capture of *A. baumannii* from flowing fluids. The design of the colistin functionalized fluidic platform was informed by my previously developed computational model of sepsis progression.

As outlined in the chapters of this dissertation, I began by developing a novel colistin functionalized nanoparticle for the rapid capture of *A. baumannii* (Chapter II). My work detailed in Chapter II was published in the *Journal of Biomedical Nanotechnology*[73]. I demonstrated for the first time the power of incorporating colistin-modified nanoparticles for capture of multiple Gram-negative bacterial strains, including drug resistant variants. The ability to control the surface coverage of colistin functionalized nanoparticles played an important role in efficient capture of the bacteria. I also discovered that extending the colistin probe from the surface of the nanoparticles with a polyethylene glycol spacer provided greater ligand flexibility, presumably allowing the colistin ligand to adopt orientations more amenable to effective interactions with the targeted pathogen surface. Importantly, the time required for pathogen capture was significantly less than nanoparticle-pathogen capture times found in previously published literature. I demonstrated that colistin enabled nanoparticle complexation with *A. baumannii* rapidly, reaching half-maximum saturation in approximately 7 minutes. This rate of capture is significantly faster than the most advanced nanoparticle-pathogen extraction platforms reported to date[26,134]. These results demonstrate that colistin is an excellent molecular probe for use in bacterial capture assays, where the stability, reaction conditions, and control of ligand orientation are more flexible than those for typical antibody-based strategies. I also demonstrated that a single colistin functionalized nanoparticle can be used to target and isolate a variety of Gram-negative pathogens, including colistin-resistant variants. Thereby, negating the requirement of pathogen identification prior to isolation and removing the need of nanoparticles that target a specific bacteria strain or variant.

Following the development of a colistin-based bacterial targeting ligand, I developed a computational model to assess the bacterial extraction characteristics required for effective eradication of infection (Chapter III). My work detailed in Chapter III was published in *PLOS ONE*[27]. The engineering-based mathematical model that I developed was used to quantitatively describe the kinetics of pathogenesis and progression of sepsis under various conditions, including bacterial separation therapy, to better understand disease mechanisms and quantitatively assess the biological impact of bacterial separation therapy. I discovered from this model that mechanical bacterial separation from blood has the potential to reduce the time of total bacteria clearance from the blood of an immunocompromised subject by 49%, compared to antibiotic treatment alone. The time required for bacteria clearance from the lungs, spleen, and liver were also significantly reduced using extracorporeal bacterial separation, thereby reducing total sepsis duration. This was a significant finding because duration of sepsis is directly correlated to patient outcome. Therefore, this work established the potential effectiveness of engineering-based bacterial separation devices for the treatment of sepsis through effective pathogen eradication. The engineering-based model described in Chapter III enabled quantitative identification of the characteristics required of an extracorporeal bacteria separation device to provide biological benefit.

Using the modeled described in Chapter III, I also evaluated nanoparticle-bacteria capture processes in blood by introducing empirical constants that mimic the interfering effects of biological components, which lower complexation efficacy of bacteria-nanoparticles. Nanoparticles with 25 nm radii were mathematically predicted to exhibit maximum capture of bacteria in blood due to their high mobility and large surface area to volume ratio, as compared to larger nanoparticles. These results were validated by previously published experimental data[26]. Unfortunately, nanoparticles of approximately 25 nm radii do not possess the magnetophoretic properties required to be extracted from flowing fluids even by the most advanced magnetic separation systems. Larger magnetic nanoparticles (> 500 nm radius) can be magnetically separated from flowing fluids effectively, but these larger particles do not meet the mobility and surface area to volume ratio requirements that enable rapid pathogen complexation and subsequent extraction from blood. Therefore, at this stage in my work I moved towards developing a colistin functionalized bacterial separation platform that did not utilize magnetic nanoparticles due to inherit magnetophoresis-associated downfalls. This subset of my work highlights the need for implementation of engineering-based principals for the elucidation of disease progression, specifically sepsis, to better develop treatment modalities.

Chapter IV described my development of a mathematical model-based, colistin functionalized fluidic platform for *A. baumannii* capture and removal from fluids (Chapter IV). This subset of my work will be submitted for publication during February of 2017. Chapter IV successfully demonstrated for the first time that a novel double spiral fluidic device can be designed for separation and capture of *A. baumannii* and other bacterial cells. Hydrodynamic, size-based separation principles characteristic of spiral fluidics were used to inertially focus bacteria into equilibrium positions within the fluidic device, which has never been previously accomplished. In addition, the fluidic device was functionalized with a bacterial- and endotoxin-targeting colistin ligand in a way that allowed for capture of the inertially focused targets. This work successfully demonstrated the capture of Gram-negative pathogens and endotoxin using the colistin functionalized fluidic platform. The design of the double spiral spatially isolated the formed elements of the blood from the regions where bacterial binding occurs and is hypothesized to be responsible for bacterial capture efficiency that is not reduced in the presence of blood. The bacterial load captured by the compact, inertial-based microfluidic device exceeded the maximal bacterial load in septic patients by more than two orders of magnitude. The design parameters of the fluidic device enabling rapid and effective bacterial capture were informed by the previously described mathematical model of sepsis (Chapter III), highlighting the need for application of engineering-based models to better assess disease progression and treatment. The simplicity and robustness of this design supports the translational potential of the approach. This approach breaks the paradigm of current sepsis treatment protocols by rapidly eliminating the infectious agents, including multi-drug resistant variants, that lead to sepsis and sepsis progression – rather than applying non-specific and/or ineffective systemic antibiotic treatment.

More work must be done to continue the development of this promising technology. Next steps include: (1) further development of the fluidic platform for inertial focusing and separation of pathogens from blood cells under flow conditions suitable for rodents and scalable for larger animal models, (2) functionalization of the device channel walls with ligands designed to capture Gram-positive bacteria, in addition to Gram-negative pathogens and endotoxin, (3) evaluation of the molecular, cellular and systemic consequences of bacterial and endotoxin removal from the circulation of septic animal models, and (4) further escalation of the technology for clinical translation.

The technology developed through this work has the potential to serve as a novel blood cleansing therapeutic for the treatment of human disease. Inertial-based fluidic platforms hold many advantages over membrane-based blood cleansing filter devices in terms of effectiveness and hemocompatibility. The scalable fluidic platform highlighted by this dissertation is capable of removing pathogens and endotoxins from circulating fluids, whereas competing technologies cannot. This design has the capacity to meet the current unmet need of sepsis while also bolstering inertial-based fluidic use and accelerating scientific advancement. This hemocompatible, blood purification technology has the potential to protect and preserve lives in the face of a number of growing health concerns, including the rise of sepsis and multi-drug resistant bacterial infections.

APPENDIX

A. CHAPTER III SUPPLEMENTARY MATERIAL

Compartment	***K. pneumoniae*** **((CFU/mL)*h)**
Lung (L)	1.39E+07
Spleen (S)	1.35E+07
Liver (H)	1.33E+08
Blood (B)	1.37E+05

Table A1. Bacterial burden experienced by immunocompromised *K. pneumoniae* rodent model administered antibiotic.

Compartment	Antibiotic Treatment (h)	100% Bacterial Separation Efficiency from Blood + Antibiotic Treatment (h)	% Decrease of Required Treatment Time with Bacterial Separation Implemented (%)
Lungs (L)	88 h	49 h	44%
Spleen (S)	86 h	48 h	44%
Liver (H)	106 h	67 h	37%
Blood (B)	61 h	32 h	48%

Table A2. 100% efficient bacterial separation accelerates *K. pneumoniae* clearance (≤1 CFU/mL) in immunocompromised rodent model.

Compartment	100% Bacterial Separation Efficiency + Antibiotic ((CFU/mL)*h)	Antibiotic Treatment Alone ((CFU/mL)*h)
Lungs (L)	3.89E+06	1.39E+07
Spleen (S)	7.19E+06	1.35E+07
Liver (H)	6.72E+07	1.33E+08
Blood (B)	2.08E+04	1.37E+05

Table A3. Bacteria separation in immunocompromised *K. pneumoniae* rodent model reduced bacterial burden experienced.

Compartment	**100% Bacterial Separation Efficiency from Blood + Antibiotic Treatment (h)**	**60% Bacterial Separation Efficiency from Blood + Antibiotic Treatment (h)**	**20% Bacterial Separation Efficiency from Blood + Antibiotic Treatment (h)**	**Antibiotic Treatment (h)**
Lungs (L)	49 h	59 h	88 h	88 h
Spleen (S)	48 h	58 h	86 h	86 h
Liver (H)	67 h	75 h	106 h	106 h
Blood (B)	32 h	39 h	61 h	61 h

Table A4. *K. pneumoniae* clearance (≤1 CFU/mL) in immunocompromised rodent model accelerated with improved bacterial separation efficiencies.

Compartment	100% Separation Efficiency + Antibiotic ((CFU/mL)*h)	60% Separation Efficiency + Antibiotic ((CFU/mL)*h)	20% Separation Efficiency + Antibiotic ((CFU/mL)*h)	Antibiotic Treatment Alone ((CFU/mL)*h)
Lungs (L)	3.89E+06	6.15E+06	1.39E+07	1.39E+07
Spleen (S)	7.19E+06	8.62E+06	1.35E+07	1.35E+07
Liver (H)	6.72E+07	8.20E+07	1.33E+08	1.33E+08
Blood (B)	2.08E+04	4.70E+04	1.36E+05	1.37E+05

Table A5. 60% or greater bacteria separation efficiencies reduced bacterial burden in *K. pneumoniae* immunocompromised rodent model.

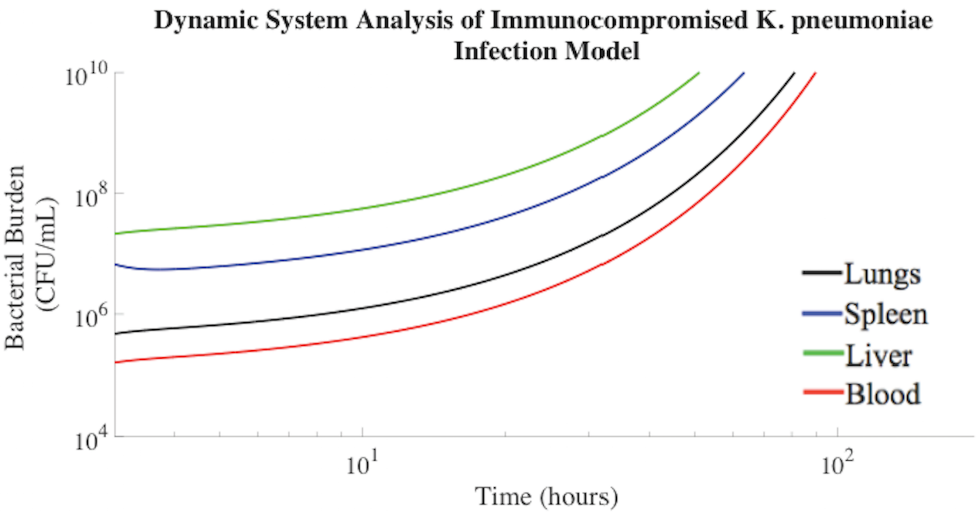

Figure A1. Bacterial burden increased over time in neutropenic rodents until reaching a lethal *K. pneumoniae* concentration. The median numbers of bacteria in each compartment observed experimentally in previous literature were used as the initial conditions for these simulations[98,101], and trajectories were generated using the parameter estimates described in the Materials and Methods of Chapter III.

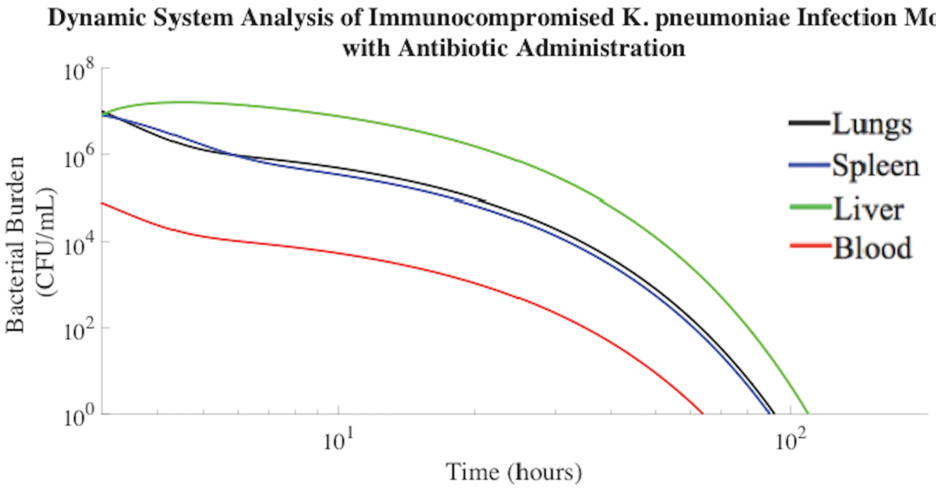

Figure A2. *K. pneumoniae* bacterial burden trajectories post inoculation in immunocompromised rodents treated with colistin sulfate (3 mg/kg).

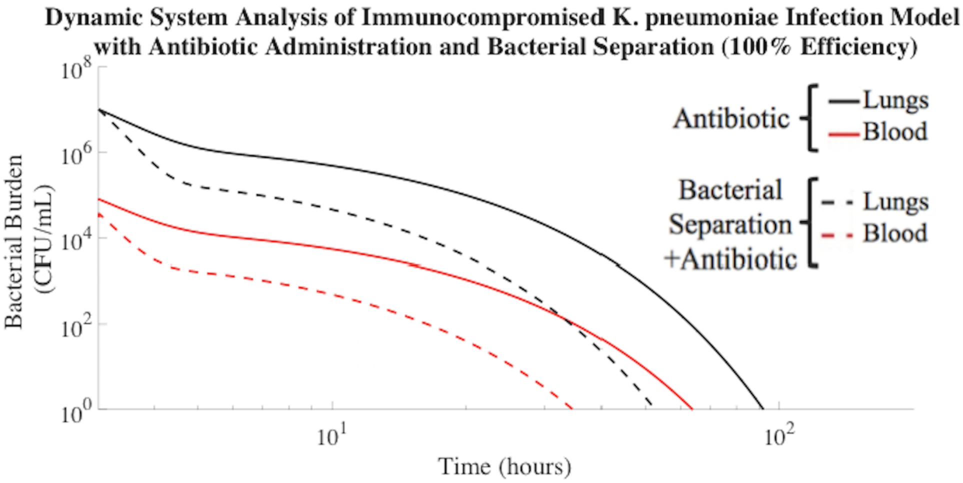

Figure A3. *K. pneumoniae* burden decreased more rapidly with bacterial separation treatment in combination with antibiotic. 100% bacterial separation efficiency, combined with antibiotic administration (colistin methanosulfate, 3mg/kg), resulted in bacterial clearance from the blood compartment in 32 h. This was 29 h faster than antibiotic treatment alone.

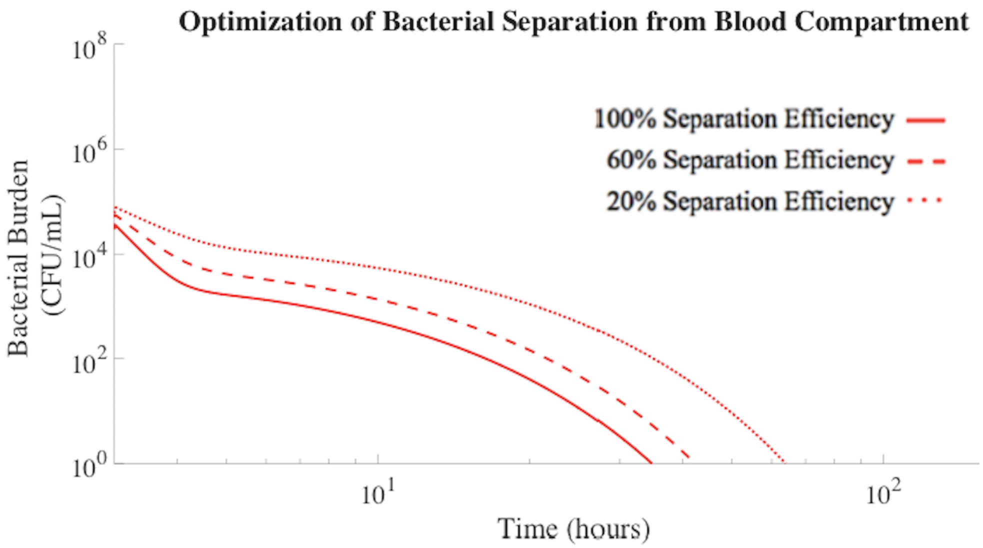

Figure A4. 100% and 60% bacterial separation efficiencies had a significant impact on overall bacterial clearance rates from the blood compartment of immunocompromised *K. pneumoniae* rodent model. 20% bacterial separation efficiency was not efficient enough to significantly impact the overall bacterial clearance rate and resulted in the same clearance rates as antibiotic treatment alone.

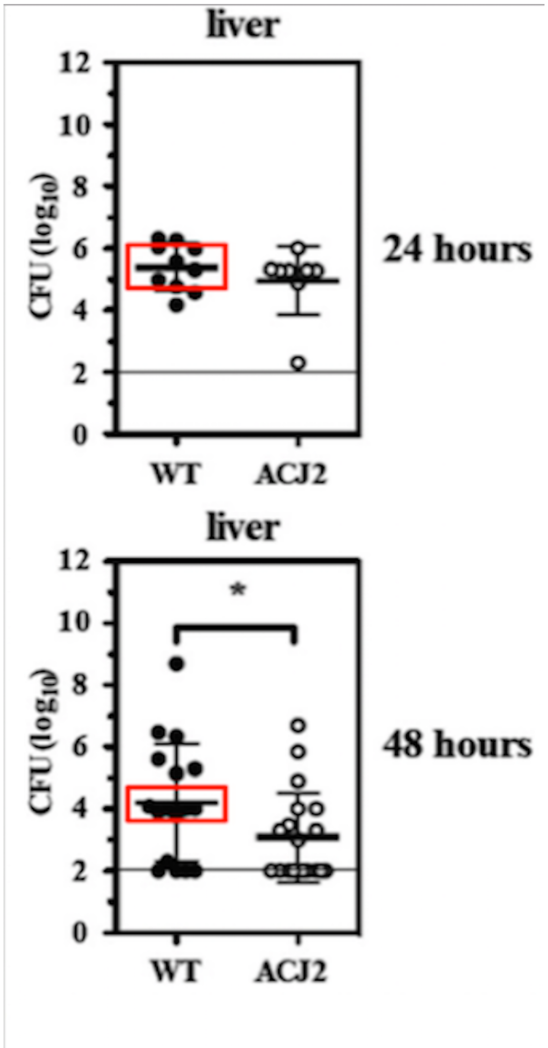

$$\frac{\Delta y}{\Delta x} = \frac{\Delta CFU}{\Delta hours} = \frac{5.7 - 4}{24 - 48} \approx \mathbf{-0.1}$$

Figure A5. Net bacterial growth rates estimated by linearization of experimental data. The net bacterial growth rate of *A. baumannii* in the liver of a non-immunocompromised rodent model is provided as an example calculation[96].

B. CHAPTER IV SUPPLEMENTARY MATERIAL

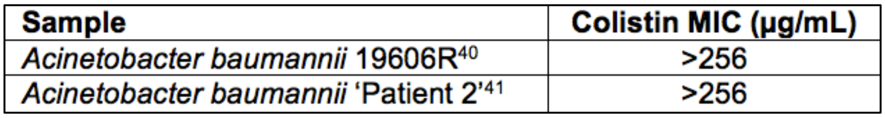

Sample	**Colistin MIC (µg/mL)**
Acinetobacter baumannii 19606R[40]	>256
Acinetobacter baumannii 'Patient 2'[41]	>256

Table B1. Colistin resistance. Minimum inhibitory concentrations (MICs; µg/ml) of colistin-resistant *A. baumannii* isolates. Results are listed as the mean ± SD, *n* = 3.

Sample	Red blood cells (trillion cells/L)	White blood cells (billion cells/L)	Platelet (billion cells/L)
Control	4.60 ± 0.70	6.80 ± 0.30	239 ± 26.6
Colistinated device	5.00 ± 0.10	7.30 ± 0.30	236 ± 0.90
PEGylated device	5.10 ± 0.10	6.50 ± 0.90	273 ± 84.3

Table B2. Blood cell counts of whole, human blood before and after passage through functionalized microfluidic devices. Red blood cell counts, white blood cell counts, and platelet counts of blood flowed through colistinated and PEGylated double spiral fluidic devices at 0.2 mL min^{-1} were not significantly different than the control group. Unaltered blood not passed through a microfluidic device was used as the control. Data were compared using one-way ANOVA followed by *post hoc* Tukey's multiple comparison test. Results are listed as the mean ± SD, $n = 3$. $^{*}P < 0.01$, $^{**}P < 0.001$, $^{***}P < 0.0001$.

Sample	Hemolysis (%)	Statistical Significance
Positive control (20 v/v % Triton-X)	100% ± 3.08%	***
Negative control	0.01% ± 0.70%	control
Colistinated device	1.09% ± 1.09%	n.d.
PEGylated device	1.86% ± 0.66%	n.d.

Table B3. Summary of hemolysis levels of whole, human blood flowed through functionalized microfluidic devices. Whole, human blood was flowed through the colistinated and PEGylated double spiral microfluidic devices. Blood passage through the devices did not cause hemolysis. Blood containing Triton-X (20 v/v %) was used as a positive control. The negative control was blood that was not passed through a double spiral fluidic device. Data were compared using one-way ANOVA followed by *post hoc* Tukey's multiple comparison test. Results are listed as the mean ± SD, $n = 5$. $^*P < 0.01$, $^{**}P < 0.001$, $^{***}P < 0.0001$.

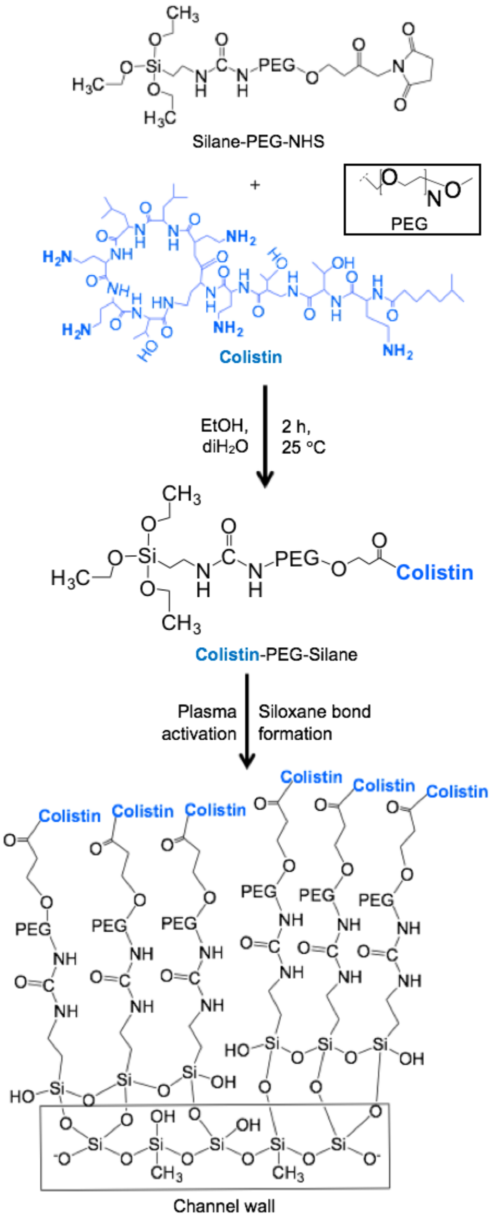

Figure B1. Schematic description of colistin immobilization onto the microchannel walls. NHS was used to couple Silane-PEG-NHS to one of the five similarly reactive L-α-diaminobutyric acid (Dab) residues of colistin through the amine side chain of Dab[59]. The NHS group of Silane-PEG-NHS covalently binds to any single, comparably reactive amine residue of the colistin antibiotic via carbodiimide chemistry, resulting in Colistin-PEG-Silane[60,61]. The silane end of Colistin-PEG-Silane forms siloxane bonds to the PDMS-based channel walls, resulting in colistin being extended into the lumen of the channel.

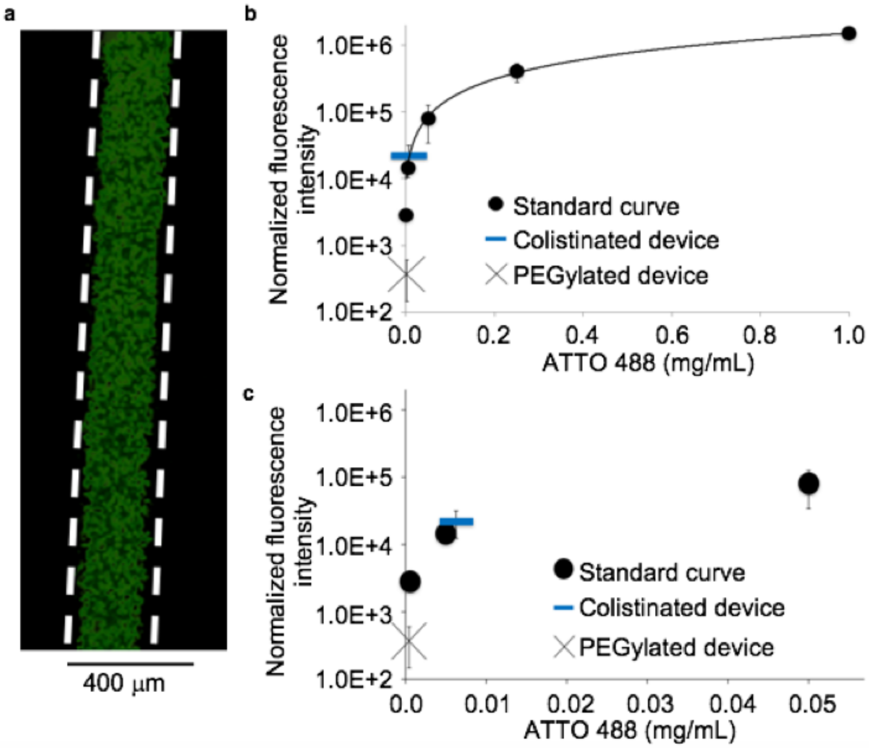

Figure B2. Confirmation of colistin decoration within microchannel. **a**, Fluorescent labeling of the amine groups of colistin was carried out with ATTO 488 NHS ester dye. The ATTO 488 NHS ester dye was added to a colistinated device and then washed with PBS. Staining indicates the presence of colistin within the microchannel. **b**, Standard dilutions of ATTO 488 NHS ester in DMSO were used to generate a standard fluorescence curve. **c**, Fluorescence generated from ATTO 488 NHS ester stained colistinated device and ATTO 488 NHS ester PEGylated device were compared to the standard curve. It was determined that 1.76 μg of colistin are present within the colistinated double spiral device. Results are plotted as the mean ± SD, *n* = 3.

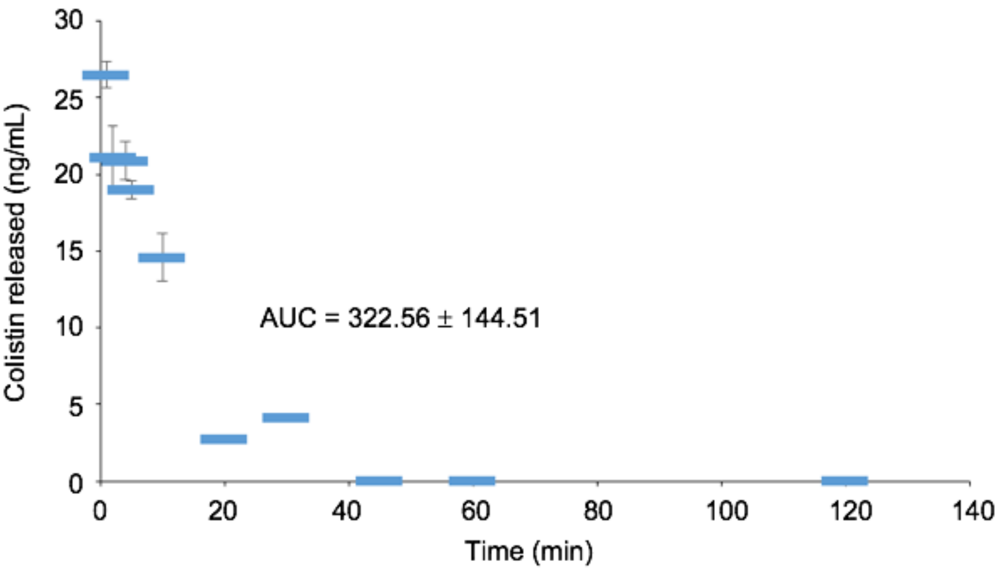

Figure B3. Colistin ligand retention within the double spiral microchannel. The release of colistin from the colistinated device was analyzed using a colistin ELISA (Bioo Scientific). PBS buffer was continuously flowed through a colistinated microfluidic device at 0.2 mL min^{-1}. The fluid was captured from the outlet at the time points indicated to analyze the possible detachment of colistin from the channel walls. Under continuous flow, 300 ng of colistin were released from the channel over the course of 2 hours. These levels of colistin are non-toxic. Importantly, no colistin was detectable in the outlet flow after approximately 40 minutes, making feasible a wash to remove uncoupled colistin from the device before use. Results are plotted as the mean ± SD, *n* = 3.

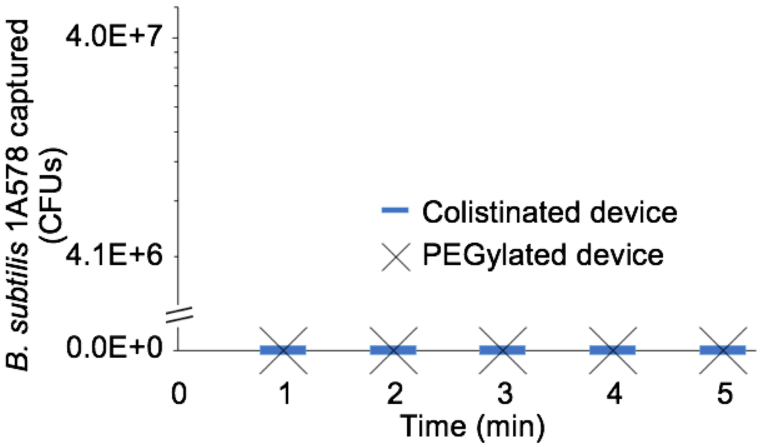

Figure B4. Evaluation of Gram-positive bacterial capture. Pathogen capture capacity of Gram-positive *B. subtilis* 1A578 when spiked into PBS and flowed through the colistinated and PEGylated double spiral microfluidic devices at 0.2 ml min^{-1}. The lack of capture indicates the specificity of colistin for Gram-negative pathogens. Results are plotted as the mean ± SD, *n* = 3.

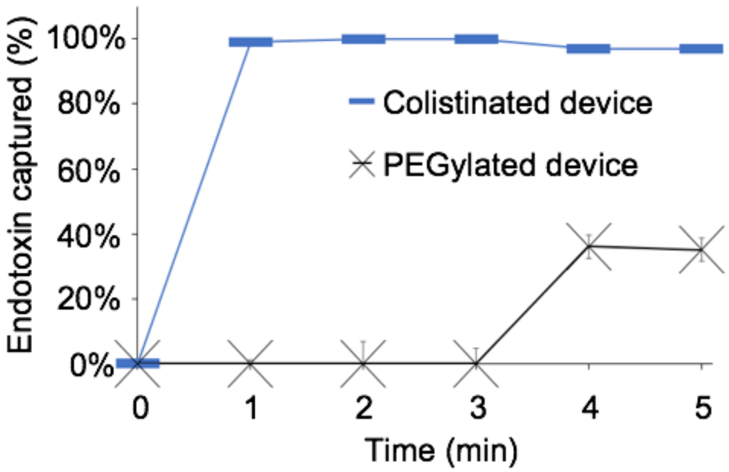

Figure B5. Quantification of endotoxin capture capacity. Endotoxin was spiked into endotoxin-free water (1 EU ml^{-1}) and flowed through the colistinated and PEGylated double spiral microfluidic devices at 0.2 ml min^{-1}. The amount of endotoxin captured over time was assessed. Results are plotted as the mean ± SD, *n* = 3.

REFERENCES

1. Cohen, J. *et al.* Sepsis: A roadmap for future research. *The Lancet Infectious Diseases* **15,** 581–614 (2015).
2. Mayr, F. B., Yende, S. & Angus, D. C. Epidemiology of severe sepsis. *Virulence* **5,** 4–11 (2014).
3. Singer, M. *et al.* The Third International Consensus Definitions for Sepsis and Septic Shock (Sepsis-3). *Jama* **315,** 801–10 (2016).
4. K., K. *et al.* Risk factors associated with Acinetobacter baumannii septicemia and its mortality rates in critically ill patients. *Crit. Care* **17,** S28 (2013).
5. Celik, I. H. *et al.* [Acinetobacter baumannii: an important pathogen with multidrug resistance in newborns]. *Mikrobiyol. Bul.* **45,** 716–22 (2011).
6. Nachimuthu, S. K. & Haug, P. J. Early detection of sepsis in the emergency department using Dynamic Bayesian Networks. *AMIA Annu. Symp. Proc.* **2012,** 653–62 (2012).
7. Stahl, J., Bergmann, H., Göttig, S., Ebersberger, I. & Averhoff, B. Acinetobacter baumannii Virulence Is Mediated by the Concerted Action of Three Phospholipases D. *PLoS One* **10,** e0138360 (2015).
8. Bergogne-Bérézin, E. & Towner, K. J. Acinetobacter spp. as nosocomial pathogens: Microbiological, clinical, and epidemiological features. *Clinical Microbiology Reviews* **9,** 148–165 (1996).
9. Manchanda, V., Sanchaita, S. & Singh, N. Multidrug resistant acinetobacter. *J. Glob. Infect. Dis.* **2,** 291–304 (2010).
10. CDC. Biggest Threats | Antibiotic/Antimicrobial Resistance | CDC. (2013). at <http://www.cdc.gov/drugresistance/biggest_threats.html>
11. Chopra, T. *et al.* Epidemiology of bloodstream infections caused by Acinetobacter baumannii and impact of drug resistance to both carbapenems and ampicillin-sulbactam on clinical outcomes. *Antimicrob. Agents Chemother.* **57,** 6270–5 (2013).
12. Jung, J. Y. *et al.* Risk factors for multi-drug resistant Acinetobacter baumannii bacteremia in patients with colonization in the intensive care unit. *BMC Infect. Dis.* **10,** 228 (2010).
13. Gerba, C. P., Rose, J. B. & Haas, C. N. Sensitive populations: Who is at the greatest risk? *Int. J. Food Microbiol.* **30,** 113–23 (1996).
14. Spapen, H., Jacobs, R., Van Gorp, V., Troubleyn, J. & Honoré, P. M. Renal and neurological side effects of colistin in critically ill patients. *Ann. Intensive Care* **1,** 14 (2011).
15. Song, J. Y. *et al.* In vitro activities of carbapenem/sulbactam combination, colistin, colistin/rifampicin combination and tigecycline against carbapenem-resistant Acinetobacter baumannii. *J. Antimicrob. Chemother.* **60,** 317–322 (2007).
16. Cheng, A. *et al.* Excess Mortality Associated With Colistin-Tigecycline Compared With Colistin-Carbapenem Combination Therapy for Extensively Drug-Resistant Acinetobacter baumannii Bacteremia. *Crit. Care Med.* **43,** 1194–1204 (2015).
17. Li, J. *et al.* Antibiograms of multidrug-resistant clinical Acinetobacter baumannii:

promising therapeutic options for treatment of infection with colistin-resistant strains. *Clin. Infect. Dis.* **45,** 594–598 (2007).

18. Zavascki, A. P., Carvalhaes, C. G., Picão, R. C. & Gales, A. C. Multidrug-resistant Pseudomonas aeruginosa and Acinetobacter baumannii: resistance mechanisms and implications for therapy. *Expert Rev. Anti. Infect. Ther.* **8,** 71–93 (2010).
19. Rolain, J.-M. *et al.* Real-time sequencing to decipher the molecular mechanism of resistance of a clinical pan-drug-resistant Acinetobacter baumannii isolate from Marseille, France. *Antimicrob. Agents Chemother.* **57,** 592–6 (2013).
20. Göttig, S. *et al.* Detection of pan drug-resistant Acinetobacter baumannii in Germany. *J. Antimicrob. Chemother.* **69,** 2578–9 (2014).
21. Cohen, J. The immunopathogenesis of sepsis. *Nature* **420,** 885–891 (2002).
22. Mihu, M. R. & Martinez, L. R. Novel therapies for treatment of multi-drug resistant Acinetobacter baumannii skin infections. *Virulence* **2,** 97–102 (2011).
23. Pivetal, J. *et al.* Selective isolation of bacterial cells within a microfluidic device using magnetic probe-based cell fishing. *Sensors Actuators B Chem.* **195,** 581–589 (2014).
24. Singh, S., Barick, K. C. & Bahadur, D. Surface engineered magnetic nanoparticles for removal of toxic metal ions and bacterial pathogens. *J. Hazard. Mater.* **192,** 1539–47 (2011).
25. Kang, J. H. *et al.* An extracorporeal blood-cleansing device for sepsis therapy. *Nat Med* **20,** 1211–1216 (2014).
26. Kang, J. H. *et al.* Optimization of Pathogen Capture in Flowing Fluids with Magnetic Nanoparticles. *Small* **11,** 5657–66 (2015).
27. Miller, S. E., Bell, C. S., McClain, M. S., Cover, T. L. & Giorgio, T. D. Dynamic Computational Model of Symptomatic Bacteremia to Inform Bacterial Separation Treatment Requirements. *PLoS One* **11,** e0163167 (2016).
28. Morris, C., Gray, L. & Giovannelli, M. Early report: The use of Cytosorb^{TM} haemabsorption column as an adjunct in managing severe sepsis: initial experiences, review and recommendations. *J. Intensive Care Soc.* **16,** 257–264 (2015).
29. Rachoin, J. S., Foster, D. & Dellinger, R. P. Endotoxin removal: how far from the evidence? From EUPHAS to EUPHRATES. *Contrib. Nephrol.* **167,** 111–8 (2010).
30. Raub, C. B., Lee, C. & Kartalov, E. Sequestration of bacteria from whole blood by optimized microfluidic cross-flow filtration for Rapid Antimicrobial Susceptibility Testing. *Sensors Actuators B Chem.* **210,** 120–123 (2015).
31. Di Carlo, D. Inertial microfluidics. *Lab Chip* **9,** 3038–3046 (2009).
32. Sun, J. *et al.* Double spiral microchannel for label-free tumor cell separation and enrichment. *Lab Chip* **12,** 3952 (2012).
33. Bhagat, A. A. S., Kuntaegowdanahalli, S. S., Dionysiou, D. D. & Papautsky, I. Spiral microfluidic nanoparticle separators. in *Microfluidics* **6886,** 68860M–68860M–11 (2008).
34. Goto, M. & Al-Hasan, M. N. Overall burden of bloodstream infection and nosocomial bloodstream infection in North America and Europe. *Clin. Microbiol. Infect.* **19,** 501–9 (2013).
35. Nielsen, S. L. *et al.* Decreasing incidence rates of bacteremia: A 9-year population-based

study. *J. Infect.* **69,** 51–59 (2014).

36. Nielsen, S. L. *et al.* Bacteremia is associated with excess long-term mortality: A 12-year population-based cohort study. *J. Infect.* **70,** 111–126 (2015).

37. García-Garmendia, J. L. *et al.* Risk factors for Acinetobacter baumannii nosocomial bacteremia in critically ill patients: a cohort study. *Clin. Infect. Dis.* **33,** 939–946 (2001).

38. Playford, E. G., Craig, J. C. & Iredell, J. R. Carbapenem-resistant Acinetobacter baumannii in intensive care unit patients: risk factors for acquisition, infection and their consequences. *J. Hosp. Infect.* **65,** 204–11 (2007).

39. Imperi, F. *et al.* The genomics of Acinetobacter baumannii: Insights into genome plasticity, antimicrobial resistance and pathogenicity. *IUBMB Life* **63,** 1068–1074 (2011).

40. Falagas, M. E., Bliziotis, I. A. & Siempos, I. I. Attributable mortality of Acinetobacter baumannii infections in critically ill patients: a systematic review of matched cohort and case-control studies. *Crit Care* **10,** R48 (2006).

41. Maragakis, L. L. & Perl, T. M. Acinetobacter baumannii: epidemiology, antimicrobial resistance, and treatment options. *Clin. Infect. Dis.* **46,** 1254–63 (2008).

42. Soon, R. L. *et al.* Different surface charge of colistin-susceptible and -resistant Acinetobacter baumannii cells measured with zeta potential as a function of growth phase and colistin treatment. *J. Antimicrob. Chemother.* **66,** 126–33 (2011).

43. Hancock, R. E. W. & Chapple, D. S. Peptide antibiotics. *Antimicrob. Agents Chemother.* **43,** 1317–1323 (1999).

44. Fournier, P. E. & Richet, H. The epidemiology and control of Acinetobacter baumannii in health care facilities. *Clin. Infect. Dis.* **42,** 692–699 (2006).

45. Vincent, J.-L. *et al.* International study of the prevalence and outcomes of infection in intensive care units. *JAMA* **302,** 2323–2329 (2009).

46. Doughari, H. J., Ndakidemi, P. A., Human, I. S. & Benade, S. The ecology, biology and pathogenesis of Acinetobacter spp.: an overview. *Microbes Environ.* **26,** 101–112 (2011).

47. WHO | Guidelines for drinking-water quality, fourth edition 2011. at <http://www.who.int/water_sanitation_health/publications/2011/dwq_chapters/en/>

48. Anaissie, E. J., Penzak, S. R. & Dignani, M. C. The Hospital Water Supply as a Source of Nosocomial Infections. *Arch. Intern. Med.* **162,** 1483 (2002).

49. Buttice, A. L., Stroot, J. M., Lim, D. V, Stroot, P. G. & Alcantar, N. A. Removal of sediment and bacteria from water using green chemistry. *Environ. Sci. Technol.* **44,** 3514–3519 (2010).

50. Maliyekkal, S. M., Lisha, K. P. & Pradeep, T. A novel cellulose-manganese oxide hybrid material by in situ soft chemical synthesis and its application for the removal of Pb(II) from water. *J. Hazard. Mater.* **181,** 986–95 (2010).

51. Zhao, Y. G., Shen, H. Y., Pan, S. D. & Hu, M. Q. Synthesis, characterization and properties of ethylenediamine-functionalized Fe3O4 magnetic polymers for removal of Cr(VI) in wastewater. *J. Hazard. Mater.* **182,** 295–302 (2010).

52. Lee, J.-J. *et al.* Synthetic ligand-coated magnetic nanoparticles for microfluidic bacterial separation from blood. *Nano Lett.* **14,** 1–5 (2014).

53. Decolin, D., Leroy, P., Nicolas, A. & Archimbault, P. Hyphenated liquid chromatographic

method for the determination of colistin residues in bovine tissues. *J. Chromatogr. Sci.* **35,** 557–564 (1997).

54. Phillips, T. M. *Encyclopedia of Chromatography, Volume 1*. (Taylor and Francis, 2005). doi:10.1081/E-SCHR-120039893

55. Uzun, O., Hu, Y., Verma, A., Chen, S., Centrone, A., Stellacci, F. Water-soluble amphiphilic gold nanoparticles with structured ligand shells. *Chem. Commun. (Camb).* 196–8 (2008). doi:10.1039/b713143g

56. Hamid, R., Rotshteyn, Y., Rabadi, L., Parikh, R. & Bullock, P. Comparison of alamar blue and MTT assays for high through-put screening. *Toxicol. Vitr.* **18,** 703–710 (2004).

57. Evans, B., Nelson, C., Yu, S. & Beavers, K., Kim, A., Li, H., Nelson, H., Giorgio, T. D, Duvall, C. L. Ex vivo red blood cell hemolysis assay for the evaluation of pH-responsive endosomolytic agents for cytosolic delivery of biomacromolecular drugs. *J. Vis. Exp.* e50166 (2013). doi:10.3791/50166

58. Moffatt, J., Harper, M., Harrison, P., Hale, J., Vinogradov, E., Seemann, T., Henry, R., Crane, B., St. Michael, F., Cox, A. Adler, B. *et al.* Colistin resistance in Acinetobacter baumannii is mediated by complete loss of lipopolysaccharide production. *Antimicrob. Agents Chemother.* **54,** 4971–4977 (2010).

59. Li, J. *et al.* Colistin: the re-emerging antibiotic for multidrug-resistant Gram-negative bacterial infections. *Lancet Infect. Dis.* **6,** 589–601 (2006).

60. Loo, C., Lowery, A., Halas, N., West, J. & Drezek, R. Immunotargeted nanoshells for integrated cancer imaging and therapy. *Nano Lett.* **5,** 709–711 (2005).

61. Sewell, S. L. & Giorgio, T. D. Synthesis and enzymatic cleavage of dual-ligand quantum dots. *Mater. Sci. Eng. C* **29,** 1428–1432 (2009).

62. Häkkinen, H. The gold–sulfur interface at the nanoscale. *Nat. Chem.* **4,** 443–455 (2012).

63. Brown, W., Iverson, B., Anslyn, E. & Foote, C. *Organic Chemistry*. (Cengage Learning, 2012).

64. Carrillo-Carrión, C., Simonet, B. M. & Valcárcel, M. Colistin-functionalised CdSe/ZnS quantum dots as fluorescent probe for the rapid detection of Escherichia coli. *Biosens. Bioelectron.* **26,** 4368–74 (2011).

65. Orwa, J., Govaeris, C., Busson, R., Roets, E., Schepdael, A., Hoogmartens, J. Isolation and Structural Characterization of Colistin Components. *J. Antibiot. (Tokyo).* **54,** 595–599 (2001).

66. Wuelfing, W. P., Gross, S. M., Miles, D. T. & Murray, R. W. Nanometer Gold Clusters Protected by Surface-Bound Monolayers of Thiolated Poly(ethylene glycol) Polymer Electrolyte. *J. Am. Chem. Soc.* **120,** 12696–12697 (1998).

67. Rampersad, S. N. Multiple applications of Alamar Blue as an indicator of metabolic function and cellular health in cell viability bioassays. *Sensors (Basel).* **12,** 12347–60 (2012).

68. Garonzik, S. M., Li, J., Thamlikitkul, V., Paterson, D. L., Shoham, S. & Jacob, J., Silveira, F. P., Forrest, A., Nation, R. L. Population pharmacokinetics of colistin methanesulfonate and formed colistin in critically ill patients from a multicenter study provide dosing suggestions for various categories of patients. *Antimicrob. Agents Chemother.* **55,** 3284–3294 (2011).

69. He, Q. & Zhang, Ji., Shi, J., Zhu, Z., Zhang, L., Bu, W., Guo, L., Chen, Y. The effect of PEGylation of mesoporous silica nanoparticles on nonspecific binding of serum proteins and cellular responses. *Biomaterials* **31,** 1085–1092 (2010).

70. Chan, S., Horner, S. R., Fauchet, P. M., A. & Miller, B. L. Identification of Gram Negative Bacteria Using Nanoscale Silicon Microcavities. *J. Am. Chem. Soc.* **123,** 11797–11798 (2001).

71. Rouf, M. A. Spectrochemical analysis of inorganic elements in bacteria. *J. Bacteriol.* **88,** 1545–1549 (1964).

72. Ward, S. K., Heintz, J. A., Albrecht, R. M. & Talaat, A. M. Single-cell elemental analysis of bacteria: quantitative analysis of polyphosphates in Mycobacterium tuberculosis. *Front. Cell. Infect. Microbiol.* **2,** 63 (2012).

73. Miller, S. E., Bell, C. S., McClain, M. S., Cover, T. L. & Giorgio, T. D. Colistin-Functionalized Nanoparticles for the Rapid Capture of Acinetobacter baumannii. *J. Biomed. Nanotechnol.* **12,** 1806–1819 (2016).

74. Wendt, C. & Grunwald, W. J. Polyclonal bacteremia due to gram-negative rods. *Clin. Infect. Dis.* **33,** 460–5 (2001).

75. Gaynes, R. & Edwards, J. R. Overview of nosocomial infections caused by gram-negative bacilli. *Clin. Infect. Dis.* **41,** 848–54 (2005).

76. Munford, R. S. Severe sepsis and septic shock: the role of gram-negative bacteremia. *Annu. Rev. Pathol.* **1,** 467–496 (2006).

77. Poole, K. Multidrug resistance in Gram-negative bacteria. *Curr. Opin. Microbiol.* **4,** 500–508 (2001).

78. Keynan, Y. & Rubinstein, E. The changing face of Klebsiella pneumoniae infections in the community. *Int. J. Antimicrob. Agents* **30,** 385–9 (2007).

79. Choi, J. Y. *et al.* Mortality risk factors of Acinetobacter baumannii bacteraemia. *Intern. Med. J.* **35,** 599–603 (2005).

80. Erbay, A., Idil, A., Gözel, M. G., Mumcuoğlu, I. & Balaban, N. Impact of early appropriate antimicrobial therapy on survival in Acinetobacter baumannii bloodstream infections. *Int. J. Antimicrob. Agents* **34,** 575–9 (2009).

81. Tumbarello, M. *et al.* Predictors of mortality in bloodstream infections caused by Klebsiella pneumoniae carbapenemase-producing K. pneumoniae: Importance of combination therapy. *Clin. Infect. Dis.* **55,** 943–950 (2012).

82. Borer, A. *et al.* Attributable mortality rate for carbapenem-resistant Klebsiella pneumoniae bacteremia. *Infect. Control Hosp. Epidemiol.* **30,** 972–6 (2009).

83. Cheewatrakoolpong, B., Steffen, E. K., Don Brown, R. & Berg, R. D. Kinetic analysis of bacterial clearance in mice using the ESTRIPc and KINET microcomputer programs. *J. Immunol. Methods* **58,** 375–381 (1983).

84. İşgüder, R., Ağın, H., Ceylan, G., Bayram, N. & Devrim, İ. Safety and efficacy of intravenous colistin use for the treatment of nosocomial multidrug-resistant Acinetobacter baumannii infections in a pediatric intensive care unit. *Am. J. Infect. Control* In press (2016). doi:http://dx.doi.org/10.1016/j.ajic.2015.12.028

85. Russo, T. A. *et al.* Rat pneumonia and soft-tissue infection models for the study of Acinetobacter baumannii biology. *Infect. Immun.* **76,** 3577–86 (2008).

86. Vincent, J.-L. *et al.* Sepsis in European intensive care units: results of the SOAP study. *Crit. Care Med.* **34,** 344–53 (2006).

87. Nadel, S. *et al.* Drotrecogin alfa (activated) in children with severe sepsis: a multicentre phase III randomised controlled trial. *Lancet (London, England)* **369,** 836–43 (2007).

88. Chung, H. M., Cartwright, M. M., Bortz, D. M., Jackson, T. L. & Younger, J. G. Dynamical system analysis of Staphylococcus epidermidis bloodstream infection. *Shock* **30,** 518–26 (2008).

89. de Biasi, J. & Rekik, L. Four compartment mammillary model applied to the pharmacokinetics of a spiroarsorane administered orally to rabbits. *J. Biomed. Eng.* **13,** 439–440 (1991).

90. Cypel, M. *et al.* Technique for prolonged normothermic ex vivo lung perfusion. *J. Heart Lung Transplant.* **27,** 1319–25 (2008).

91. Molina, D. K. & DiMaio, V. J. M. Normal Organ Weights in Men: Part II-The Brain, Lungs, Liver, Spleen, and Kidneys. *Am. J. Forensic Med. Pathol.* **33,** 368–72 (2012).

92. Altamura, M. *et al.* Splenectomy and sepsis: the role of the spleen in the immune-mediated bacterial clearance. *Immunopharmacol. Immunotoxicol.* **23,** 153–61 (2001).

93. Plowchalk, D. R. Development of a Physiologically Based Pharmacokinetic Model for Estradiol in Rats and Humans: A Biologically Motivated Quantitative Framework for Evaluating Responses to Estradiol and Other Endocrine-Active Compounds. *Toxicol. Sci.* **69,** 60–78 (2002).

94. Lewis, N. D. *et al.* Circulating monocytes are reduced by sphingosine-1-phosphate receptor modulators independently of S1P3. *J. Immunol.* **190,** 3533–40 (2013).

95. Guo, B. *et al.* Quantitative impact of neutrophils on bacterial clearance in a murine pneumonia model. *Antimicrob. Agents Chemother.* **55,** 4601–5 (2011).

96. Jacobs, A. C. *et al.* Inactivation of phospholipase D diminishes Acinetobacter baumannii pathogenesis. *Infect. Immun.* **78,** 1952–62 (2010).

97. Bruhn, K. W. *et al.* Host Fate is Rapidly Determined by Innate Effector-Microbial Interactions During Acinetobacter baumannii Bacteremia. *J. Infect. Dis.* **211,** 1296–305 (2015).

98. Gandhi, J. A. *et al.* Alcohol enhances Acinetobacter baumannii-associated pneumonia and systemic dissemination by impairing neutrophil antimicrobial activity in a murine model of infection. *PLoS One* **9,** e95707 (2014).

99. Bansal, S., Harjai, K. & Chhibber, S. Depolymerase improves gentamicin efficacy during Klebsiella pneumoniae induced murine infection. *BMC Infect. Dis.* **14,** 456 (2014).

100. Moore, T. a, Lau, H. Y., Cogen, A. L., Monteleon, C. L. & Standiford, T. J. Anti-tumor necrosis factor-alpha therapy during murine Klebsiella pneumoniae bacteremia: increased mortality in the absence of liver injury. *Shock* **20,** 309–15 (2003).

101. de Stoppelaar, S. F. *et al.* Thrombocytopenia impairs host defense in gram-negative pneumonia-derived sepsis in mice. *Blood* **124,** 3781–90 (2014).

102. Docobo-Pérez, F. *et al.* Efficacies of colistin and tigecycline in mice with experimental pneumonia due to NDM-1-producing strains of Klebsiella pneumoniae and Escherichia coli. *Int. J. Antimicrob. Agents* **39,** 251–254 (2012).

103. Pantopoulou, A. *et al.* Colistin offers prolonged survival in experimental infection by

multidrug-resistant Acinetobacter baumannii: the significance of co-administration of rifampicin. *Int. J. Antimicrob. Agents* **29,** 51–55 (2007).

104. Hoshino, K., Chen, P., Huang, Y. Y. & Zhang, X. Computational analysis of microfluidic immunomagnetic rare cell separation from a particulate blood flow. *Anal. Chem.* **84,** 4292–4299 (2012).

105. Sahly, H. *et al.* Capsule Impedes Adhesion to and Invasion of Epithelial Cells by Klebsiella pneumoniae. *Infect. Immun.* **68,** 6744–6749 (2000).

106. Chiang, S.-R. *et al.* Intratracheal colistin sulfate for BALB/c mice with early pneumonia caused by carbapenem-resistant Acinetobacter baumannii. *Crit. Care Med.* **2851,** 2851–2851 (2009).

107. Gross, K. *et al.* Bacterial clearance in the intact and regenerating liver. *J. Pediatr. Surg.* **20,** 320–323 (1985).

108. Lin, J.-C. *et al.* Do neutrophils play a role in establishing liver abscesses and distant metastases caused by Klebsiella pneumoniae? *PLoS One* **5,** e15005 (2010).

109. Lin, Y.-T. *et al.* TREM-1 promotes survival during Klebsiella pneumoniae liver abscess in mice. *Infect. Immun.* **82,** 1335–42 (2014).

110. van Faassen, H. *et al.* Neutrophils play an important role in host resistance to respiratory infection with Acinetobacter baumannii in mice. *Infect Immun* **75,** 5597–5608 (2007).

111. Al-Anazi, K. A. & Al-Jasser, A. M. Infections caused by Acinetobacter baumannii in recipients of hematopoietic stem cell transplantation. *Front. Oncol.* **4,** 1–10 (2014).

112. Cross, A. S., Opal, S. M., Sadoff, J. C. & Gemski, P. Choice of bacteria in animal models of sepsis. *Infect. Immun.* **61,** 2741–7 (1993).

113. Singh, R., Garg, N., Shukla, G., Capalash, N. & Sharma, P. Immunoprotective Efficacy of Acinetobacter baumannii Outer Membrane Protein, FilF, Predicted In silico as a Potential Vaccine Candidate. *Front. Microbiol.* **7,** 158 (2016).

114. Pan, C.-Y. *et al.* Piscidin is highly active against carbapenem-resistant Acinetobacter baumannii and NDM-1-producing Klebsiella pneumonia in a systemic Septicaemia infection mouse model. *Mar. Drugs* **13,** 2287–305 (2015).

115. Joly-Guillou, M. L., Wolff, M., Pocidalo, J. J., Walker, F. & Carbon, C. Use of a new mouse model of Acinetobacter baumannii pneumonia to evaluate the postantibiotic effect of imipenem. *Antimicrob. Agents Chemother.* **41,** 345–351 (1997).

116. Montero, A. *et al.* Efficacy of colistin versus beta-lactams, aminoglycosides, rifampin as monotherapy in a mouse model of pneumonia caused by multiresistant Acinetobacter baumannii. *Antimicrob. Agents Chemother.* **46,** 1946–1952 (2002).

117. Kumar, A. A. *et al.* Duration of hypotension before initiation of effective antimicrobial therapy is the critical determinant of survival in human septic shock. *Crit. Care Med.* **34,** 1589–1596 (2006).

118. Pezzulo, A. A. *et al.* Abundant DNase I-sensitive bacterial DNA in healthy porcine lungs and its implications for the lung microbiome. *Appl. Environ. Microbiol.* **79,** 5936–41 (2013).

119. Kreger, B. E., Craven, D. E., Carling, P. C. & McCabe, W. R. Gram-negative bacteremia. III. Reassessment of etiology, epidemiology and ecology in 612 patients. *Am. J. Med.* **68,** 332–43 (1980).

120. Lehmann, L. E. *et al.* A multiplex real-time PCR assay for rapid detection and differentiation of 25 bacterial and fungal pathogens from whole blood samples. *Med. Microbiol. Immunol.* **197,** 313–324 (2008).

121. Rello, J. *et al.* Severity of pneumococcal pneumonia associated with genomic bacterial load. *Chest* **136,** 832–40 (2009).

122. Levy, S. B. & Marshall, B. Antibacterial resistance worldwide: causes, challenges and responses. *Nat.Med.* **10,** S122–S129 (2004).

123. Opal, S. M., Dellinger, R. P., Vincent, J.-L., Masur, H. & Angus, D. C. The Next Generation of Sepsis Clinical Trial Designs: What Is Next After the Demise of Recombinant Human Activated Protein C? *Crit. Care Med.* **42,** 1–8 (2014).

124. Dellinger, R. P. *et al.* Surviving sepsis campaign: international guidelines for management of severe sepsis and septic shock: 2012. *Crit. Care Med.* **41,** 580–637 (2013).

125. Ferrer, R. *et al.* Empiric antibiotic treatment reduces mortality in severe sepsis and septic shock from the first hour: results from a guideline-based performance improvement program. *Crit. Care Med.* **42,** 1749–1755 (2014).

126. MacArthur, R. D. *et al.* Adequacy of early empiric antibiotic treatment and survival in severe sepsis: experience from the MONARCS trial. *Clin. Infect. Dis.* **38,** 284–8 (2004).

127. Hattori, N. *et al.* Cytokine-adsorbing hemofilter: old but new modality for septic acute kidney injury. *Ren. Replace. Ther.* **2,** 41 (2016).

128. Bernard, G. R. *et al.* Efficacy and safety of recombinant human activated protein C for severe sepsis. *N. Engl. J. Med.* **344,** 699–709 (2001).

129. Annane, D. & Cavaillon, J.-M. Corticosteroids in sepsis: from bench to bedside? *Shock* **20,** 197–207 (2003).

130. McCulloh, R. & Opal, S. M. Human Recombinant Lactoferrin for Sepsis. *Crit. Care Med.* **41,** 908–909 (2013).

131. Hutchins, N. A., Unsinger, J., Hotchkiss, R. S. & Ayala, A. The new normal: Immunomodulatory agents against sepsis immune suppression. *Trends in Molecular Medicine* **20,** 224–233 (2014).

132. Peng, Z.-Y. *et al.* Acute removal of common sepsis mediators does not explain the effects of extracorporeal blood purification in experimental sepsis. *Kidney Int.* **81,** 363–9 (2012).

133. Shoji, H. Extracorporeal endotoxin removal for the treatment of sepsis: Endotoxin adsorption cartridge (Toraymyxin). *Ther. Apher.* **7,** 108–114 (2003).

134. Kell, A. J. *et al.* Vancomycin-modified nanoparticles for efficient targeting and preconcentration of gram-positive and gram-negative bacteria. *ACS Nano* **2,** 1777–1788 (2008).

135. Dong, B. *et al.* Real-time Functional Analysis of Inertial Microfluidic Devices via Spectral Domain Optical Coherence Tomography. *Sci. Rep.* **6,** 33250 (2016).

136. Asmolov, E. S. The inertial lift on a spherical particle in a plane Poiseuille flow at large channel Reynolds number. *J. Fluid Mech.* **381,** 63–87 (1999).

137. Eichhorn, R. & Small, S. Experiments on the lift and drag of spheres suspended in a Poiseuille flow. *J. Fluid Mech.* **20,** 513 (2006).

138. Matas, J., Morris, J. & Guazzelli, E. Lateral Forces on a Sphere. *Oil Gas Sci. Technol.* **59,**

59–70 (2004).

139. Segré, G. & Silberberg, A. Behaviour of macroscopic rigid spheres in Poiseuille flow Part 2. Experimental results and interpretation. *J. Fluid Mech.* **14,** 136 (2006).

140. Segre, G. & Silberberg, A. Radial Particle Displacements in Poiseuille Flow of Suspensions. *Nature* **189,** 209–210 (1961).

141. Morsi, S. A. & Alexander, A. J. An investigation of particle trajectories in two-phase flow systems. *J. Fluid Mech.* **55,** 193 (1972).

142. Bhagat, A. A. S., Kuntaegowdanahalli, S. S. & Papautsky, I. Continuous particle separation in spiral microchannels using Dean flows and differential migration. *Lab Chip* **8,** 1906–14 (2008).

143. Johnston, I. D. *et al.* Dean flow focusing and separation of small microspheres within a narrow size range. *Microfluid. Nanofluidics* **17,** 509–518 (2014).

144. Zhou, J. & Papautsky, I. Fundamentals of inertial focusing in microchannels. *Lab Chip* **13,** 1121–32 (2013).

145. Auton, T. R., Hunt, J. C. R. & Prud'Homme, M. The force exerted on a body in inviscid unsteady non-uniform rotational flow. *J. Fluid Mech.* **197,** 241 (1988).

146. Marasco, C. C. *et al.* Real-Time Cellular Exometabolome Analysis with a Microfluidic-Mass Spectrometry Platform. *PLoS One* **10,** e0117685 (2015).

147. Zhou, J., Ellis, A. V. & Voelcker, N. H. Recent developments in PDMS surface modification for microfluidic devices. *Electrophoresis* **31,** 2–16 (2010).

148. Demming, S., Lesche, C., Schmolke, H., Klages, C.-P. P. & Büttgenbach, S. Characterization of long-term stability of hydrophilized PEG-grafted PDMS within different media for biotechnological and pharmaceutical applications. *Phys. Status Solidi Appl. Mater. Sci.* **208,** 1301–1307 (2011).

149. Qureshi, Z. A. *et al.* Colistin-resistant acinetobacter baumannii: Beyond carbapenem resistance. *Clin. Infect. Dis.* **60,** 1295–1303 (2015).

150. Zeigler, D. R. *Bacillus Genetic Stock Center Catalog of Strains: Bacillus subtilis 168.* (2000). at <http://x.bgsc.org/_catalogs/Catpart1.pdf>

151. Anderson, L. M., Henkin, T. M., Chambliss, G. H. & Bott, K. F. New chloramphenicol resistance locus in Bacillus subtilis. *J. Bacteriol.* **158,** 386–388 (1984).

152. Weinstein, M. P. *et al. Methods for Dilution Antimicrobial Susceptibility Tests for Bacteria That Grow Aerobically ; Approved Standard — Ninth Edition. Methods for Dilution Antimicrobial Susceptibility Tests for Bacteria That Grow Aerobically; Approved Standar-Ninth Edition* **32,** (2012).

153. *Performance Standards for Antimicrobial Susceptibility Testing; Twenty-Second Informational Supplement*. *Clinical and Laboratory Standards Institute (CLSI)* **32,** (2013).

154. Wiesel, P. *et al.* Endotoxin-induced mortality is related to increased oxidative stress and end-organ dysfunction, not refractory hypotension, in heme oxygenase-1–deficient mice. *Circulation* **102,** 3015–3022 (2000).

155. Kuntaegowdanahalli, S. & Bhagat, A. Inertial microfluidics for continuous particle separation in spiral microchannels. *Lab Chip* **9,** 2973–80 (2009).

156. Mei, R. *An approximate expression for the shear lift force on a spherical particle at finite*

reynolds number. *International Journal of Multiphase Flow* **18,** (1992).

157. Nivedita, N. & Papautsky, I. Continuous separation of blood cells in spiral microfluidic devices. *Biomicrofluidics* **7,** 54101 (2013).

158. Jeffery, G. B. The Motion of Ellipsoidal Particles Immersed in a Viscous Fluid. *Proc. R. Soc. A Math. Phys. Eng. Sci.* **102,** 161–179 (1922).

159. Hur, S. C., Choi, S. E., Kwon, S. & Carlo, D. Di. Inertial focusing of non-spherical microparticles. *Appl. Phys. Lett.* **99,** (2011).

160. Amini, H., Lee, W. & Di Carlo, D. Inertial microfluidic physics. *Lab Chip* **14,** 2739–2761 (2014).

161. Masaeli, M. *et al.* Continuous inertial focusing and separation of particles by shape. *Phys. Rev. X* **2,** (2012).